

國立交通大學

機械工程學系

博士論文

可互溶流體於 Hele-Shaw Cell 下界面不穩定現象
—注入及拉升流場

**Studies on Flow Instabilities on the Miscible
Fluid Interface in a Hele-Shaw Cell
—Injection and Lifting**

研究生： 王立杰

指導教授： 陳慶耀

中華民國一〇三年六月

可互溶流體於 Hele-Shaw Cell 下界面不穩定現象
—注入及拉升流場

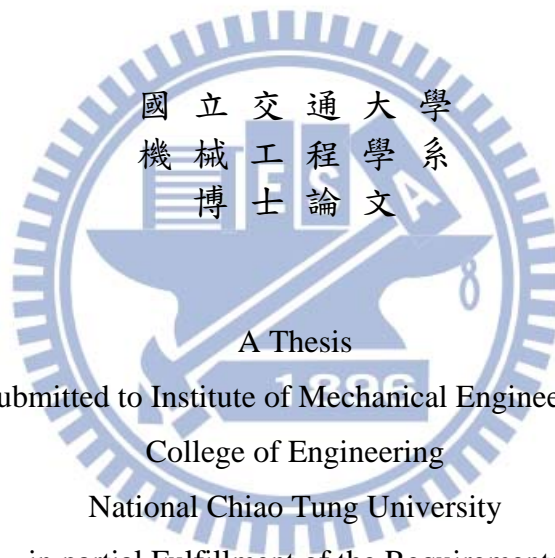
**Studies on Flow Instabilities on the Miscible Fluid Interface in a
Hele-Shaw Cell —Injection and Lifting**

研究生：王立杰

Student : Li-Chieh Wang

指導教授：陳慶耀

Advisor : Ching-Yao, Chen



Submitted to Institute of Mechanical Engineering

College of Engineering

National Chiao Tung University

in partial Fulfillment of the Requirements

for the Degree of

Doctor of Philosophy

in

Mechanical Engineering

June 2014

Hsinchu, Taiwan, Republic of China

中華民國一〇三年六月

中文摘要

黏滯度指狀物是指於平行薄板或多孔性材料間，以低黏滯度流體驅動高黏度流體時，兩流體間介面形成代表流場不穩定的指狀物型態，在多種工業製程中，多相流流場界面的不穩定性，嚴重影響產品品質及生產效率，常見案例為原油開採時以水性溶劑為驅動流體注入多孔性岩層推動更為黏稠原油時，卻因指狀物型態出現，而使水性溶劑穿透原油，降低開採效率。另平行薄板間高度改變形成的徑向拉升流場，也因可運用於黏著與潤滑分析，成為另一重要研究議題，本論文中運用高精確模擬(highly accurate simulation)之數值方法，分別以一致形(monotonic)與非一致形(nonmonotonic)黏滯度剖面之可互溶流體，探討徑向注入微小間隙的兩平行板間(即 Hele-Shaw Cell)與間隙隨時間增大之 Hele-Shaw Cell 徑向流場之界面演變，論文內容包含兩大部分：

第一部份於注入流場進行大量系統化的數值模擬，針對不同對流／擴散比(Peclet 值)與黏滯度剖面參數討論，首先除以過去學者慣用之指數型(下凹曲線)一致形黏滯度剖面進行研究外，另外定義線性及反指數型(上凸曲線)一致性黏滯度剖面與非一致形黏滯度剖面進行比較，結果顯示黏滯度對比固定時，各種黏滯度剖面對注入流場之穩定性無顯著影響，但如非一致性黏滯度剖面與上凸黏滯度剖面交錯，將激化流體介面間的不穩定性。另經由系統化改變非一致形黏滯度分布各參數值，觀察其對界面指狀化圖形之影響，除觀察到多種有趣之介面型態，諸如產生於一致形黏滯度分布所無法觀察到的成對雙渦旋流場及逆指狀物結構等現象，最後對非一致性黏滯度剖面各參數對整體注入流場穩定性影響進行討論。

第二部分首先探討不同拉升函數與初始擾動對流場穩定性之影響，相對於定量注入可互溶流體於徑向 Hele-Shaw Cell 流場會產生指狀物尾端開叉與分枝等多變流場現象，平行板間隙隨時間成指數化關係變化的拉升流場形成更錯綜複雜的流場現象，近期研究指出經由調整平板間隙與時間函數關係可控制流場指狀物的形態，本研究除得到指數拉升方式可較線性拉升方式獲得更不穩定之流場，亦歸納出高 Péclet 值與高黏滯度對比會增加指狀物長度，另對初始條件與擾動設定對流場穩定度影響於指數函數拉升時影響較大，線性函數拉升則幾乎沒有影響。進而討論不同黏滯度剖面之可互溶流體於指數拉升流場之界面型態，影響情況較注入流場顯著。接著採與第一部份相同作法，探討不同黏滯度剖面之可互溶流體於拉升流場之影響，發現黏滯度剖面對流場穩定性影響程度於拉升流場較注入流場大，且不穩定性均遵循下凹曲線>直線>上凸曲線順序，最後對非一致性黏滯度剖面各參數對拉升流場穩定性影響進行討論。

Abstract

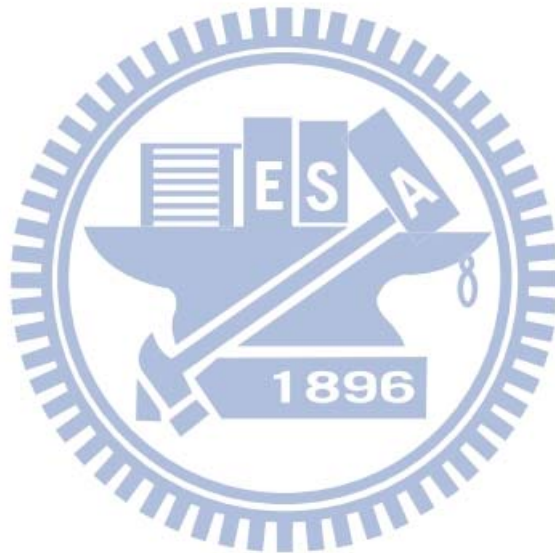
Viscous fingering is an interfacial fluid flow instability that occurs when less viscous fluid displaces another more viscous one in a Hele-Shaw cell or porous media, leading to the formation of finger-like pattern at the interface of both fluids. The interfacial evolution of multiphase flows will severely impact on the quality of production and efficiency in a variety of practical application of industrial process. Most frequent example of this instability is that of oil recovery for which viscous fingering takes place when an aqueous solution displaces more viscous oil in underground reservoirs, leading to the formation of nontrivial fingerlike structure and reduce the efficiency of the displacement process. Another particularly interesting variation of the classic radial flow is the investigation of fingering instabilities in Hele-Shaw cells presenting variable gap spacing. This is also a very important issue in many industrial areas including adhesion, lubrication, and colloidal hydrodynamics. In this dissertation, we carried out the highly accurate simulation to investigate the interfacial evolution in two scenarios – radial injection-driven miscible flow and lifting radial Hele-Shaw flow, both with the monotonic and nonmonotonic viscosity profile. So, the thesis consists of two parts:

Part 1 focus on radial injection-driven miscible flow in a Hele-Shaw cell and covers three major topics. To begin with, we perform numerical experiments in a wide range to study the dispersion relation on both the Péclet number and the parameters of the viscosity profile. A monotonic viscosity-concentration relation of exponential type (concave) by other scholars is assumed, and a linear and reverse (convex) monotonic viscosity profiles and nonmonotonic one are also discussed. Results of this study show that as the overall viscosity contrast held constant, nonmonotonic

viscosity profile lead to a more stable flow than that of monotonic one, and there are no significant differences in different viscosity profiles. However, if the nonmonotonic viscosity profile crosses the convex monotonic viscosity profile, the nonmonotonic feature enhances the prominence of interfacial instability. Then, a great variety of morphological behaviors is systematically introduced. In general, the nonmonotonic feature enhances the prominence of interfacial instability. Formation of dual vortex pairs and “reverse fingering”, where the fingers spread farther in the backward than in the forward direction are observed, which are not present in monotonic viscosity profile. Finally, we have carried out a parameter study to understand the effects of nonmonotonicity on the stability of the injection flow.

In part 2, discussions start with the investigation of the influence of lifting scenario and the perturbation set. Contrast to the injection-driven miscible flow in radial Hele-Shaw cells which leads to the formation of morphing flow phenomenon of finger tip-splitting and side-branch events are plentiful if the injection rate is constant with time. More complicated flow are present for time-dependent gap flow which results in different kinds of patterns, and leads to intricate morphologies if the cell’s gap width grows exponentially with time. Recent studies show that the growing of intricate patterns due to lifting can be controlled by properly adjusting the time-dependent gap width. Moreover, we found the exponential lifting case will cause the flow more unstable than the variant lifting situation. We also deduce higher Péclet number and viscous contrast (A in monotonic viscosity profile and μ_m in nonmonotonic one) demonstrate more vigorous fingering. The sensitivity of the system to changes in the initial conditions and perturbation set is also discussed. Next, the effects of four viscosity profiles as stated in part 1 have been investigated. Unlike injection flow, the stability of three monotonic viscosity profiles are always in the series of

concave, linear and convex. However, as injection flow, if the nonmonotonic viscosity profile crosses the convex curve will enhances the prominence of interfacial instability. Finally, we have carried out a parameter study to understand the effects of nonmonotonicity viscosity profile on the stability of the lifting flow.



誌 謝

由衷地感謝陳慶耀教授，在原指導教授楊文美老師退休之後，願意接受一個對數值計算及流場不穩定性完全不了解的學生，讓昔為航空背景的我能夠進入此領域進行研究，且常因任務需求，無法常與您 meeting 的情況下，只能剝奪您休息時間，在新竹至台中的路途上盡量挖掘您學術及人生的寶庫，獲得您無私的分享，在此研究上能夠有些許的發現，全因為您細心指導。日後研究的範圍還很寬廣，我會將您的指導盡情揮灑出屬於我的天空。

感謝大學時期曾教過我的曾培元教授及宋齊有教授，以及許立傑教授、吳宗信教授及陳彥升研究員能在百忙之中遠道而來，蒞臨指導我的學位口試，不吝給予寶貴意見，使我了解論文撰擬上的疏漏，學習到更多陳述解決問題及表達結果的技巧，謝謝各位老師的指導；也感謝曾經與我一同在實驗室共同打拼的學弟妹琦雯、裕盛及彥宏等，沒有你們的陪伴與協助還真不知如何完成這段路。

就學期間涵蓋職場兩個階段，感謝空軍測評戰研中心國正、中樑、洪安及文琳主任讓我實現飛行的夢想以及求學的支持，及兄弟們的情義相挺，亦要感謝國家中山科學研究院航空研究所准予以公餘進修方式攻讀博士學位。

一路走來兼顧工作與求學兩方面的負荷，父母及愛妻秀梅對家庭的照顧，使我可以無後顧之憂地全力以赴，彭老醫師精湛的醫術也使我精神及體能始終可以維持最佳狀況，芄允和心佑兩位天真活潑又可愛的女兒也總是讓我疲憊時重新燃起動力，讓我完成我的夢想。

僅將本文獻給每一位曾在人生路上伴我成長的家人、師長、兄弟及朋友們，感謝你們。

Contents

中文摘要	i
Abstract	iii
誌謝	vi
Contents.....	vii
List of Figures	ix
Nomenclature	xvii
Chapter 1 Introduction	1
1.1 Literatures Review	1
1.2 Objective and Organization of This Thesis.....	6
Chapter 2 General Feature	9
2.1 Physical Problem.....	9
2.2 Governing Equations.....	11
2.2.1 Viscosity Profile.....	11
2.2.2 Injection-Driven Radial Hele-Shaw flow	13
2.2.3 Time-dependent Gap Hele-Shaw Cell	17
2.3 Numerical Scheme	21
2.4 Validation.....	23
Chapter 3 Fingering Instability of Miscible Injection Hele-Shaw Flows.....	27
3.1 Monotonic Viscosity Profile	27
3.2 Nonmonotonic Viscosity Profile.....	28
3.2.1 Influence of the Péclet number Pe	29
3.2.2 Influence of the maximum viscosity μ_m	30
3.2.3 Influence of the location of the maximum viscosity c_m	33
3.2.4 Influence of the end-point viscosity contrast α	35
Chapter 4 Controlling Radial Fingering Patterns in Miscible Lifting	

Hele-Shaw Flow.....	57
4.1 Influence of the Lifting Scenarios.....	57
4.2 Influence of the Perturbation Set	60
4.3 Monotonic Viscosity Profile	61
4.4 Nonmonotonic viscosity profile.....	63
4.4.1 Influence of the maximum viscosity μ_m	63
4.4.2 Influence of the end-point viscosities contrast α	64
4.4.3 Influence of the location of the maximum viscosity c_m	65
Chapter 5 Conclusions and Recommendations of Future Work.....	90
5.1 Conclusions	90
5.1.1 Fingering Instability of Miscible Injection Hele-Shaw Flows	90
5.1.2 Controlling Radial Fingering Patterns in Miscible Lifting	
Hele-Shaw Flow.....	91
5.2 Recommendations of Future Work	92
Appendix 1 Vorticity.....	93
Appendix 2 Hele-Shaw cell	97
References	99
Resume	106

List of Figures

Figure 1: Schematic illustration of a perturbation of the interface between two fluids in Hele-Shaw cell, the injecting flow ₁ pushes the displaced flow ₂	25
Figure 2: A physical interpretation of the stability criteria.	25
Figure 3: Schematic setup for an injection-driven miscible radial flow in Hele-Shaw cell with cell gap h . The fluid 1 is injected at the center with a flux Q . Viscosities of the injected fluid 1 and the displaced fluid 2 are denoted as μ_1 and μ_2 , respectively.....	26
Figure 4: Schematic setup of the time-dependent gap radial Hele-Shaw flow with miscible fluids. The upper plate of the cell is lifted, so that the gap of the cell is variable. The inner fluid is more viscous ($\mu_2 > \mu_1$).....	26
Figure 5: Various types of monotonic viscosity profiles with $A=0.5$ (viscosity ration $\alpha=3$). The quasi-monotonic profile is represented by insignificant non-monotonicity of $\mu_m=3.001$ and $c_m=0.03$	37
Figure 6: Concentration images with $Pe=800$ at $t=0.30$ for various types of viscosity profiles shown in Fig. 5, (a) concave; (b) linear; (c) convex and (d) quasi-monotonic. In the present unstable conditions, i.e. $\mu_1 > \mu_2$, fingering instabilities are observed for all the profiles. The overall patterns show great similarities, which indicate insignificant influences of the local correlations between fluid concentration and the viscosity.....	38
Figure 7: Evolutions of the interfacial lengths, which can be used as a global quantitative measurement of the prominence of fingering, for the four conditions shown in Time evolution of the interfacial	

length under the condition set as Fig. 5. The global characteristics of interfacial lengths show no significant variations. Nevertheless, a general trend is observed, in which a more convex profile leads to a more unstable interface at the early time, and turns more stable at a later stage..... 39

Figure 8: Representative profiles of non-monotonic viscosity. The black lines show unfavorable end-point viscosity contrasts of $\alpha=3$, $c_m=0.1$ for $\mu_m=9$ and 14. Favorable end-point viscosity contrasts are represented by the red lines with $\alpha=0.2$, $c_m=0.2$ for $\mu_m=6$ and 9. 40

Figure 9: Concentration images for the case of unfavorable viscosity profile ($\alpha=2$, top row), and favorable viscosity profile ($\alpha=0.5$, bottom row). These simulation used for different Péclet number with parameters set for $\mu_m=4$ and $c_m=0.2$ at $t=0.35$ 41

Figure 10: The contour of concentration for $c=0.5$ versus azimuth with the same viscosity profile sets of Fig. 9. Both on unfavorable case ($\alpha=2$, top fig) and favorable end point contrast ($\alpha=0.5$, bottom fig) with $Pe=800$, at $t=0.1, 0.2$ and 0.35 , respectively. The red line indicate the position of basestate as a function of the time. 42

Figure 11: Interfacial length L_n as a function of time for different Péclet number with constant viscosity profile ($\mu_m=4$ and $c_m=0.2$) in unfavorable and favorable viscosity profile. In the inset the number label the Péclet number and end-point viscosity contrast. An interesting phenomena damping effect can be observed in $Pe=800$ and $\alpha=0.5$ set and will be discussed later..... 43

Figure 12: Concentration images for the non-monotonic viscosity profiles shown in Fig. 8 with $Pe=400$. Unfavorable viscosity contrast of

$\alpha=3$ and $c_m=0.1$ for $\mu_m=9$ (a) and $\mu_m=14$ (b). Favorable viscosity contrast of $\alpha=0.2$ and $c_m=0.2$ for $\mu_m=6$ (c) and 9 (d). The non-monotonic viscosity profile enhances fingering instability significantly. Even an original stable interface in a monotonic profile appears significantly fingering if the viscosity profile is non-monotonic, i.e. $\alpha < 1$ shown in (c) and (d). In addition, the prominences of fingering are enhanced by degree of the monotony, i.e. higher μ_m 44

Figure 13: Correspondent images of vorticity for the cases shown in Fig. 8. Besides the well-understood vorticity pairs inside the individual fingers, additional pairs of detached vorticity caps right beyond the fingertips are generated due to the non-monotony of viscosity profile. 45

Figure 14: Evolutions of the normalized interfacial lengths for the four cases shown in Fig. 8. After a short period of time with significant growths, the interfacial lengths appear to level off. In line with the common expectations, a more unfavorable end-point viscosity contrast, such as $\alpha=3$, results in a more prominent fingering instability. Also confirmed is that significance of the viscosity non-monotony leads to a more unstable interface, e.g. $\mu_m=9$ 46

Figure 15: A time series of the contours on the concentration to the Fig. 13 (d) parameters sets as $\mu_m=9$. Time is varied between 0.03 and 0.13 with increments of 0.02 in blue lines. Times during damping effect are plot in red lines. 47

Figure 16: The contour of concentration for to the Fig. 13 (d) parameters sets as $\mu_m=9$ at $t=(a)0.0343$, (b) 0.0729, and (c)0.11. The green lines indicate the position of basestate as a function of the time.

.....	48
Figure 17: Representative profiles of non-monotonic viscosity for the cases with unfavorable and favorable end-point contrasts of $\alpha=3$ and 0.7, respectively. The local maximum viscosity contrast is $\mu_m=4$, whose position is at $c_m=0.1, 0.3,$ and $0.5.$	49
Figure 18: Parameter for the end-point derivatives of the viscosity profile, A as a function of the maximum of the viscosity profile, c_m , both for the unfavorable and favorable end-point viscosity contrast in Fig. 17.....	50
Figure 19: Evolutions of the normalized interfacial lengths for $Pe=400$ with the six viscosity profiles shown in Fig. 17. The most unstable interface at a later time stage is always triggered by a smallest $c_m=0.1$, whose viscosity profile appears more concave, for both unfavorable and favorable end-point conditions. The trend agrees well with the findings presented in Fig. 18.....	51
Figure 20: Concentration images for the non-monotonic viscosity profiles shown in Fig. 17 with $Pe=400$ and $\mu_m=4$ at $t=0.30$. Unfavorable viscosity contrast of $\alpha=3$ and $c_m=0.1, 0.3,$ and $0.5.$ Favorable viscosity contrast of $\alpha=0.2$ and $c_m=0.1, 0.3,$ and $0.5.$ The lower c_m enhances fingering instability significantly. Even an original unstable interface in higher c_m appears significantly more unstable either favorable or unfavorable shown in Fig. 19.....	52
Figure 21: Concentration images (top row) and vorticity images (bottom row) for viscosity profile set with $\mu_m=13$ and $c_m=0.1$ for (a) $Pe=400$ and $\alpha=2.$ (b) $Pe=200$ and $\alpha=9.$ (c) $Pe=400$ and $\alpha=9$ at $t=0.30.$ The outer fluid is more viscous ($\mu_2 > \mu_1$).....	53
Figure 22: Evolutions of the normalized interfacial lengths for Fig. 21. ...	54
Figure 23: Zoom in the nonmonotonic viscosity profiles for $\mu_m=4, c_m=0.1,$	

and $\alpha=0.2, 0.5, \text{ and } 1$	55
Figure 24: Concentration images (top row) and vorticity images (bottom row) for $Pe=400, \mu_m=4, c_m=0.1, \alpha=0.2, 0.5, \text{ and } 1$ at $t=0.30$. The inner fluid is more viscous ($\mu_1 > \mu_2$) and the green lines in vorticity images indicate the position of μ_m .	55
Figure 25: Time evolution of the interfacial length with $\mu_m=4, c_m=0.1, \alpha=0.2, 0.5, \text{ and } 1$ for $Pe=400$. In the inset the detail viscosity profiles for the three parameters sets. No significant main effect for favorable end-point contrast was found.....	56
Figure 26: Concentration images for the dimensionless gap distances $h/h_0=2, 3, \text{ and } 4$, for the cases of exponential lifting (top row), and variant lifting (bottom row) to the parameter set as $Pe=3000, A=0.925$. The domain of x and y axis are -0.8 to 0.8	67
Figure 27: Concentration images for $Pe=2000$ (first column), 3000 (second column), 4000 (third column), and $A=0.762$ (top row), 0.905 (mid row), 0.925 (bottom row) at dimensionless gap distances $h/h_0=4$, for the cases of exponential lifting. The domain of x and y axis are -0.5 to 0.5 .	68
Figure 28: Interfacial lengths L_s as a function of the dimensionless gap distance h/h_0 for the exponential lifting case. These simulations used the same physical parameters as in Fig. 27. In the inset the numbers label the distinct Pe and A sets.	69
Figure 29: A dimensionless gap distances h/h_0 series of the contours on the concentration to the parameters sets as $Pe=3000, A=0.925$ for the exponential lifting case. For the dimensionless gap distance $h/h_0=$ (a) 1.5 , (b) 2 , (c) 2.5 , and (d) 4 .	70
Figure 30: A dimensionless gap distances h/h_0 series of the contours on the concentration to the parameters sets as $Pe=3000, A=0.925$ for	

the variant lifting situation. For the dimensionless gap distance $h/h_0 =$ (a) 1.5, (b) 2, (c) 2.5, and (d) 4.	70
Figure 31: Concentration images for the dimensionless gap distance $h/h_0=4$ for the cases of exponential lifting (top row), and variant lifting (bottom row). These simulations used the same physical parameters as in Fig. 26, but utilized two distinct set of initial random conditions: perturbation set 2 (first column), and perturbation set 3 (second column).	71
Figure 32: Interfacial length L_s as a function of the dimensionless gap distance h/h_0 for the exponential lifting (<i>EL</i>) case, and three different sets of initial perturbations (solid curves). The dashed curves represent similar sets of data for the variant lifting (<i>VL</i>) situation. In the inset the numbers label the distinct perturbation sets.	72
Figure 33: Concentration images for the dimensionless gap distance $h/h_0=2, 3, \text{ and } 4$ for the cases of exponential lifting. These simulations used the same physical parameters as in Fig. 29, but utilized two distinct set of initial random conditions: amplitude=0.05 (top row), and amplitude=0.1 (bottom row).	73
Figure 34: Interfacial lengths L_s as a function of the dimensionless gap distance h/h_0 for the exponential lifting case. These simulations used the same physical parameters as in Fig. 27. In the inset the numbers label the amplitude sets.	74
Figure 35: Four kinds of viscosity profiles with $A=0.925$ ($\alpha=25.67$). The parameters set of the Quasi-monotonic viscosity profile is $c_m=0.1$ and $\mu_m=25.77$	75
Figure 36: Concentration images for the dimensionless gap distance $h/h_0=2, 3, \text{ and } 4$, for the cases in Fig. 35 with $Pe=2000$ and $A=0.925$ for	

(a) Concave (b) Linear (c) Convex (d) Quasi-monotonic. The inner fluid is more viscous ($\mu_2 > \mu_1$).....	76
Figure 37: Interfacial length L_s as a function of the dimensionless gap distance h/h_0 for the exponential lifting case and four kinds of different viscosity profiles for Fig. 35 with $Pe=2000$. In the inset the numbers label the distinct viscosity profiles.	77
Figure 38: Five kinds of viscosity profiles with $A=0.848$ ($\mu_m=e^A=12.18$). The parameters set of the nonmonotonic viscosity profile is $c_m=0.1$ and $\alpha=10$	78
Figure 39: Interfacial length L_s as a function of the dimensionless gap distance h/h_0 for the exponential lifting case and five viscosity profiles in Fig. 38 with $Pe=4000$. In the inset the numbers label the distinct viscosity profiles.....	79
Figure 40: Concentration images for the dimensionless gap distance $h/h_0=4$ with $Pe=4000$, for the viscosity profile depicted in Fig. 38 for (a) Concave (b) Linear (c) Convex (d) Nonmonotonic, $\alpha=10$. The inner fluid is more viscous ($\mu_2 > \mu_1$).....	80
Figure 41: Concentration images of parameters set $\alpha=3$ and $c_m=0.1$ with $Pe=3000$ for the exponential lifting case (a) $\mu_m=8$, (b) $\mu_m=16$, (c) $\mu_m=24$ and (d) $\mu_m=32$ for the dimensionless gap distance $h/h_0=4$,	81
Figure 42: Interfacial length L_s as a function of the dimensionless gap distance h/h_0 for the four cases shown in Fig. 41. In the inset the numbers label the distinct maximum viscosity μ_m	82
Figure 43: Time evolution of the interfacial length L_s for two monotonic viscosity profiles with $\alpha=20.08$ and 16.44 and four nonmonotonic viscosity profiles with $\mu_m=16.44$, $c_m=0.1$, $\alpha=3$, 9 , 12 , and 15 for $Pe=3000$. In the inset the detail viscosity profiles	

for the seven parameters sets.....	83
Figure 44: Concentration images of parameters set $\mu_m=16.44$ and $c_m=0.1$ with $Pe=3000$ for the exponential lifting case (a) $\alpha=3$, (b) $\alpha=9$, (c) $\alpha=12$ and (d) $\alpha=15$ for the dimensionless gap distance $h/h_0=4$. Despite the finger lengths of different cases are very close; the morphology in each set is quite similar.....	84
Figure 45: Correspondent images of vorticity for the cases shown in Figure 43 for the dimensionless gap distance $h/h_0=4$, (a) $\alpha=3$; (b) $\alpha=9$; (c) $\alpha=12$ and (d) $\alpha=15$ for $Pe=3000$. Unlike the inner fingers in injection flow, it may become disappear, as the difference between α and μ_m decrease.....	85
Figure 46: Representative profiles of non-monotonic viscosity profiles show end-point viscosity contrasts with $\alpha=3$, $\mu_m=24$ for $c_m=0.1$, 0.3, 0.5 and 0.7.....	86
Figure 47: Concentration images for the dimensionless gap distance $h/h_0=4$ with the non-monotonic viscosity profiles shown in Fig. 46 with $Pe=2000$ for series of (a) $c_m=0.1$, (b) $c_m=0.3$, (c) $c_m=0.5$ and (d) $c_m=0.7$	87
Figure 48: Time evolution of the interfacial length with viscosity profile $\alpha=3$, $\mu_m=24$ with $Pe=2000$ for $c_m=0.1$, 0.3, 0.5 and 0.7.....	88
Figure 49: Concentration images for the dimensionless gap distance $h/h_0=4$ for the favorable end-point contrast cases of $\alpha=0.25$ (top row), and the unfavorable end-point contrast cases of $\alpha=4$. Utilized two distinct set of the location of the maximum viscosity: $c_m=0.1$ (first column), and $c_m=0.9$ (second column). Other parameters set are $Pe=3000$ and $\mu_m=8$	89

Nomenclature

Roman Symbols

a	lifting ratio
A	Atwood number
b	parameter of compact finite-difference
c	concentration of the injecting fluid
h	gap thickness
k	permeability
L	interfacial length
M	mobility
N	the number of grid point
Pe	Péclet number
p	pressure
Q	injection rate
R	mobility ratio
r	radius
t	time
u	velocity vector
V	volume of the fluid
v	velocity vector
x, y	spatial direction

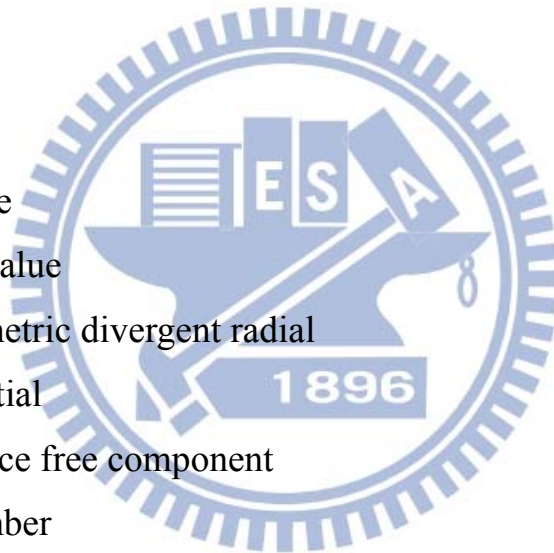
Greek Symbols

α	viscosity contrast
β	parameter of Runge-Kutta

γ	control parameter
δ	a control parameter with an inverse dimension of time.
η	parameter of Runge-Kutta
μ	viscosity
ν	parameter of Runge-Kutta
ξ	parameter of compact finite-difference
ϕ	stream function
A	stability criteria
ρ	density
σ	core size

Subscripts

B	base state
c	critical value
d	axisymmetric divergent radial
exp	exponential
f	divergence free component
g	grid number
i	initial
$linear$	linear viscosity profile
m	maximum
$mono$	monotonic viscosity profile
n	normalized
non	nonmonotonic viscosity profile
pot	potential part
r	rotational part
v	variant dimensional lifting situation
vex	convex viscosity profile



- 0* initial condition
- 1* injection in injection flow / outer flow in lifting flow
- 2* displaced in injection flow / inner flow in lifting flow



Chapter 1 Introduction

1.1 Literatures Review

Viscous fingering (VF) is a hydrodynamic instability occurring where a higher viscous fluid is displaced by a less viscous one in porous media. It can be observed the different viscous fingering instabilities in the interface between the two fluids, and can be explained by Saffman-Taylor instability. In most applications, viscous fingering instabilities are undesirable as the displacing fluid fingers through and by pass the displaced one, reduces the efficiency of this injection. Over the years viscous fingering problem has been extensively studied both experimentally and theoretically. The related studied can be classified into two categories depending on whether the viscosity profiles are monotonic or nonmonotonic. For convenience, Tan and Homsy [1] defined a particular case in which viscosity varies exponentially with the concentration of injection fluid, as well as monotonic viscosity profiles. They also used Fourier spectral method and found as time progresses, the nonlinear behavior of fingers cause a few dominant fingers spread and shield [2]. However, some driving fluid used to petroleum secondary recovery techniques such as a mixture of alcohols and water need not to be monotonic. Manickam and Homsy [3] defined a nonmonotonic viscosity profile for the viscosity concentration data of alcohols to approximate nature fluid behavior. They have carried out a parameter study to understand the effects of nonmonotonicity on the stability of the flow. Other last strategies aim to analysis viscous fingering by non-Newtonian fluid interfaces [4].

Researchers studies have focused on simpler geometries, such as two fluids in the narrow gap between closely-spaced parallel plates of a Hele-Shaw cell, include rectilinear and radial flow, as well as quarter

five-spot configuration. Many theoretical and experimental studies have been performed in both geometrics. Tan and Homsy [1] used the quasi-steady-state approximation (QSSA) for a radial source flow in porous media with monotonic viscosity profiles. They found that the unfavorable viscosity gradient results the fluid more unstable in radial source flow. They also did a critical Péclet number Pe_c calculation, above which displacement becomes unstable, and vice versa. Chen and Meiburg [5, 6] focused on miscible quarter five-spot configuration and radial flows in homogeneous and heterogeneous environment with monotonic viscosity profiles, and described in detail as a function of the mobility ratio R and the Péclet number Pe . Chen *et al.* [6-9] also investigate the stability of time-dependent gap Hele-Shaw cell which is significant to adhesion related problem. In addition, the results by Manickam and Homsy [10] used Hartley transform based spectral method for rectilinear flow with nonmonotonic viscosity profiles show a new phenomenon of “reverse” fingering and understand the effects of nonmonotonicity on the stabilization of the flow. Ruith and Meiburg [11] added the effect of gravity force in miscible displacement and investigate the influence of the Péclet number, the viscosity and density contrasts, and the aspect ratio on the dynamic evolution of the displacement. An up-to-date report write by Jha *et al.* [12] take viscosity contrast into account to affects fluid mixing. Recent extend the studies of the miscible flow in a rotating cell [13-17] demonstrate fingering morphologies unlike in injection and lifting flow [18].

The main difference between the radial and the rectilinear displacement is that for the rectilinear flow, the base state velocity is a constant, while for the radial displacement, the velocity decreases spatially $1/r$. Nonlinear simulations of quarter five-spot configuration displacements have been confirmed the linear stability results, which for small times correspond to

radial source flows. Pankiewicz and Meiburg [19] extend this analysis to numerical simulation of quarter five-spot configuration with nonmonotonic viscosity profiles, which have done a deliberative parameter study, and derive that either favorable or unfavorable end point contrast will cause the flow unstable only that the Péclet number is sufficiently high. They also find there exist two concentric rings of vortex region and touch each other exactly at the location of the viscosity maximum. Shariati and Yortsos [20] explained the overall effect any two adjacent counter-rotating vortices may further stabilize or destabilize the flow. As point out earlier, some late researchers study the viscous fingering by chemical means. Chemical reaction may change the density, surface tension or viscosity of the fluid. Hejanctuzi *et al.* [21] used linear stability analysis for a reaction-diffusion-convection problem and found the effects of chemical reaction on the stability of the flow are like nonmonotonicity.

To date, most of the previous studies (e.g. Tan and Homsy [2]; Chen and Meiburg [5]) on monotonic viscosity profile consider flow on the relation to concentration and viscosity are an exponential function. There is a noticeable absence of research projects dealing with different types of monotonic viscosity profiles. Due to the practical and academic relevance of the injecting problem, it is of interest to study and understand the emerging interfacial under many different viscosity profiles. Additionally, the effect of nonmonotonic viscosity profile on the stabilization of miscible displacement has been considered in a limited number of studies. Chouke [22] and Tan and Homsy [23] obtained stability criteria Λ can be interpreted through the slopes in injection and displaced fluid sides. They employed QSSA to analyze the stability characteristics. Loggia *et al.* [24] make an exhaustive study of the parameter and explain the key for of longitudinal dispersion in making conditionally unstable an initially stable profile as sufficient time. Nevertheless, Manickam and Homsy [3] used the

QSSA and suggested the equation fails to hold at large times when the base state has diffused out. Later Kim and Choi [25] tackled the problem of without QSSA and believed the system is unconditionally stable for long-wave disturbance regardless of viscosity profile.

Miscible displacements with nonmonotonic viscosity profiles are characterized by negligible surface tension, so that the interplay of by the Péclet number and the parameters of the viscosity profile dictate the pattern formation behavior. Although researchers agreed the viscosity profiles effects the stability of fluid. Not only little research has been done on the final state of the nonmonotonic viscosity profile variation system, but has never seen discussing different monotonic viscosity profile stability of the flow field. We are therefore interested in developing a fundamental understanding of miscible radial flow with monotonic and nonmonotonic viscosity profile.

Much of the research of the traditional Saffman-Taylor problem has examined the flow in flat, motionless, constant-gap spacing Hele-Shaw cells, in which the fluids are relatively simple. Somewhat simpler radial and rectangular geometry situation have been examined, where the upper plate is lifted uniformly, i.e., the plates remain parallel to each other during the lifting process. It is the so-called *lifting radial Hele-Shaw flow* and result Saffman-Taylor situation in the formation of complex structures.

A particularly interesting variation of the classic radial flow is the investigation of fingering instabilities in Hele-Shaw cells presenting variable gap spacing. The study of compliant adhesive layers is highly interdisciplinary involves a great variety of areas range from interfacial science and rheology to pattern formation. It is worth noting that is not only intrinsically interesting, but also of significant importance to related problems. In such types of problems, to get the bond strength of adhesives is to measure the force or the work required to separate two surfaces stuck

by a thin adhesive film can be quite successfully evaluated through a Hele-Shaw approach (Darcy's law formulation). In other industrial areas including lubrication, fracture mechanics, chemistry, biology [26], wetting dynamics, colloidal hydrodynamics [27] and oil recovery [28], lifting radial Hele-Shaw flow plays very important role.

Unlike the traditional Hele-Shaw cells of a constant gap, in such a lifting version the upper plate of the cell is moved upwards uniformly at a lifting velocity, i.e., the plates remain parallel to each other during the lifting process, while the lower plate of the cell is held fixed. The morphology of the emerging structures is characterized by the competition among inward moving fingers. To create complex viscous finger in lifting radial Hele-Shaw flow [19, 20, 22, and 29] the more viscous fluid is placed at the center of a Hele-Shaw cell, surrounded by a less viscous fluid, and the upper cell plate is moved upwards. The pressure gradient within the more viscous fluid is due to the lifting of the upper plate, the fluid-fluid interface moves inwards allowing the penetration of multiple fingers of the outer. Interesting variation of the radial Saffman-Taylor problems Hele-Shaw cells with variable gap spacing are presented which are different to with a constant gap and need to be investigated.

As the lifting radial Hele-Shaw flow where the upper plate is lifted just by one edge, making the gap both time and space dependent, where so that the gap is a function of time, but not of space. This defines the so-called *time-dependent gap Hele-Shaw cell*. Shelley *et al.* [29] have shown the Saffman-Taylor instability for stretch flow in rectangular geometry Hele-Shaw cells is valid both with and without surface tension, where the pressure gradient within the fluid is due to the lifting of the upper plate at a specified rate. Different kinds of pattern arise in the lifting Hele-Shaw flow where the cell's gap varies with time. Ben-Jacob *et al.* [30] investigated the stability of lifting Hele-Shaw cell with rectangular geometry by experiment

obtain at low lifting rate finger formed, while the lifting velocity is increased, fingers become dendrites; and the spacing of the dendrites decreases as the lifting velocity is increased. Zhang *et al.* [31] performed a linear stability analysis of the issue and derived the basic equations of the directional solidification problem. Linder *et al.* [32] studied fingering patterns and lifting forces of a thin layer of Newtonian liquid in both numerical simulations and experiments. They have found the number of fingers is sole determined by the surface tension and the extent of fingers growth depends not only on control parameter but also on initial conditions.

A somewhat simpler radial geometry situation has been extensively studied, both experimentally and theoretically. Miranda and Oliveira [33] replaced the thin film with conventional adhesive material to a high viscosity ferrofluid between two narrowly spaced parallel flat plates a subjected to an external magnetic field. The work by Dias and Miranda [34] showed an example that finger competition is restrained as the gap width scale with time with exponent $-2/7$ by linear stability analysis. For this particular situation, it has been shown that finger competition is restrained leading to a more ordered array of fingers. Chen *et al.* [9] studied have noted that time-dependent gap miscible flow in lifting Hele-Shaw cells leads to intricate morphologies if the cell's gap width grows exponentially with time can create more vigorous fingering process.

1.2 Objective and Organization of This Thesis

The literature reviewed above describes the viscous fingering in injection and lifting Hele-Shaw cell through experimental and theoretical work. Different viscosity profiles may lead to a variety patterned structures at the fluid-fluid interface. However, the effect related to finger shape selection in radial geometry is not clear. In this study, therefore, we carried out the

highly accurate pseudospectral method to investigate the interfacial evolution assuming that the fluids involved are miscible. Performing a systematic study of the unstable phenomenon obtained for different values of the relevant control parameters.

The thesis is organized as follows:

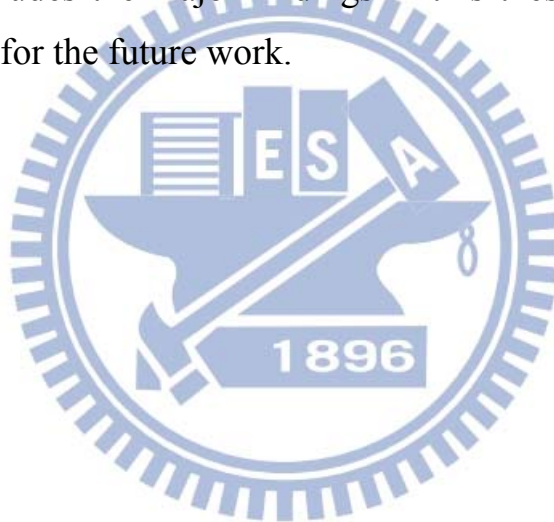
Chapter 2 formulates our theoretical approach and presents the physical problem governing equations of the radial injection flow and time-dependent gap Hele-Shaw cell that the fluids involved are miscible flow with monotonic and nonmonotonic viscosity profiles, respectively. A highly accurate pseudospectral method is employed in this thesis to solve those governing equations.

Chapter 3 investigates the vigorous fingering phenomena in injection-driven miscible flow with monotonic and nonmonotonic viscosity profiles, respectively. We focus on the influence of four kinds of viscosity profiles on the interface dynamics: vary-monotonic (include concave, linear and convex) and nonmonotonic viscosity profile. Various parameters, such as the convection to dispersion ratio and the overall viscosity contrast of both monotonic and nonmonotonic viscosity profile, and local maximum viscosity contrast and position of local maximum viscosity for nonmonotonic viscosity profile, are also analyzed systematically. Result of this study showed that as the overall viscosity contrast held constant, nonmonotonic viscosity profile lead to a more stable flow than monotonic one, and there are no significant differences in different monotonic viscosity profiles. However, if the nonmonotonic viscosity profile crosses the convex monotonic viscosity profile, the nonmonotonic feature enhances the prominence of interfacial instability.

Chapter 4 focuses on study the morphologies in lifting Hele-Shaw cells. We investigate the effectiveness of time-dependent gap width assuming that the fluids involved are miscible. Splitting, merging and competition of

fingers are all inhibited. The sensitivity of the system to changes in the initial conditions and Péclet numbers is also discussed. The influence of the four viscosity profiles as discussed in Chapter 3 has been studied again on the interface dynamics. Consistently, higher Péclet number Pe and viscosity contrast (A in monotonic viscosity profile and μ_m in nonmonotonic one, respectively) demonstrate more vigorous fingering. The stability of three monotonic viscosity profiles is always in the series of concave, linear and convex. As the nonmonotonic viscosity profile across the convex monotonic viscosity profile, demonstrates more vigorous fingering than concave viscosity profile.

Chapter 5 concludes the major findings in this thesis and outlining the recommendations for the future work.



Chapter 2 General Feature

2.1 Physical Problem

To investigate the phenomenon of viscous finger, we can simplify the complex geometries such porous media to a narrow gap between closed-spaced parallel plates. Consider a packed column of length L initially filled with displaced fluid and injecting fluid, which is schematically showed in Fig. 1. When the injecting fluid displaced fluid in porous media, the difference between the viscosity and the density arise flow instability. The pressure drop ΔP is constant along the column, and k is the permeability. Darcy's equation for a porous medium is expressed as [36]:

$$u = \frac{k}{\mu} \left(-\frac{\partial P}{\partial x} + \rho \delta g \right) = \frac{k}{\mu} \left(\frac{P_{in} - P_{out}}{L} + \rho \delta g \right). \quad (1)$$

Figure 1 schematically shows the interface between the two fluids along the column. Section A is the main, unperturbed zone, and a small part section B perturbs the interface ahead of (or behind) the column cross-section. Considering the liquids in sections A and B are incompressible, the velocity of injecting flow is the same as that of displaced flow, but the flow velocity u_A is not equal to u_B . Flow instability may arise from the viscosity difference, but also from the density difference when the upper fluid is denser than the lower fluid. The difference in velocity between u_A and u_B was down by Rousseaux *et al.* [37] is expressed as:

$$u_A - u_B = \frac{k}{[\mu_1(z/L) + \mu_2(1-(z/L))]} \times \left[\frac{u_B}{k} (\mu_1 - \mu_2) - \delta g (\rho_1 - \rho_2) \right] \frac{\delta z}{L} \quad (2)$$

The flow is unstable when $u_B > u_A$ for $\delta z > 0$. From Eq. (2), the denominator of this equation is positive, then the stability criterion

expressed as:

$$\underbrace{\frac{u_B}{k}(\mu_1 - \mu_2)}_{\text{viscosity effect}} - \underbrace{\delta g(\rho_1 - \rho_2)}_{\text{density effect}} > 0 \quad (3)$$

It contains the viscosity effect and the density effect. To avoid gravity effect, Hele-Shaw [38] suggested considering a flow between two parallel horizontal plates with a narrow gap between them. Therefore, only the viscosity effect is conceded. In general, if the injecting fluid is less viscous than the displaced one, this unfavorable viscosity contrast makes viscous fingers and causes the system unstable.

Consider the control volume which is across the interface shown in Fig. 2 to explain the stability criteria. For a fluid with positive perturbation u' and increasing concentration c' , which in turn leads to changes in the viscosity change μ' are $\mu'_1 = \left(\frac{d\mu}{dc}\right)\bigg|_{c=1} c'$ and $\mu'_2 = \left(\frac{d\mu}{dc}\right)\bigg|_{c=0} c'$, the fluid is initially stable while the pressure difference $\delta P = -(\mu'_1 + \mu'_2)Udx < 0$. This indicates with the requirement that for a stable flow, and we obtain the criteria for $(\mu'_1 + \mu'_2) > 0$.

However, as a result of nonlinear interactions between the fingers, the stability of the flow depends not only on the end-point viscosity contrast, but also on the derivatives of the viscosity with respect to concentration. It is difficult to predict the nonlinear behavior of the viscous finger. This may represent an experimental challenge because the fluids may get mixed up before the injecting and lifting start, or undesirable air bubbles can be trapped between the plates. A general solution is needed to understand the growth of different fluid system.

2.2 Governing Equations

2.2.1 Viscosity Profile

The viscosity μ in the mixing zone is supposed to be a function of the injecting fluid concentration expressed as Eq. (4):

$$\mu = \mu(c). \quad (4)$$

Following other researchers (e.g. Tan and Homsy [23] and Rogerson Meiburg [39]), the viscosity dependence on the monotonic case, concentration has the form (e.g. Tan and Homsy [2]; Chen and Meiburg [4]) as: (see Appendix 1 a.)

$$\mu_{mono}(c) = e^{R(1-c)}, R_{mono} = -\frac{1}{\mu} \frac{d\mu}{dc} = \ln\left(\frac{\mu_2}{\mu_1}\right), A = \frac{e^R - 1}{e^R + 1}. \quad (5)$$

To confirm the stability of various viscosity profiles as stated before, scholars have defined and studied monotonic and nonmonotonic viscosity profiles, respectively. While considerable attention has been paid in the past to the effect of different viscosity profiles with nonmonotonic to fluid stability, the issue of variable monotonic viscosity profile has never been investigated. Follow the monotonic sense, recreate two convex and linear monotonic viscosity profiles expressions as equation (6) and (7), where the subscripts *vex* and *linear* are indicated, respectively. We thus obtain

$$\mu_{vex}(c) = \frac{\mu_2}{\mu_1} - \frac{\frac{\mu_2}{\mu_1}}{\exp\left(\ln\left(\frac{\mu_2}{\mu_1}\right) \times (1-c)\right)} + 1, \quad (6)$$

$$\mu_{linear}(c) = \alpha - \alpha c + c. \quad (7)$$

The viscosity-related parameter in the stability equation takes the form (8) and (9), respectively (see Appendix 1 b. and c.).

$$R_{vex} = \frac{1}{\left(\alpha - \frac{\alpha}{\exp(R \times (1-c))} + 1 \right)} \left(\frac{-\alpha R}{\exp(R \times (1-c))} \right), \quad (8)$$

$$R_{linear} = \left(\frac{1}{\alpha - \alpha c + c} \right) (1 - \alpha). \quad (9)$$

The nonlinear evolution of viscous fingering instabilities in miscible displacement flows with nonmonotonic viscosity-concentration profile of the alcohol-water mixtures have been investigated first by Manickam and Homsy [10]. The nonmonotonic viscosity profiles are characterized by the interplay of the maximum viscosity μ_m , the location of the maximum viscosity c_m , and the end-point viscosities contrast α . Different viscosity-concentration relationships may result in different fluid configuration. In order to be able to compare results of previous studies on nonmonotonic flows, we employ the same functional relationships between viscosity and concentration which has investigated by Manickam and Homsy [10]. It has defined a simple sine function modified through a sequence of transformation by the expressions as Eqs. (10)-(16).

$$\mu_{non}(c) = \mu_m \sin(\gamma), \quad (10)$$

$$\gamma = \gamma_0(1 - \beta) + \gamma_1\beta, \quad (11)$$

$$\beta = \frac{(1+a)c}{1+ac}, \quad (12)$$

$$\gamma_0 = \sin^{-1}(\alpha/\mu_m), \quad (13)$$

$$\gamma_1 = \pi - \sin^{-1}(1/\mu_m), \quad (14)$$

$$a = \frac{c_m - \beta_m}{c_m(\beta_m - 1)}, \quad (15)$$

$$\beta_m = \frac{\frac{1}{2}\pi - \gamma_0}{\gamma_1 - \gamma_0}. \quad (16)$$

The viscosity μ is supposed to be a function of the injecting fluid concentration, which is a sine function modified and has the end-point viscosities $\mu(0)=\alpha$, $\mu(1)=1$, schematically show the shape of the class of viscosity profile considered. When $\alpha < 1$, the flow has a favorable end-point viscosities contrast, as a high viscosity fluid displaces a low viscosity fluid, and $\alpha > 1$, the flow is said to have an unfavorable end-point viscosities contrast to indicate the reverse scenario. It is given the maximum viscosity value of μ_m located at $c=c_m$. In $c_m > 0.5$ case, the maximum viscosity is located closer to the injecting fluid, and is closer to the displaced fluid otherwise.

In the nonmonotonic case, the viscosity-related parameter $R_{non}(\mu)$ in the stability equation takes the form as: (see Appendix 1 d.)

$$R_{non}(\mu) = -\frac{1}{\mu} \frac{d\mu}{dc} = (\gamma_1 - \gamma_0) \frac{1+a}{(1+ac)^2} \cot(\gamma) \quad (17)$$

2.2.2 Injection-Driven Radial Hele-Shaw flow

Consider a Hele-Shaw cell of constant gap thickness h containing two miscible, incompressible, viscous fluid (Fig. 3). Miscible displacements are characterized by negligible surface tension, so the interplay of diffusive, convective, and viscous effects dictate the pattern formation behavior. Denote the injecting fluid of viscosity μ_1 displaces the displaced fluid of viscosity μ_2 at a given injection rate Q , equal to the area cover per unit time. Further, we assume two fluids mix in all proportions. The concentration of the injecting fluid is represented by c . Assume the permeability and the physical dispersion to be homogeneous and isotropic. Solve the unstable,

steady, incompressible flow generated by a miscible displacement process under Darcy's law expressed as:

Continuity equation:

$$\nabla \cdot u = \frac{\partial u}{\partial x} + \frac{\partial u}{\partial y} = 0 \quad (18)$$

Hele-Shaw equation (see Appendix 2):

$$\nabla p = \frac{\partial p}{\partial x} = -\frac{12\mu}{h^2}u \quad (19)$$

Convection/dispersion equations:

$$\frac{\partial c}{\partial t} + u \cdot \nabla c = \frac{\partial c}{\partial t} + u \frac{\partial c}{\partial x} + v \frac{\partial c}{\partial y} = D\nabla^2 c \quad (20)$$

D is the constant isotropic diffusion coefficient. The governing equations (18)–(20) are rendered dimensionless by taking the lateral extent L of one unit of the flow field as the characteristic length scale. With the source strength Q , choose the following parameters as characteristic scale to make governing equation dimensionless:

$$\begin{aligned} t^* &= \frac{2\pi L^2}{Q}, \\ u^* &= \frac{Q}{2\pi L}, \\ p^* &= \frac{6\mu_1 Q}{\pi h^2}. \end{aligned} \quad (21)$$

The dimensionless equations (18)–(20), omitting the asterisks, can be expressed in terms of the total velocity u , pressure p , and concentration c . The dynamical evolutions of the system are the traditional gap average Hele-Shaw flow equations expressed as:

$$\nabla \cdot u = 0, \quad (22)$$

$$\nabla p = -\mu u, \quad (23)$$

$$\frac{\partial c}{\partial t} + u \cdot \nabla c = \frac{1}{Pe} \nabla^2 c. \quad (24)$$

Here the Péclet number Pe can be interpreted as a dimensionless flow rate,

$$Pe = \frac{Q}{2\pi D}, \quad (25)$$

which is a measure of the relative importance of advection to diffusion.

By employing such an approach, we rewrite the gap average velocity in Eq. (23) as:

$$u = u_{rot} + u_{pot}, \quad (26)$$

where u_{rot} is the rotational component of the velocity, and u_{pot} represents its potential component, respectively. The rotational part of the velocity is smooth and can be obtained with highly accurate pseudospectral method, while the potential part induced by injection is related to a flow singularity at a source located at the origin, making accurate computations more difficult near these locations. To avoid numerical instabilities near $r=0$, we smooth out the point source by distributing its strength in a Gaussian way over a small circular core region. Accomplishing this, we consider a ‘‘Gaussian source’’ [40] which is characterized by a core size $\sigma=0.075$. In addition, the initial condition is assumed as an initial fluid core of radius of $r_i=0.1$. Under the circumstances of constant injection rate, the dimensional injected area at a given time can be written as $A=Qt$. In this case, the dimensionless potential radial velocity satisfying these requirements can be expressed as:

$$u_{pot} = \frac{1}{r} [1 - \exp(-r^2 / \sigma^2)] \hat{r}, \quad (27)$$

where \hat{r} denotes the unit vector along the radial direction.

A fully explicit third order Runge-Kutta procedure on time and spatial sixth order compact finite difference schemes are employed to solve the concentration Eq. (24) and will be discussed in Section 2.3.

In order to solve the vorticity equations (24) numerically, we define the total stream function [5] of the system as

$$\phi = \phi_{rot} + \phi_{pot} \quad (28)$$

where ϕ_{rot} and ϕ_{pot} denote the rotational and potential stream functions, respectively. Since $\nabla^2 \phi_{pot} = 0$, we end up with the equations of

$$u_r = \frac{\partial \phi}{\partial y}, \quad v_r = -\frac{\partial \phi}{\partial x}, \quad \nabla^2 \phi = -\omega. \quad (29)$$

In the present simulations, we take $c_0(x)$ from the one-dimensional similarity solutions provided by Tan & Homsy [1] as well as Yortsos [44] for radial source flow at initial time t_i . The starting time t_i of the simulation is taken to be non-zero, in order to avoid a singular initial concentration profile. Suitable initial condition can be specified as

$$\phi(x, t = t_i) = \phi_{pot}(x), \quad (30)$$

$$c(x, t = t_i) = c_0(x). \quad (31)$$

Furthermore, to break the unphysical fingering symmetry, an initial condition such as a small magnitude of random perturbations which is produced by Matlab is applied to the positions at $c = 0.5$. The influence of perturbation on the simulation results will be discussed in Section 4.2.

The symmetry boundary conditions at the sides now are

$$x = \pm 1, \quad \phi = 0, \quad \frac{\partial c}{\partial x} = 0, \quad (32)$$

$$y = \pm 1, \quad \phi = 0, \quad \frac{\partial c}{\partial y} = 0. \quad (33)$$

To reproduce the extremely fine structures of the fingers, a highly

accurate pseudospectral method which will be discussed later is employed. As a result, the actual boundary conditions applied in the numerical code are $\partial\phi/\partial y = 0$ at $y = \pm 1$, where no concentration gradient is generated on the boundary. The condition $\phi = 0$ could be imposed at the boundary. To ensure this condition, all the simulations are terminated when the inner fluid reaches the boundary.

An alternative and more quantitative account of the role played by the parameters in determining the behavior of the evolving mixing interface is offered by the growth of a characteristic quantity related to the mixing boundary region. The mixing region between two miscible fluids is not a well-defined sharp interface, in the region of significant concentration gradient. Chen and Meiburg [4] provides a good measure of the overall length $L(t)$ of the interface between injecting and displaced fluid can be represented as Eq. (34)

$$L(t) = \int_0^1 \int_0^1 \sqrt{\left(\frac{\partial c}{\partial x}\right)^2 + \left(\frac{\partial c}{\partial y}\right)^2} dx dy. \quad (34)$$

Normalized mixing interfacial length $L_B(t)$ scale as Eq. (35), which is the initial circular pattern (base state) at a given time, expresses the ratio of the length of the diffuse interface to the perimeter of base state $L_n(t)$ as (36).

$$L_B(t) = 2\pi\sqrt{2(t + 0.005)}, \quad (35)$$

$$L_n(t) = \frac{1}{L_B(t)} \int_0^1 \int_0^1 \sqrt{\left(\frac{\partial c}{\partial x}\right)^2 + \left(\frac{\partial c}{\partial y}\right)^2} dx dy. \quad (36)$$

2.2.3 Time-dependent Gap Hele-Shaw Cell

Consider a Hele-Shaw cell of a time-depended gap width $h(t)$, containing two miscible, incompressible, viscous fluid is sketched in Fig. 4.

Unlike the traditional Hele-Shaw cell illustrated in Fig. 3 of a constant gap thickness h , in such a lifting version, the upper plate of the cell is

moved upwards uniformly at a lifting velocity, while the lower plate of the cell is held fixed. Denote the outer fluid of viscosity μ_1 displaces the inner fluid of viscosity μ_2 , and the concentration of the outer fluid is represented by c . Assume two fluids mixing in all proportions, and the permeability and the physical dispersion to be homogeneous and isotropic. During the lifting process the plate always parallels to each other. For the initial gap thickness $h_{t=0}=h_0$, the gap is a function of time, but not space. The initial fluid-fluid diffusive interface is circular, having radius $R_{t=0}=R_0$. Initially, a more viscous fluid is placed at the center of a Hele-Shaw cell, surround by a less viscous fluid.

The dynamical evolution in a time-dependent gap Hele-Shaw cell is governed by the follow equations in Refs. [26, 31, 39, 41, and 42]:

Continuity equation:

$$\nabla \cdot u = -\frac{\dot{h}(t)}{h(t)} \quad (37)$$

Hele-Shaw equation:

$$\nabla P = -\frac{12\mu}{h^2}u \quad (38)$$

Convection/dispersion equations:

$$\frac{\partial c}{\partial t} + u \cdot \nabla c = D\nabla^2 c \quad (39)$$

Like the injection cases discussed in the chapter 2.2.1, the concentration of the outer fluid is represented by c . In order to render the governing equation (37)-(39) dimensionless in Refs. [5, 6], we assume an exponential increasing gap width as:

$$h_{\text{exp}}(t) = h_0 e^{(\gamma t)}, \quad (40)$$

where γ is a control parameter. Take the initial radius R_0 as the characteristic length scale. Here the gap averaged Hele-Shaw

dimensionless expressions are a bit different from these presented in the injection-driven fluid [Eqs. (18)-(20)]. Here the gap averaged Hele-Shaw dimensionless expression to the time variation of the cell gap spacing is as:

$$\nabla \cdot u = -1, \quad (41)$$

$$\nabla P = -\frac{\mu}{e^{2t}} u, \quad (42)$$

$$\frac{\partial c}{\partial t} + u \cdot \nabla c = \frac{1}{Pe} \nabla^2 c. \quad (43)$$

Defines a Péclet number for the lifting flow situation as:

$$Pe = \frac{\gamma R_0^2}{D}. \quad (44)$$

Further scale the viscosity with μ_l and time with l/γ , respectively. The following parameters make governing equation dimensionless

$$P = \frac{12\mu_l \gamma R_0^2}{h_0^2}, \quad (45)$$

$$u = \gamma R_0. \quad (46)$$

The velocity is split into a divergence free component u_f which is the rotational velocity of the constant gap spacing case, and an axisymmetric divergent radial, potential velocity $u_d = u_d(r)$ caused by the gap variation, so that

$$u = u_f + u_d, \quad (47)$$

$$\nabla \cdot u_f = 0, \quad u_f = \frac{\partial \phi}{\partial y}, \quad v_f = -\frac{\partial \phi}{\partial x} \quad (48)$$

$$\nabla \cdot u_d = -1. \quad (49)$$

The divergent radial velocity is obtained directly from Eq. (49) as $u_d = -r/2$, which is a potential field. Similar to the injection-driven case, the divergence free component u_f can be obtained by solving Eqs. (29) where u and v are the components of the velocity vector u along the x and y

directions. Notice that the velocities refer to the x - y components of the rotational velocity (u_r, v_r). The numerical scheme is similar to injection which will be discussed in the Section 2.3, we will not discuss again. Following Ref. [34] for the variant dimensional lifting situation we consider that

$$h_v(t) = \frac{h_0}{(1 - \delta t)^{2/7}}, \quad (50)$$

where δ is a control parameter with an inverse dimension of time. We utilize the same set of characteristic scales used in the exponential lifting situation to obtain the corresponding governing equations for the variant lifting case. In this context, the dimensionless continuity equation takes the form as

$$\nabla \cdot u = -\frac{2a}{7(1 - at)}, \quad (51)$$

but Eqs. (42) and (43) remain unchanged. Note the definition of an additional dimensionless parameter, namely the lifting ratio $a = \delta/\gamma$. Likewise, in dealing with the variant lifting situation, Eqs. (47) and (48) are unaltered, but Eq. (49) is replaced by

$$\nabla \cdot u_d = -\frac{2a}{7(1 - at)}. \quad (52)$$

The divergent radial velocity is obtained directly as

$$u_d = -\frac{ar}{7(1 - at)} \hat{r}, \quad (53)$$

which is a potential field.

The mixing interfacial length be represented in [50] are moderated from Eqs.(34)-(36),

$$L_n(t) = \frac{1}{L_0} \int_0^1 \int_0^1 \sqrt{\left(\frac{\partial c}{\partial x}\right)^2 + \left(\frac{\partial c}{\partial y}\right)^2} dx dy, \quad (54)$$

L_0 is the initial interfacial length.

As to the boundary conditions, the non-vanishing divergence-free stream function given by Eq. (28) is induced by concentration gradients. Consequently, for regions located outside the droplet (where no concentration gradient is presented), the stream function is zero. Therefore, the choice of computational domain is arbitrary as long as the domain contains the whole droplet. Of course, the divergent radial component is still presented within the entire computational domain. In order to reproduce the very fine structures of the fingers successfully, we choose the boundaries to vary between $+4/3$ and $-4/3$ in both x and y directions. Under such circumstances, the boundary conditions are prescribed as follows:

$$x = \pm \frac{4}{3}; \phi = 0, \frac{\partial c}{\partial x} = 0, \quad (55)$$

$$y = \pm \frac{4}{3}; \phi = 0, \frac{\partial c}{\partial y} = 0. \quad (56)$$

The simulations are terminated when the $h/h_0 = 4$. This is done to the definition to Hele-Shaw cell with a narrow gap.

2.3 Numerical Scheme

To address the issue in Section 2.2.2, the stream function (ϕ) and vorticity (ω) formulation by Josselin and Jong [46] is employed. In this way, the continuity equation is satisfied identically, and the governing set of the Eq. (24) takes the form

$$c_t + \phi_y c_x - \phi_x c_y = \frac{1}{Pe} \nabla^2 c \quad (57)$$

A fully explicit third-order Runge-Kutta procedure on time is utilized, so by writing the concentration equation as

$$\frac{\partial c}{\partial t} = F(c), \quad (58)$$

so that

$$c_{i,j}^g = c_{i,j}^{g-1} + \Delta t [v_g F(c_{i,j}^{g-1}) + \eta_g F(c_{i,j}^{g-2})], \quad (59)$$

where

$$\begin{aligned} v_1 &= \frac{8}{15}, \eta_1 = 0, \\ v_2 &= \frac{5}{12}, \eta_2 = -\frac{17}{60}, \\ v_3 &= \frac{3}{4}, \eta_3 = -\frac{5}{12}. \end{aligned} \quad (60)$$

with

$$|g| < \frac{N}{2},$$

where N is the number of grid points in the longitudinal direction. The simulations to be discussed below typically employ discretization of 513×513 grid points.

Recast Eq. (23) into the well-known vorticity formulation (see Appendix 1), yielding

$$\omega = \frac{1}{\mu} \frac{d\mu}{dc} \left(u \frac{\partial c}{\partial y} - v \frac{\partial c}{\partial x} \right) = \frac{1}{\mu} \frac{d\mu}{dc} (\nabla \phi \cdot \nabla c) = -R (\nabla \phi \cdot \nabla c). \quad (61)$$

The parameter R is chosen from Eqs. (5), (8), (9), and (17) which correspond to different kind of viscosity profile. The streamfunction (ϕ) and vorticity (ω) are employed a Galerkin-type discretization expanded in a cosine series in the x direction as Eq. (62)-(63).

$$\phi(x, y, t) = \sum_g \hat{\phi}_g(y, t) \cos[2\pi g x], \quad (62)$$

$$\omega(x, y, t) = \sum_g \hat{\omega}_g(y, t) \cos[2\pi g x], \quad (63)$$

To solve the stream function Eq. (29) and (61), the elliptic Poisson equation for the determination of the rotational component of the stream

function from the vorticity distribution can be solved fast and efficiently on the basis of fast Fourier-Galerkin scheme. In the y -direction, discretization is accomplished by sixth order compact finite differences. In the x -direction, discretization is accomplished by pseudospectral method.

The spatial discretization of the governing equation is based on the compact finite difference schemes in the form given by Lele [45]. When the first derivatives contained in the convection terms that appear explicitly, the sixth-order formulation is

$$\xi_1 f'_{i-1} + f'_i + \xi_1 f'_{i+1} = b_1 \frac{f_{i+2} - f_{i-2}}{4\Delta} + a_1 \frac{f_{i+1} - f_{i-1}}{2\Delta}, \quad (64)$$

with

$$\xi_1 = \frac{1}{3}, a_1 = \frac{14}{9}, b_1 = \frac{1}{9}. \quad (65)$$

Here, Δ indicates the mesh size, which is identical in the x and y direction. We apply the second derivatives of the diffusion terms is

$$\xi_2 f''_{i-1} + f''_i + \xi_2 f''_{i+1} = b_2 \frac{f_{i+2} - 2f_i + f_{i-2}}{4\Delta^2} + a_2 \frac{f_{i+1} - 2f_i + f_{i-1}}{\Delta^2}, \quad (66)$$

with

$$\xi_2 = \frac{2}{11}, a_2 = \frac{12}{11}, b_2 = \frac{3}{11}. \quad (67)$$

2.4 Validation

Rigorous validation represents an important step in establishing the accuracy and convergence properties of a novel numerical approach. However, not only the viscosity profiles we studied are very complicated, but an experimental challenge because the fluids may get mixed up before the injecting and lifting start or undesirable air bubbles can be trapped between the plates. We cannot compare with experiment data.

Our numerical code is largely similar to the one used for earlier investigations on planar fronts with monotonic viscosity profile [7], is validated by comparing the growth rate of small perturbations with the respective values obtained from linear stability theory by Tan and Homsy [1]. In other words, in contrast to other investigation of the Hele-Shaw problem for immiscible with rotation where a more physical correlation would be desired [47], which have been validated by comparing the numbers of finger obtained in Ref. [48]. These simulated morphological in suction flow [49] also attributes very well with existing experiment [51]-[54] and other numerical simulation, as well as with other numerical simulations [55], have gotten excellent agreement.



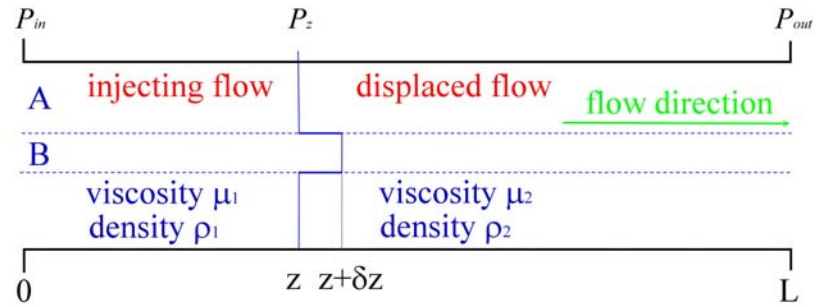


Figure 1: Schematic illustration of a perturbation of the interface between two fluids in Hele-Shaw cell, the injecting flow₁ pushes the displaced flow₂.

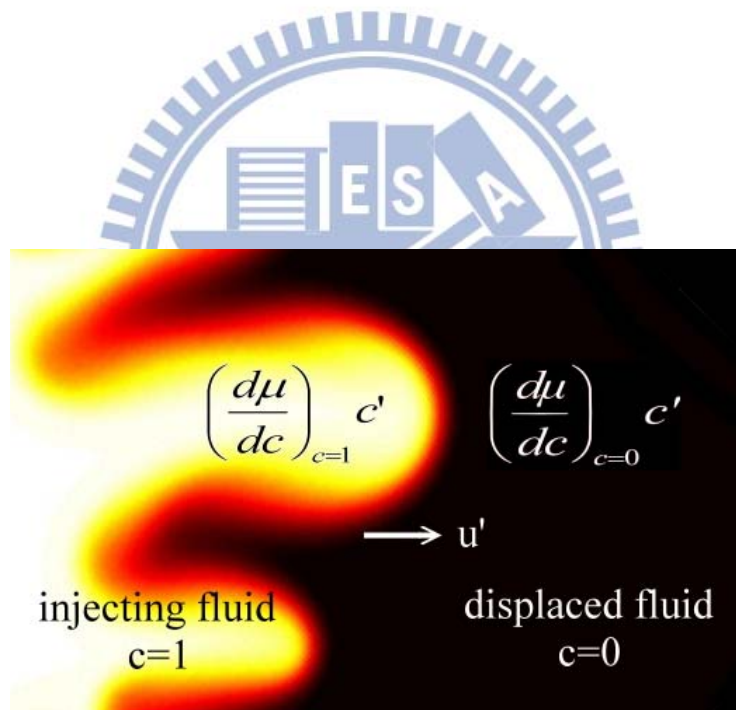


Figure 2: A physical interpretation of the stability criteria.

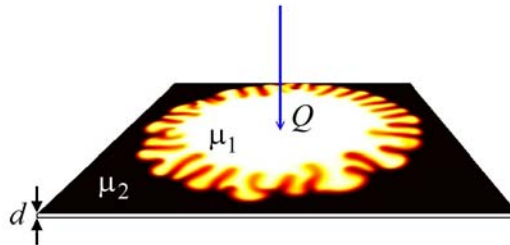


Figure 3: Schematic setup for an injection-driven miscible radial flow in Hele-Shaw cell with cell gap h . The fluid 1 is injected at the center with a flux Q . Viscosities of the injected fluid 1 and the displaced fluid 2 are denoted as μ_1 and μ_2 , respectively.

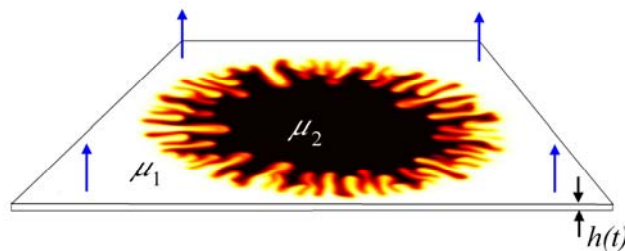


Figure 4: Schematic setup of the time-dependent gap radial Hele-Shaw flow with miscible fluids. The upper plate of the cell is lifted, so that the gap of the cell is variable. The inner fluid is more viscous ($\mu_2 > \mu_1$).

Chapter 3 Fingering Instability of Miscible Injection Hele-Shaw Flows

3.1 Monotonic Viscosity Profile

To begin with our numerical investigation, we perform a systematic study of the concentration images obtained from different viscosity profiles. Chen *et al.* [6] and most of recent studies in the outward radial flow, in which one of the fluids is injected into the Hele-Shaw cell with monotonic viscosity profile, have demonstrated that more vigorous finger is observed at higher Pe and larger A . Other types of monotonic viscosity profiles redefined by us will be discussed later.

To study the effect of different viscosity profiles, a nonmonotonic viscosity profile is provided to compare with the monotonic viscosity profiles, concave, linear, and convex are depicted in Fig. 5 for comparison. In order to minimize the impact of μ_m , let the μ_m equal of $\alpha + 0.001$, and c_m set to 0.03 so as to ensure that nonmonotonic viscosity profile is not across the aforementioned three monotonic viscosity profiles. To compare with the monotonic viscosity profiles as stated before, we rename monotonic and nonmonotonic viscosity profile to concave and quasi-monotonic one, respectively. A picture of the four viscosity profiles are depicted in Fig. 5. The concentration images of four viscosity profiles shown as Fig. 5 at $t=0.30$ are depicted in Fig. 6 and time evolution of the interfacial length shows in Fig. 7 with $Pe=800$, respectively.

It can be observed that although a linear and convex viscosity profile tends to widen the finger tip, but the morphology of three monotonic viscosity profiles are very similar. However, we simulated over a broad

region in parameter space before our numerical code become unstable and found that the differences in concentration images and time evolution of the interfacial length between three types of monotonic viscosity profiles are quite small. Result of this study showed that as the overall viscosity contrast held constant, nonmonotonic viscosity profile led to a more stable flow than monotonic one. Likewise appear in the study of monotonic viscosity profiles, although we modified as A varies from 0 to 1, there were no significant differences in different viscosity profiles. However, if the nonmonotonic viscosity profile was across the convex monotonic viscosity profile, the nonmonotonic feature enhanced the prominence of interfacial instability.

3.2 Nonmonotonic Viscosity Profile

We now turn our attention to the influence of physical parameters to the nonmonotonic viscosity profile for miscible radial Hele-Shaw flow. The original definition of this profile given by Manickam and Homsy [10] divided it into an unstable zone (from injection fluid to the viscosity maximum) and a stable zone (from the viscosity maximum to displaced fluid) illustrated in Fig. 8, respectively. Both of zones affect the fluid. In particular, Pankiewitz and Meiburg [19] suggested the unstable zone has the ability to trigger an overall instability, and the stable zone of the viscosity profile acts as a barrier for the forward growth of fingers. However, detailed discussions of the viscosity profile and stabilization in a radial Hele-Shaw cell have not been found. Therefore we focus our effort in the effect of the relation. The stability of the flow is investigated and a criterion for instability is formulated in favorable and unfavorable viscosity contrast, respectively. We simulated miscible displacement over a broad region in parameter space before our numerical code became unstable and

discussed the results to the stability problem.

3.2.1 Influence of the Péclet number Pe

The value of Pe is directly proportional to the flow rate. Small flow rate provides diffusion with enough time to smear out the concentration field, whereas, for larger flow rate, steeper concentration gradient can be maintained. Its influence can be analyzed by discussing a series of simulations employing different values of Pe for which c_m , α and μ_m are held constant. The increase in the value of the Péclet number provides stronger concentration gradients that enhance finger penetration and lead to more fingering. This finding is easily verified in Fig. 9, in term of both with unfavorable or favorable viscosity profile.

For Pe variation between 200 and 800 with increments of 200, meaning weaker diffusive effects or faster injection rate, the width of viscous fingers tends to get thinner and the number of finger become more with increasing Pe -value. The unfavorable end-point viscosity contrast ($\alpha=2$) in the top of Fig. 10 is the inverse of the bottom one with favorable end-point viscosity contrast ($\alpha'=1/\alpha=0.5$), depicting that the lengths of fingers in unfavorable viscosity profile are longer than favorable ones. The particular phenomenon of “reverse” fingering where the fingers spread farther in the backward direction than the forward are observed. We can also find comparing the interfacial length illustrated in Fig. 11, that higher Pe will get higher L_n if other parameters held constant. It means that larger Pe -value gives a rise in a fingering instability.

Tan and Homsy [1] had found that each viscosity profile in nonmonotonic case has a critical value Pe_c , can identify, above which the flow is unstable. Below the Pe_c , viscous finger is not obvious and the concentrate image is a circle before breakthrough. It is also found that L_n almost equals to 1 as time progresses. The phenomenon indicates that a

nonmonotonic viscosity profile can be stable, no matter whether the end-point viscosity is unfavorable or favorable end-point viscosity contrast.

3.2.2 Influence of the maximum viscosity μ_m

The maximum value of the viscosity is given by μ_m and the maximum occurs at $c=c_m$. Higher value of the maximum viscosity μ_m means that the injecting fluid would push a lower mobility displaced fluid. It has an intuition that the fluid will flow slower because higher μ_m will decrease the tip velocity and the front become thicker, but higher μ_m also increases the derivate between the injecting fluid and μ_m , causing the fluid more unstable. Pankiewitz and Meiburg [19] discovered that for a given end-point viscosities contrast, an increase in the maximum viscosity generally leads to a more unstable flow, regardless of whether the overall viscosity ratio is favorable or unfavorable. However, contrasting to Manickam and Homsy [10] numerically showed that in rectilinear displacement, a higher maximum viscosity generally stabilizes flow with an unfavorable end-point viscosity contrast.

It is to be kept in mind that all of the above investigations dealt with rectilinear and quarter five-spot displacements, whereas our present study focuses on the nonlinear flow characteristic of radial flow. We use the largest value μ_m for which our numerical code remains stable for $\mu_m=14$ with an unfavorable viscosity profile ($\alpha= 3$ and $c_m=0.1$) and $\mu_m=9$ with a favorable viscosity profile ($\alpha= 0.2$ and $c_m=0.2$). The viscosity profiles are illustrated in Fig. 8, respectively. By analyzing Fig. 12 which depicts the concentration images at $t=0.30$, we obtained for increasingly larger values of the maximum viscosity μ_m , the occurrence of fingerlike structures which split at their tips. The length of fingers will increase with the maximum value of the viscosity, respectively.

Figure 13 illustrates the vorticity images of Fig. 12. The result suggested

that higher μ_m tend to be stronger in the recirculating fluid region. It is corresponding to the finding by Pankiewicz and Meiburg [19]. But it is in marked contrast to the above, in which usually only the inner recirculating fluid region exists for unfavorable scenario. Reduced μ_m to 3, the outer ones never becomes visible in the perturbation streamfunction plot. However, we have observed that with favorable end-point viscosities contrast ($\alpha=0.2$) take the $\mu_m=2$, both of the inner and outer recirculating fluid regions are obvious and dual vortex appear. In contrast with unfavorable end-point viscosities contrast ($\alpha=3$), take the $\mu_m=3.001$ slightly higher than end-point viscosities contrast, the outer recirculating fluid regions are obscure, but exactly exist.

Manickam and Homsy [3] suggested that the flow will be unstable if the destabilizing vortices are stronger than the stabilizing ones, but otherwise stable. However, inspecting the vorticity images of Figure 13 and other cases we have done over a broad region parameters space, the destabilizing vortices are always stronger than the stabilizing ones without exception, corresponding to the findings for the radial source flow displacement by Pankiewicz and Meiburg [19]. We also notice that the pair of vortices is more violent for larger μ_m .

Both of inner and outer vortices comprise many two units of adjacent counter-rotating vortices. For this, we borrow arguments similar to Shariati and Yortsos [20]. The vortices in the outer rings of decreasing viscosity in the direction of displacement, any two adjacent counter-rotating vortices bring low viscosity fluid from the downstream to the upstream direction and high viscosity fluid from the upstream to the downstream direction. The first action lowers the resistance to flow in a direction that opposes the instability, while the second one increases the resistance to flow in a direction that enhances the instability. Both of the vortices in the outer rings act to stabilize the flow. Conversely, in the inner rings which are increasing

viscosity in the direction of displacement, act to destabilize the flow. Higher μ_m will cause the vortices both in inner and outer rings more violent. The dimensionless interfacial lengths L_n as a function of time for different μ_m are illustrated in Fig. 14 which depicts the time evolution of the normalized mixing interfacial length L_n for $Pe=400$, with the four sets of viscosity profiles in Fig. 8, both in unfavorable end-point viscosities contrast $\alpha=3$ and $c_m=0.1$ [related to Fig. 12 (a) and (b)]; and in favorable end-point viscosities contrast $\alpha=0.2$ and $c_m=0.2$ [related to Fig. 12 (c) and (d)], and three increasing values of the maximum viscosity value μ_m .

The growth of normalized interfacial length serves as a good indicator for the intensity of fingering at the mixing interface. From Fig. 14, it is evident that the presences of increasingly larger maximum viscosity value μ_m tend to destabilize the diffuse interface. For the μ_m with mature fingers, we observe a very steep growth of L_n at earlier time, followed by its “saturation” for longer time, and we also notice that the slopes of the curves are increased for larger μ_m .

In addition, for all times, the curves for lower μ_m are always below the ones of higher μ_m . Again, this is in accordance with the maximum viscosity value μ_m , which tends to destabilize the mixing interface.

By contrasting these normalized interfacial lengths, we notice that the most noteworthy effect in Fig. 14 the collapse of the curve as $\alpha=0.2$ and $\mu_m=9$ shows a damping effect in favorable end-point viscosity contrast at beginning (during $t=0.0343$ to 0.0729). A time series of the contours on the concentration to the parameters sets are illustrated in Fig. 15. The time interval between contours is 0.02 and the first contour is at $t=0.03$. It can be observed without fingers merge and shield, numbers of fingers do not change, and the length of finger is almost constant but becomes wider after $t=0.0343$. Compare with the length of fingering between $t=0.0343$ and $t=0.0729$ illustrated in Fig. 16 (a) and (b) and it shows no significant

variations. It means that the finger length does not increase as fast as the injection flow. As time longer than $t=0.0729$, as in Fig. 16 (c) at $t=0.11$, it is apparent that the length of fingers are longer than (a) and (b). The phenomenon can interpret damping effect in Fig. 14. We also find that the viscosity contrast and fluid stability do not show any significantly relation with nonmonotonic favorable viscosity profile.

3.2.3 Influence of the location of the maximum viscosity c_m

In the nonmonotonic viscosity profile, the position of the maximum viscosity c_m denotes the place with the lowest mobility. With an increase in c_m , the maximum viscosity μ_m of the viscosity profile will move to injection fluid, vice versa. It is difficult to find the nonlinear effect of the c_m to the stability of fluid. The work of Manickam and Homsy [3] has extended a straight forward parameter Λ which is a quantity for the relation between the slope of injecting fluid ($c=1$) and displaced fluid ($c=0$) is expressed as:

$$\Lambda = -\frac{\left. \frac{d\mu}{dc} \right|_{c=0} + \left. \frac{d\mu}{dc} \right|_{c=1}}{\alpha + 1}, \quad \alpha = \frac{\mu_2}{\mu_1}. \quad (68)$$

In the monotonic viscosity profile, $(d\mu/dc) |_{c=0}$ and $(d\mu/dc) |_{c=1}$ are of the same sign, the unfavorable viscosity contrast ($\mu_1 < \mu_2$) leads to instability ($\Lambda > 0$), and vice versa. In non-monotonic case, $(d\mu/dc) |_{c=0}$ and $(d\mu/dc) |_{c=1}$ are of opposite signs, $\Lambda > 0$ means the slope of the viscosity profile at the point $c=1$ is steeper than at $c=0$. In other words, the slope in unstable zone is steeper than stable zone.

A number of studies depict viscosity profile by Λ and attempt to identify and quantify the stability of fluid. Therefore, Loggia *et al.* [24] make an exhaustive study of the parameter and explains the key for longitudinal dispersion in making conditionally unstable an initially stable profile at a

critical time. Yortsos and Zeybek [47] showed that Eq. (68) with $\Lambda=1$ can be obtained for the monotonic profile. Manickam and Homsy [3] used the QSSA and suggested that when the parameter Λ is positive, the flow is always unstable, and when Λ is negative, the initially stable flow becomes unstable as the base flow diffusion; but they also suggested the equation fail to hold at large times when the base state has diffused out. With nonmonotonic viscosity profile, Kim and Choi [25] showed that Λ is expressed as:

$$\Lambda = \frac{(\gamma_1 - \gamma_0)\mu_m}{\alpha + 1} \left[(1 + a)\cos(\gamma_0) + (1 + a)^{-1}\cos(\gamma_1) \right]. \quad (69)$$

We begin analyzing the favorable ($\alpha=0.7$) and unfavorable ($\alpha=3$) end-point viscosity contrast viscosity profiles set shown in Fig. 17, respectively. Because higher c_m is easy to cause our numerical code become unstable, in order to assess the magnitude of this effect, we carried out a relevant parameter set in which $Pe=400$ and $\mu_m=4$ were kept constant, and fingering was generated by different sets of c_m .

Figure 18 plots the end-point derivatives of the viscosity profile, Λ as a function of the maximum of the viscosity profile, c_m , for the unfavorable (blue curve) and favorable (red curve) end-point viscosity contrast. It presents a simple tendency toward more unstable of fluid for higher c_m , which is consistent with Manickam and Homsy [3]. The time evolution of the interfacial length is illustrated in Fig. 19. A general trend is observed, in which a higher c_m leads to a more unstable interface at the early time, but turns more stable at a later stage. However, concentration images in Fig. 20 illustrated that at the final stage ($t=0.30$), as c_m increase, fingers become more obscure.

It should be noted as the Péclet number decreases closely to the critical number Pe_c demonstrated by Tan and Homsy [1], the approach sketched out here fails to predict the stability of fluid. Fortunately, in that scenario,

the fingering is not mature, and render parameters vary ineffectively. It is acceptable to neglect the error in predicts.

3.2.4 Influence of the end-point viscosity contrast α

Now we turn to the investigation of the role played by the end-point viscosity contrast α . The influence of this parameter is quite intuitive. As a general point, for large end-point viscosity contrasts and Péclet number, strong nonlinear interactions between the finger, such as merging, partial merging, and shielding, are observed [4] with monotonic viscosity profile. Interestingly, investigations of the injection-driven Hele-Shaw cell with nonmonotonic viscosity profiles have been performed so far focusing solely on quarter five-spot configuration and rectilinear flow. Therefore, the beautiful interfacial patterns for radial injection flows involving miscible fluids are still largely unexplored in the present literature.

We begin our numerical investigation performing a systematic study of the concentration images obtained for different values of the relevant control parameters. Basing on the above discussions, we expect large end-point viscosity contrasts leading to a strong nonlinear interaction. However, it is also interesting to notice the fundamental differences regarding the enhanced fingering processes induced by Péclet number Pe and end-point viscosity contrast α . Comparing the concentration images in Fig. 21 and descriptions in more qualitative terms in Fig. 22 highlight differences the two parameters, we found that higher difference between end-point viscosity contrast α and the maximum viscosity μ_m caused richer phenomenology, such as tip splitting was observed in Fig. 21 (a). Look at the interfacial behavior in another way, comparing Fig. 21 (a) with (c), it is interesting to find that lower end-point viscosity contrast α for constant maximum viscosity μ_m leads to enhanced fingering around internal regions.

An important interfacial behavior that can be studied more quantitatively

is the one related to different morphological interfacial features induced by higher Péclet number or higher end-point viscosity contrast α . Compare Fig. 21, and will find that higher Pe leads to more fingering (recheck Fig. 9 also agree this point), while higher α for constant maximum viscosity μ_m leads to longer viscous fingers.

Another scenario is favorable end-point viscosity. The set of simulations we have chosen are with nonmonotonic viscosity profiles for the end-point viscosity contrast $\alpha=0.2, 0.5, \text{ and } 1$, respectively. Other parameters set are fixed at the Péclet number $Pe=400$, the maximum viscosity $\mu_m=4$ and the location of the maximum viscosity $c_m=0.1$. A schematic of these profiles with the parameters set are shown in Fig. 23 and almost overlap between three lines. The concentration and vorticity images (Fig. 24) and the time evolution of the interfacial length (Fig. 25) indicates that there are no statistically interaction effects of favorable end-point contrast was found.

Moreover, recheck Fig. 10, although the end-point viscosity contrast of unfavorable scenario is the inverse of the favorable case, fingering for unfavorable contrast are always longer than favorable one. This phenomenon indicates that unfavorable end-point viscosity contrast leads to fluid more unstable than the favorable one if other parameters set is held fix.

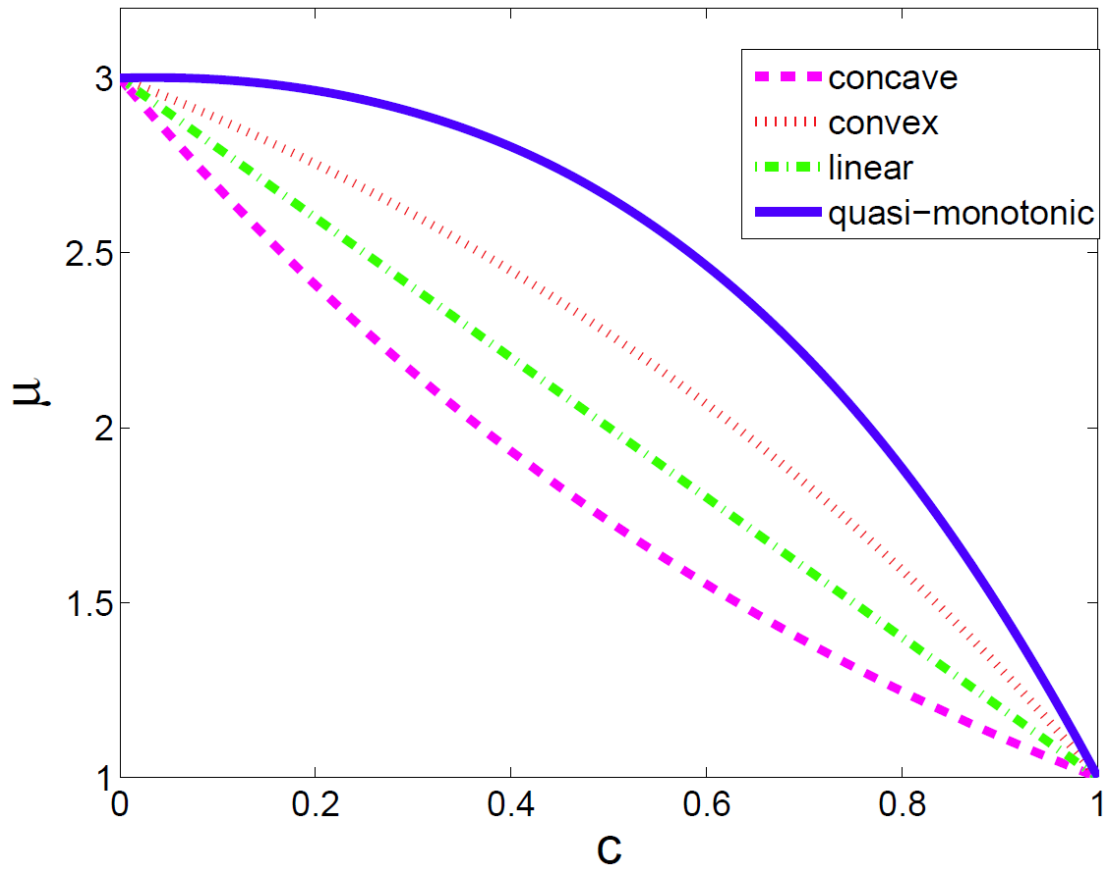


Figure 5: Various types of monotonic viscosity profiles with $A=0.5$ (viscosity ration $\alpha=3$). The quasi-monotonic profile is represented by insignificant non-monotonicity of $\mu_m=3.001$ and $c_m=0.03$.

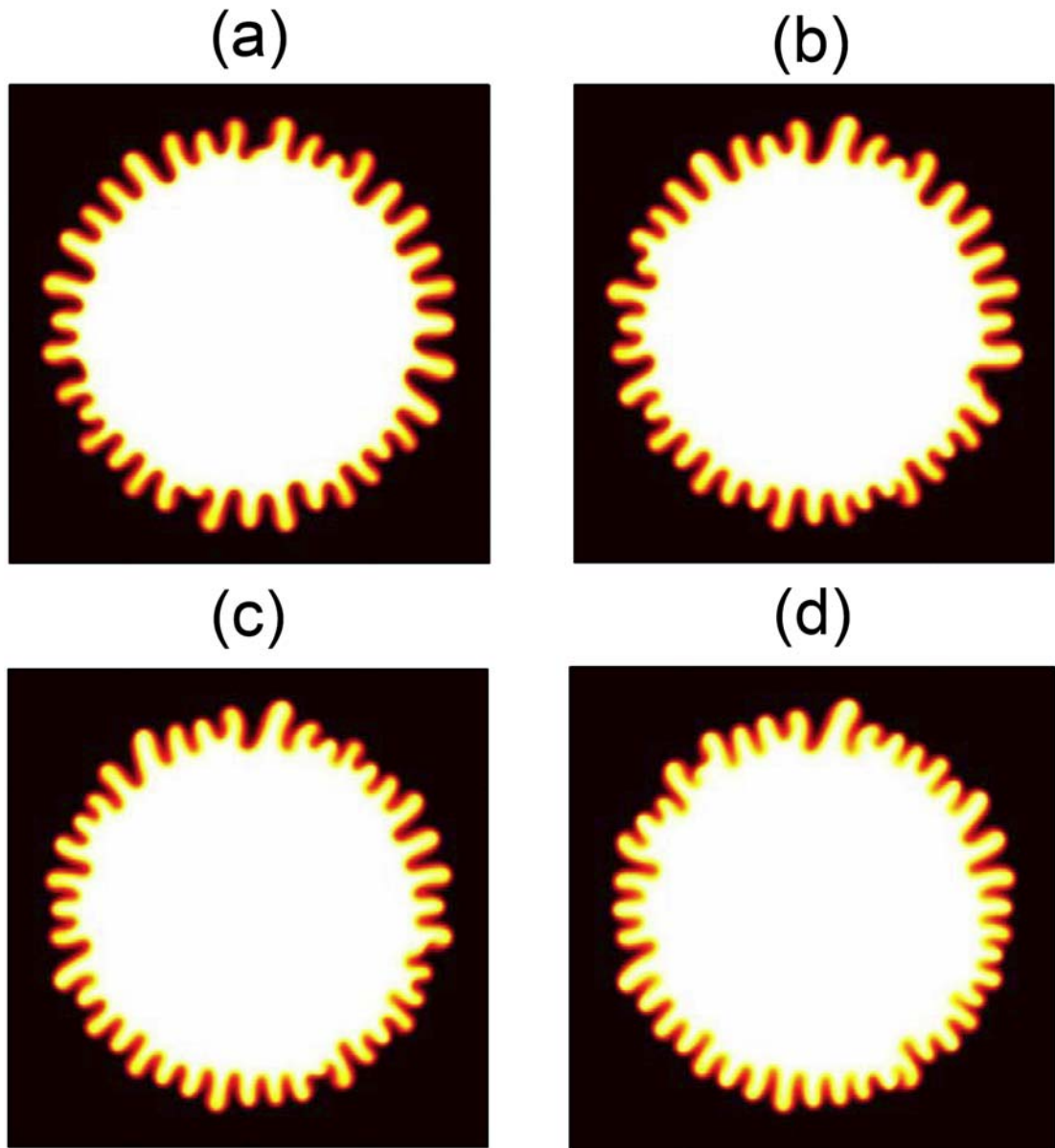


Figure 6: Concentration images with $Pe=800$ at $t=0.30$ for various types of viscosity profiles shown in Fig. 5, (a) concave; (b) linear; (c) convex and (d) quasi-monotonic. In the present unstable conditions, i.e. $\mu_1 > \mu_2$, fingering instabilities are observed for all the profiles. The overall patterns show great similarities, which indicate insignificant influences of the local correlations between fluid concentration and the viscosity.

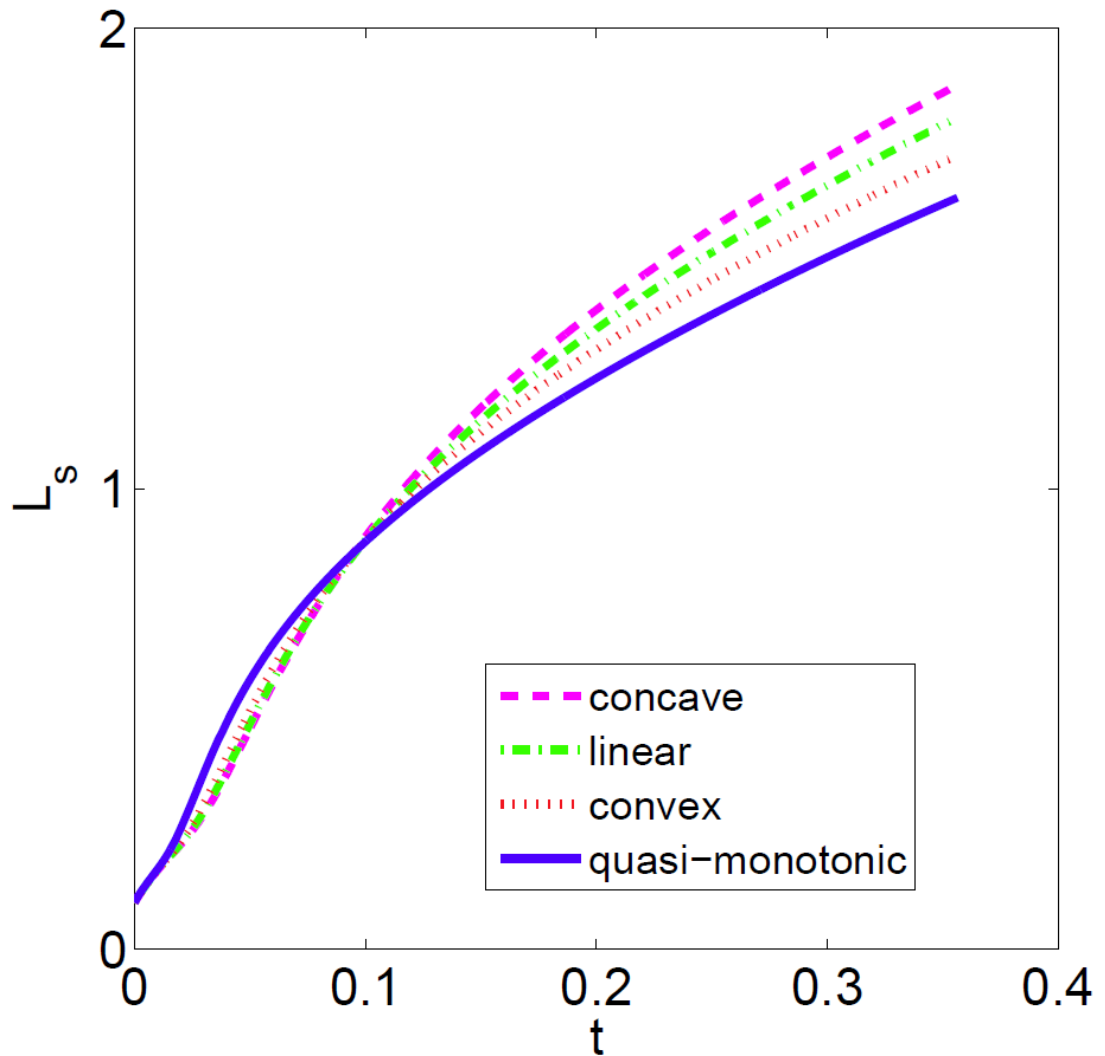


Figure 7: Evolutions of the interfacial lengths, which can be used as a global quantitative measurement of the prominence of fingering, for the four conditions shown in Time evolution of the interfacial length under the condition set as Fig. 5. The global characteristics of interfacial lengths show no significant variations. Nevertheless, a general trend is observed, in which a more convex profile leads to a more unstable interface at the early time, and turns more stable at a later stage.

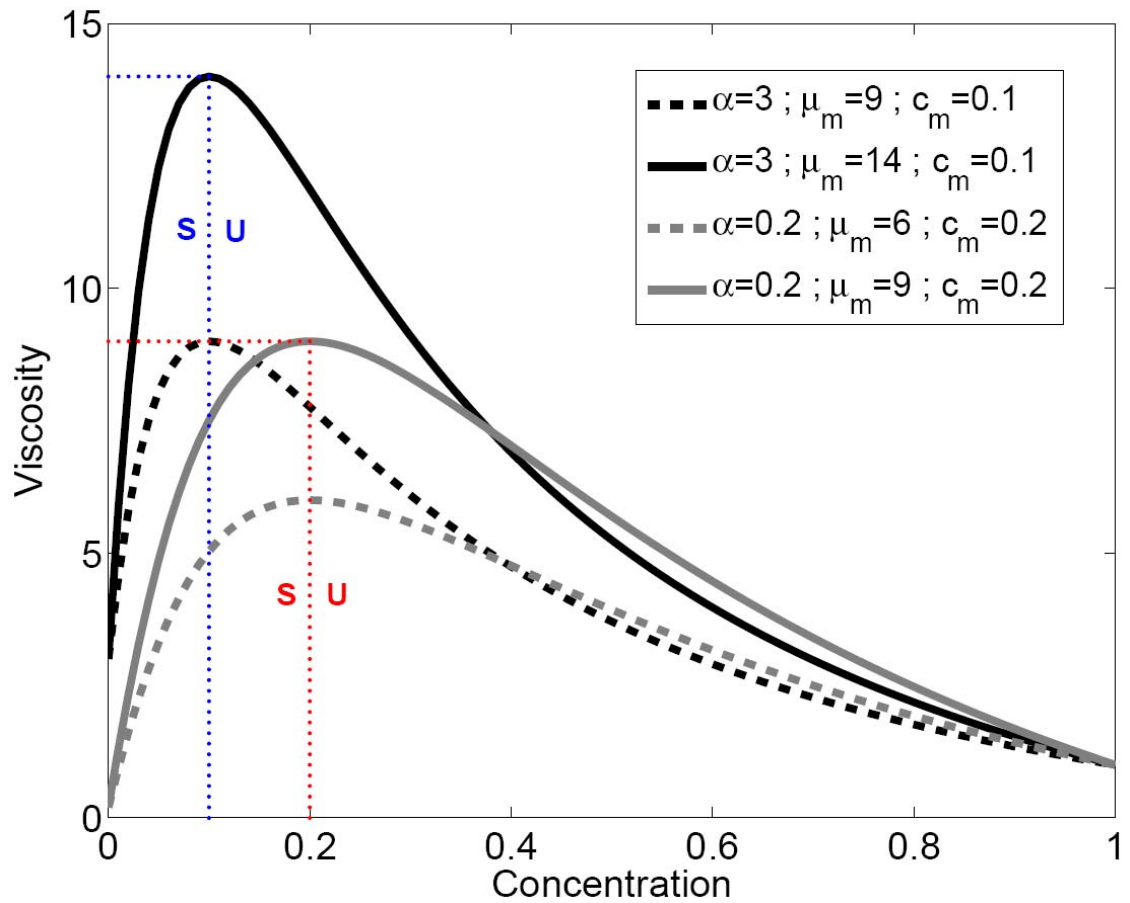


Figure 8: Representative profiles of non-monotonic viscosity. The black lines show unfavorable end-point viscosity contrasts of $\alpha=3$, $c_m=0.1$ for $\mu_m=9$ and 14. Favorable end-point viscosity contrasts are represented by the red lines with $\alpha=0.2$, $c_m=0.2$ for $\mu_m=6$ and 9.

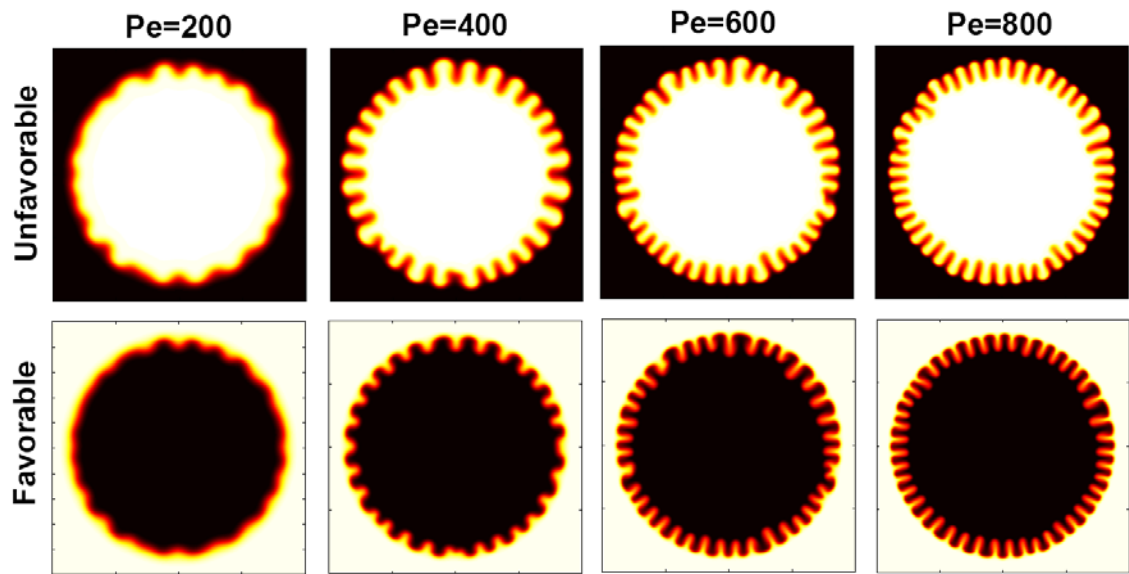
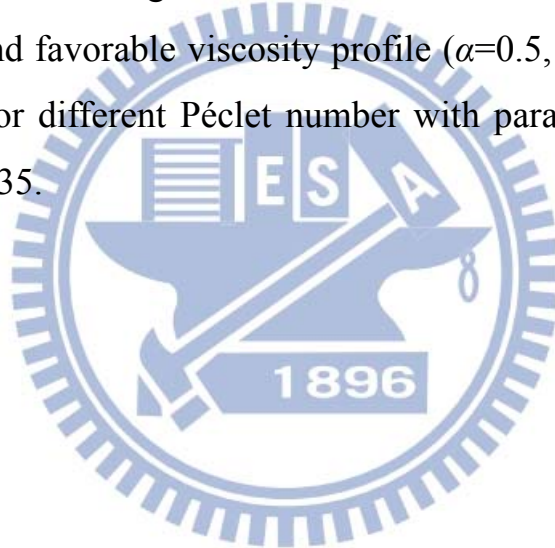


Figure 9: Concentration images for the case of unfavorable viscosity profile ($\alpha=2$, top row), and favorable viscosity profile ($\alpha=0.5$, bottom row). These simulation used for different Péclet number with parameters set for $\mu_m=4$ and $c_m=0.2$ at $t=0.35$.



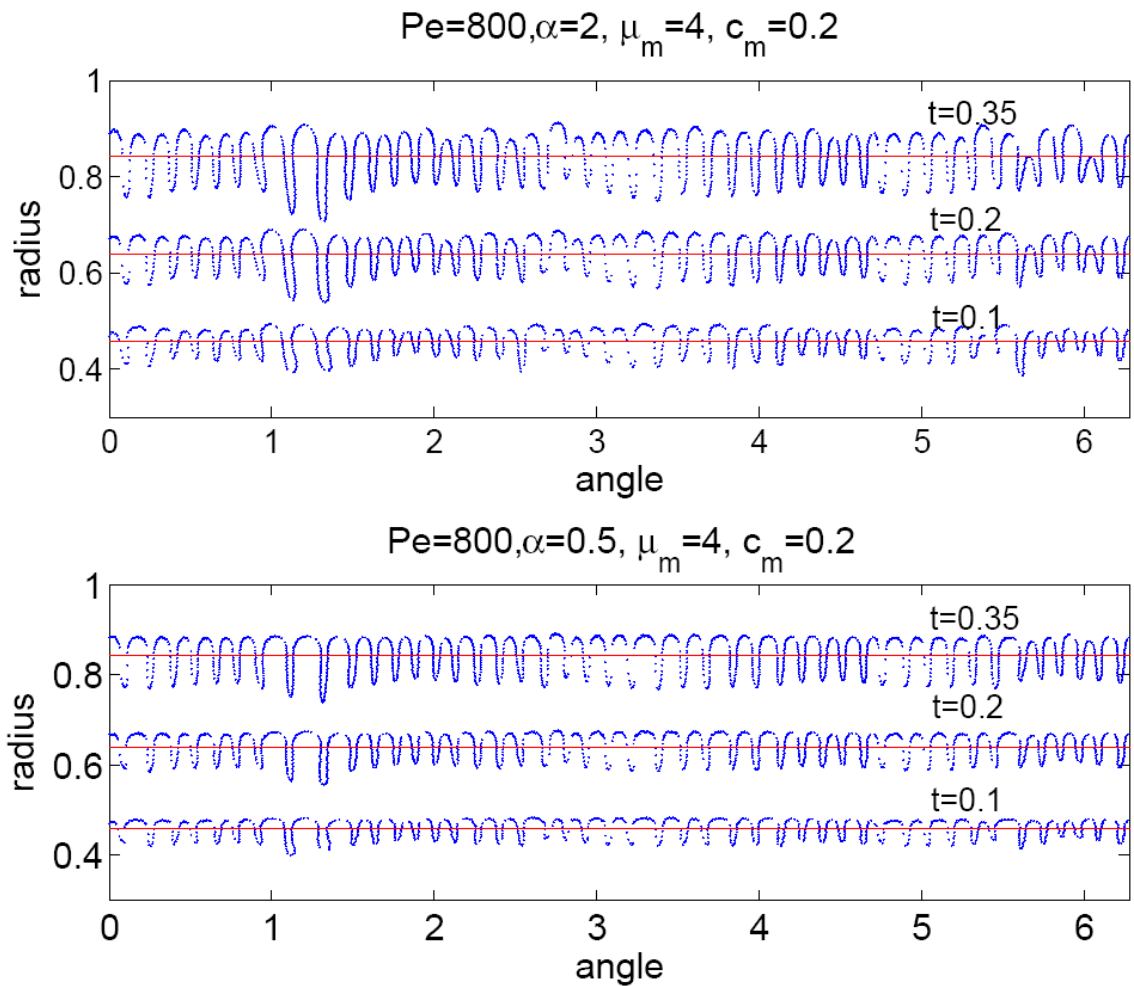


Figure 10: The contour of concentration for $c=0.5$ versus azimuth with the same viscosity profile sets of Fig. 9. Both on unfavorable case ($\alpha=2$, top fig) and favorable end point contrast ($\alpha=0.5$, bottom fig) with $Pe=800$, at $t=0.1$, 0.2 and 0.35 , respectively. The red line indicates the position of base state as a function of the time.

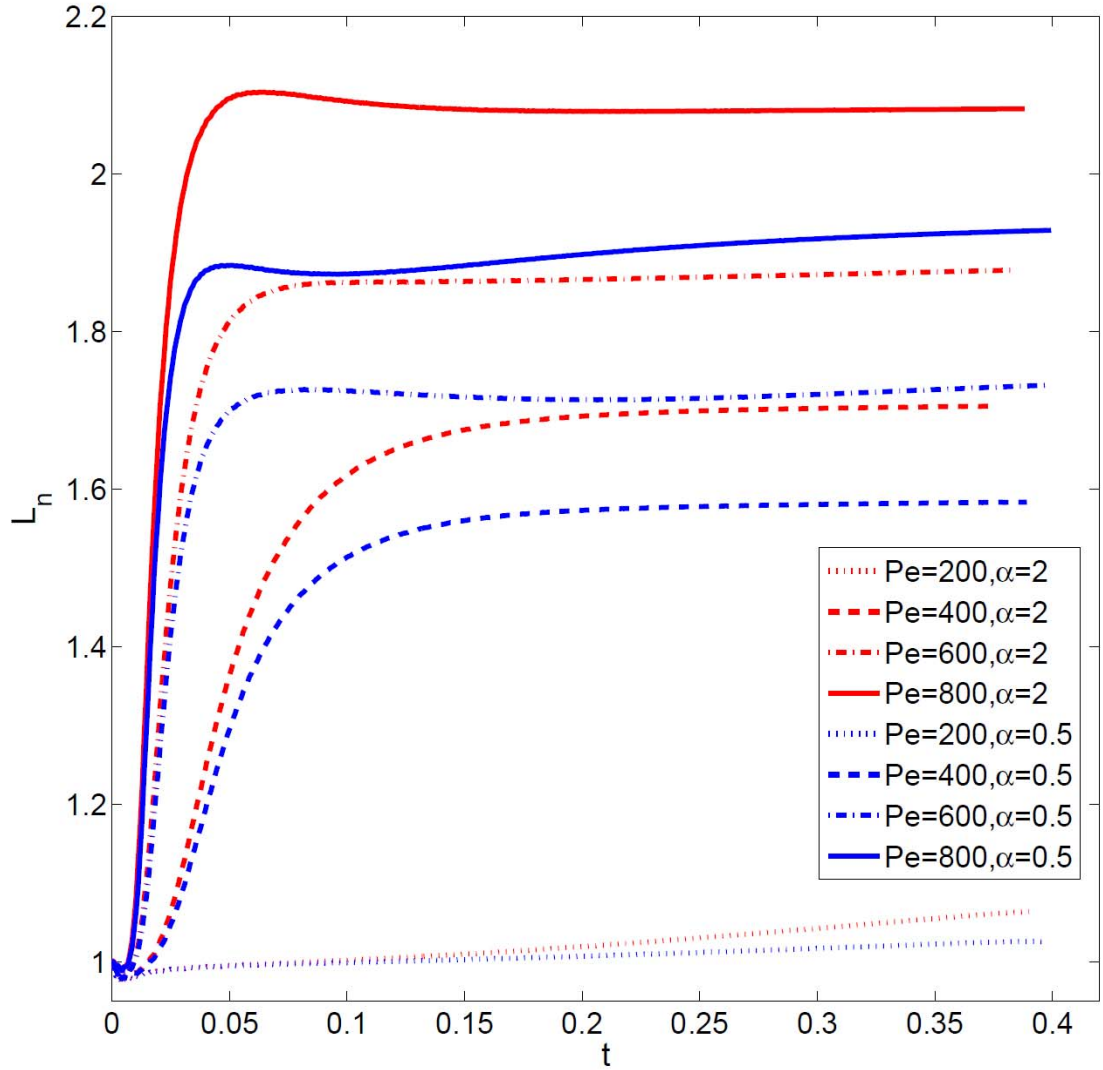


Figure 11: Interfacial length L_n as a function of time for different Péclet number with constant viscosity profile ($\mu_m=4$ and $c_m=0.2$) in unfavorable and favorable viscosity profile. In the inset the number label the Péclet number and end-point viscosity contrast. An interesting phenomena damping effect can be observed in $Pe=800$ and $\alpha=0.5$ set and will be discussed later.

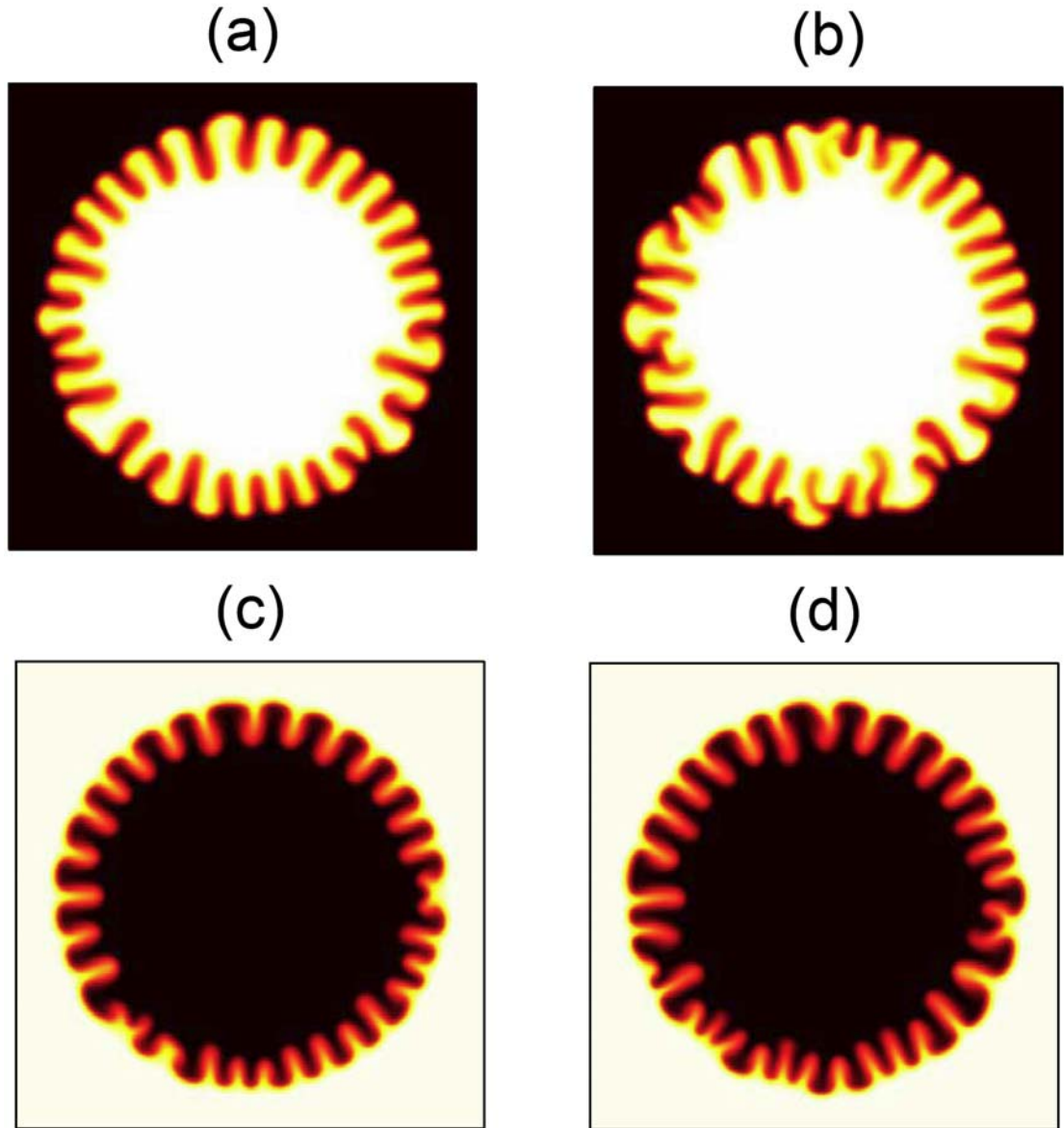


Figure 12: Concentration images for the non-monotonic viscosity profiles shown in Fig. 8 with $Pe=400$. Unfavorable viscosity contrast of $\alpha=3$ and $c_m=0.1$ for $\mu_m=9$ (a) and $\mu_m=14$ (b). Favorable viscosity contrast of $\alpha=0.2$ and $c_m=0.2$ for $\mu_m=6$ (c) and 9 (d). The non-monotonic viscosity profile enhances fingering instability significantly. Even an original stable interface in a monotonic profile appears significantly fingering if the viscosity profile is non-monotonic, i.e. $\alpha < 1$ shown in (c) and (d). In addition, the prominences of fingering are enhanced by degree of the monotony, i.e. higher μ_m .

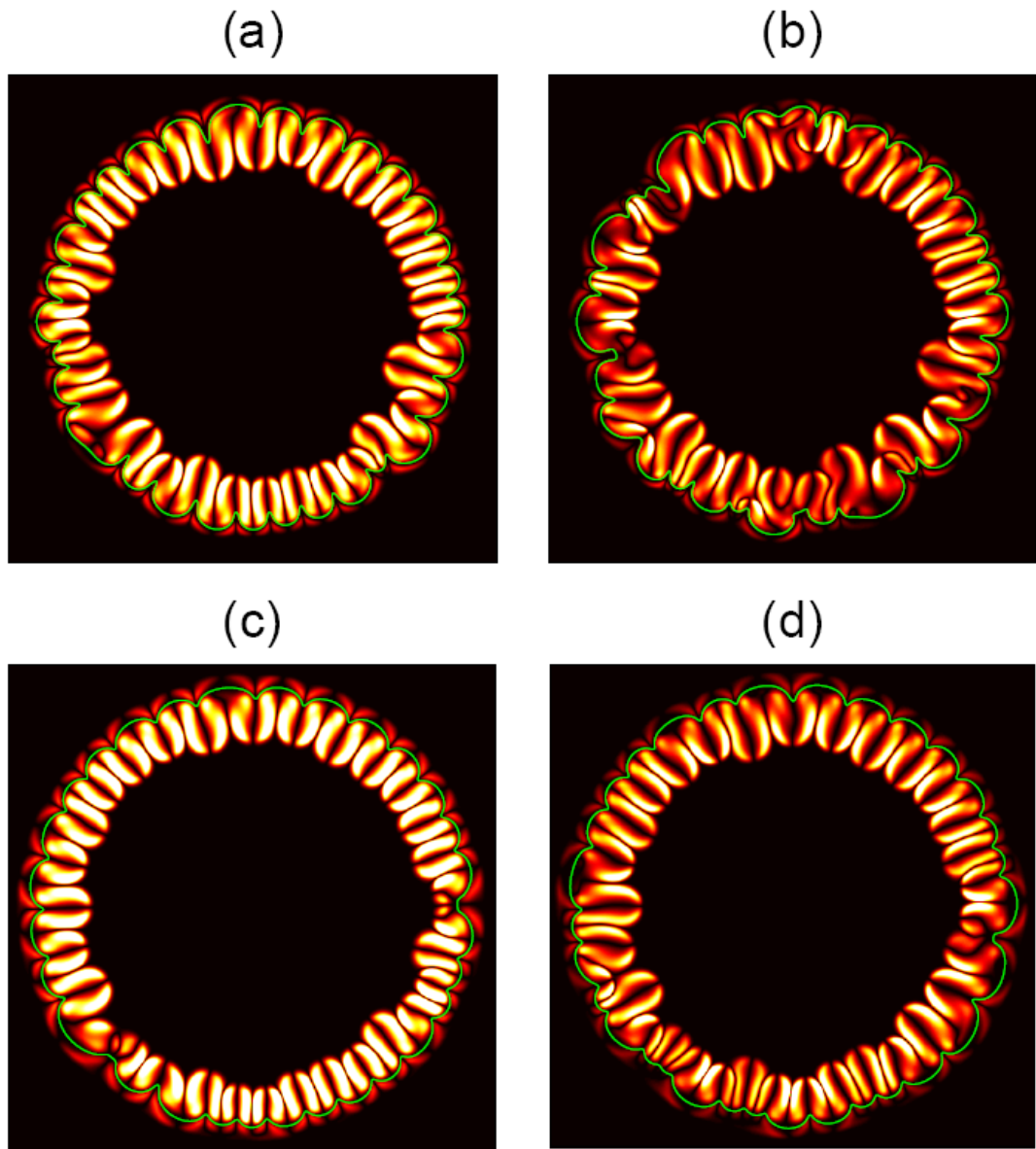


Figure 13: Correspondent images of vorticity for the cases shown in Fig. 8. Besides the well-understood vorticity pairs inside the individual fingers, additional pairs of detached vorticity caps right beyond the fingertips are generated due to the non-monotony of viscosity profile.

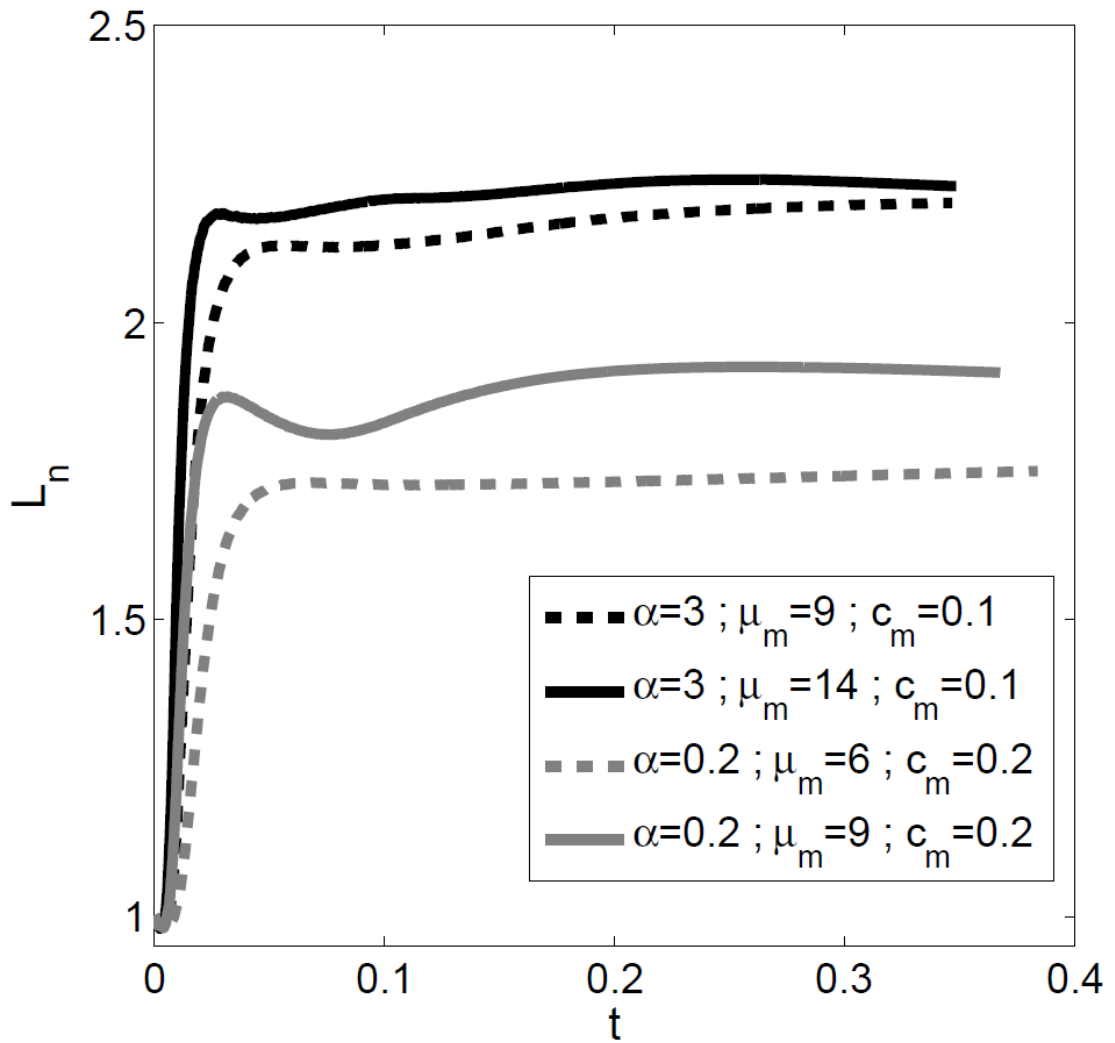


Figure 14: Evolutions of the normalized interfacial lengths for the four cases shown in Fig. 8. After a short period of time with significant growths, the interfacial lengths appear to level off. In line with the common expectations, a more unfavorable end-point viscosity contrast, such as $\alpha=3$, results in a more prominent fingering instability. Also confirmed is that significance of the viscosity non-monotony leads to a more unstable interface, e.g. $\mu_m=9$.

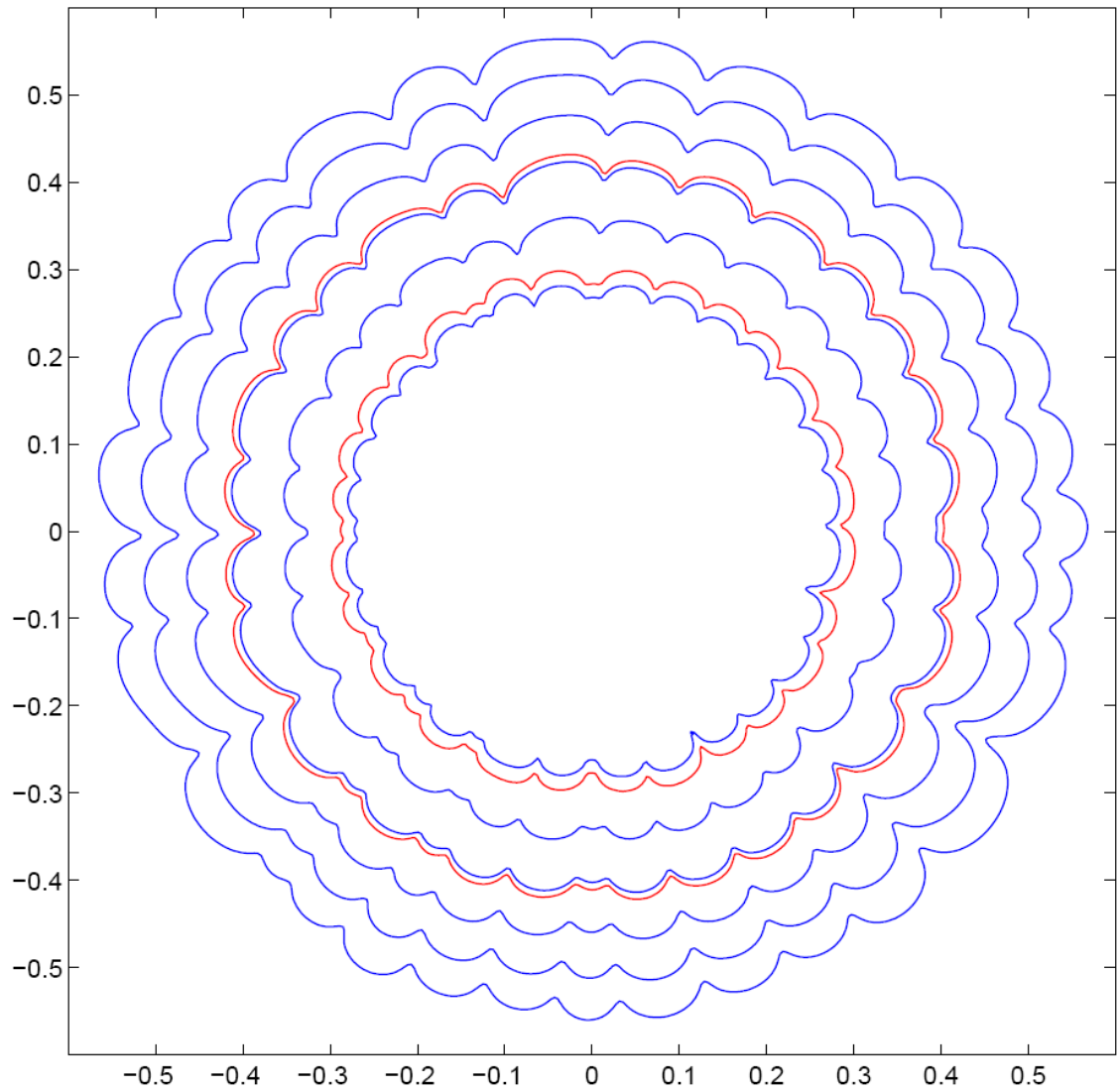


Figure 15: A time series of the contours on the concentration to the Fig. 13 (d) parameters sets as $\mu_m=9$. Time is varied between 0.03 and 0.13 with increments of 0.02 in blue lines. Times during damping effect are plot in red lines.

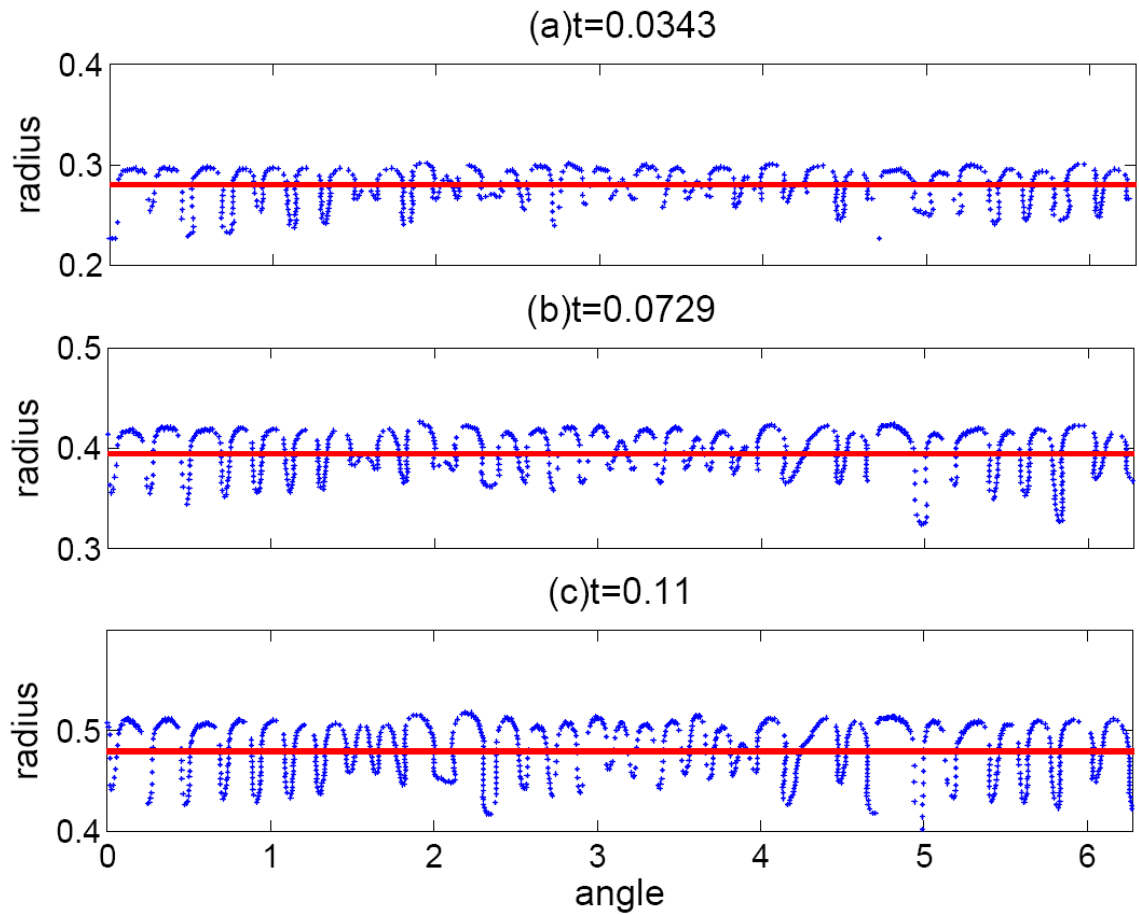


Figure 16: The contour of concentration for to the Fig. 13 (d) parameters sets as $\mu_m=9$ at $t=(a)0.0343$, (b) 0.0729 , and (c) 0.11 . The green lines indicate the position of basestate as a function of the time.

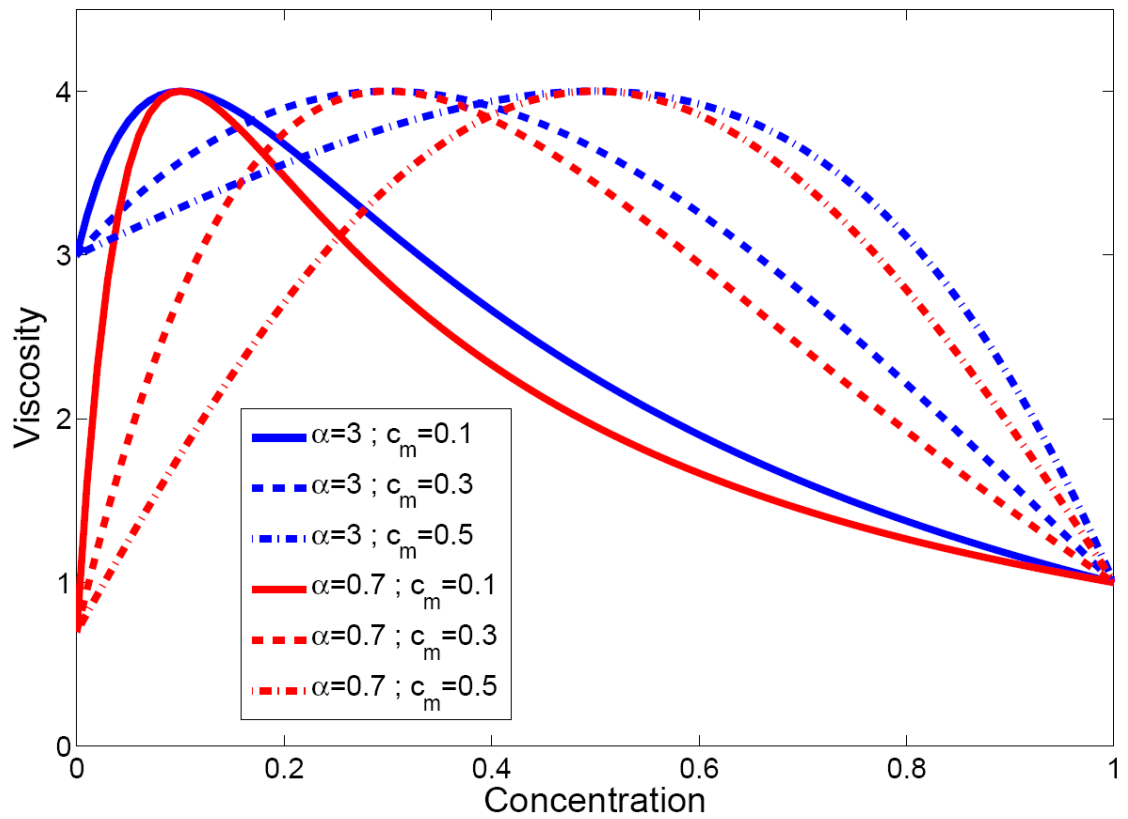


Figure 17: Representative profiles of non-monotonic viscosity for the cases with unfavorable and favorable end-point contrasts of $\alpha=3$ and 0.7 , respectively. The local maximum viscosity contrast is $\mu_m=4$, whose position is at $c_m=0.1, 0.3$, and 0.5 .

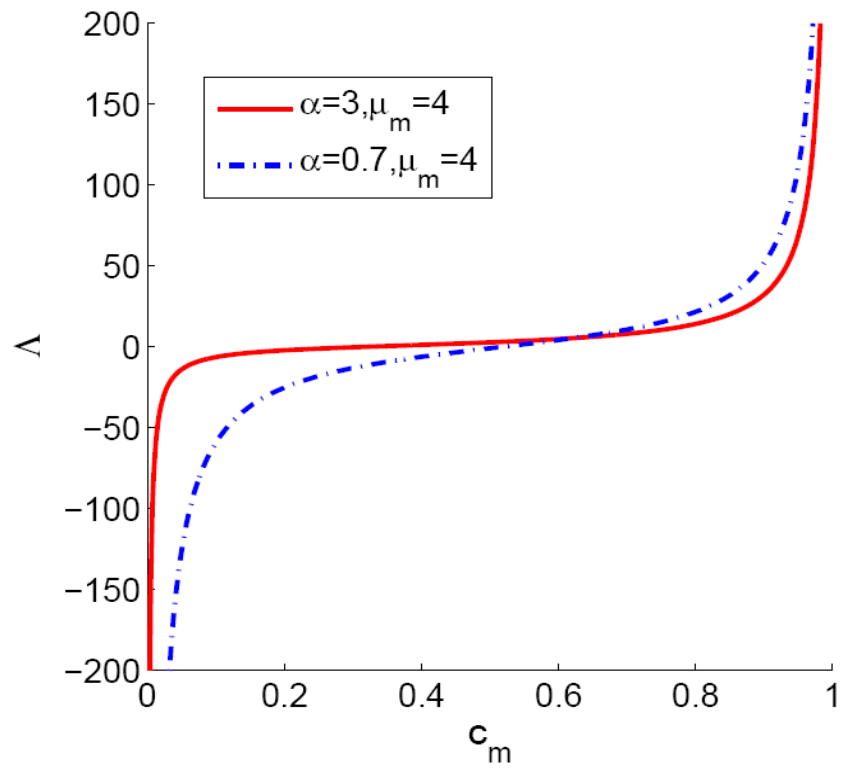


Figure 18: Parameter for the end-point derivatives of the viscosity profile, Δ as a function of the maximum of the viscosity profile, c_m , both for the unfavorable and favorable end-point viscosity contrast in Fig. 17.

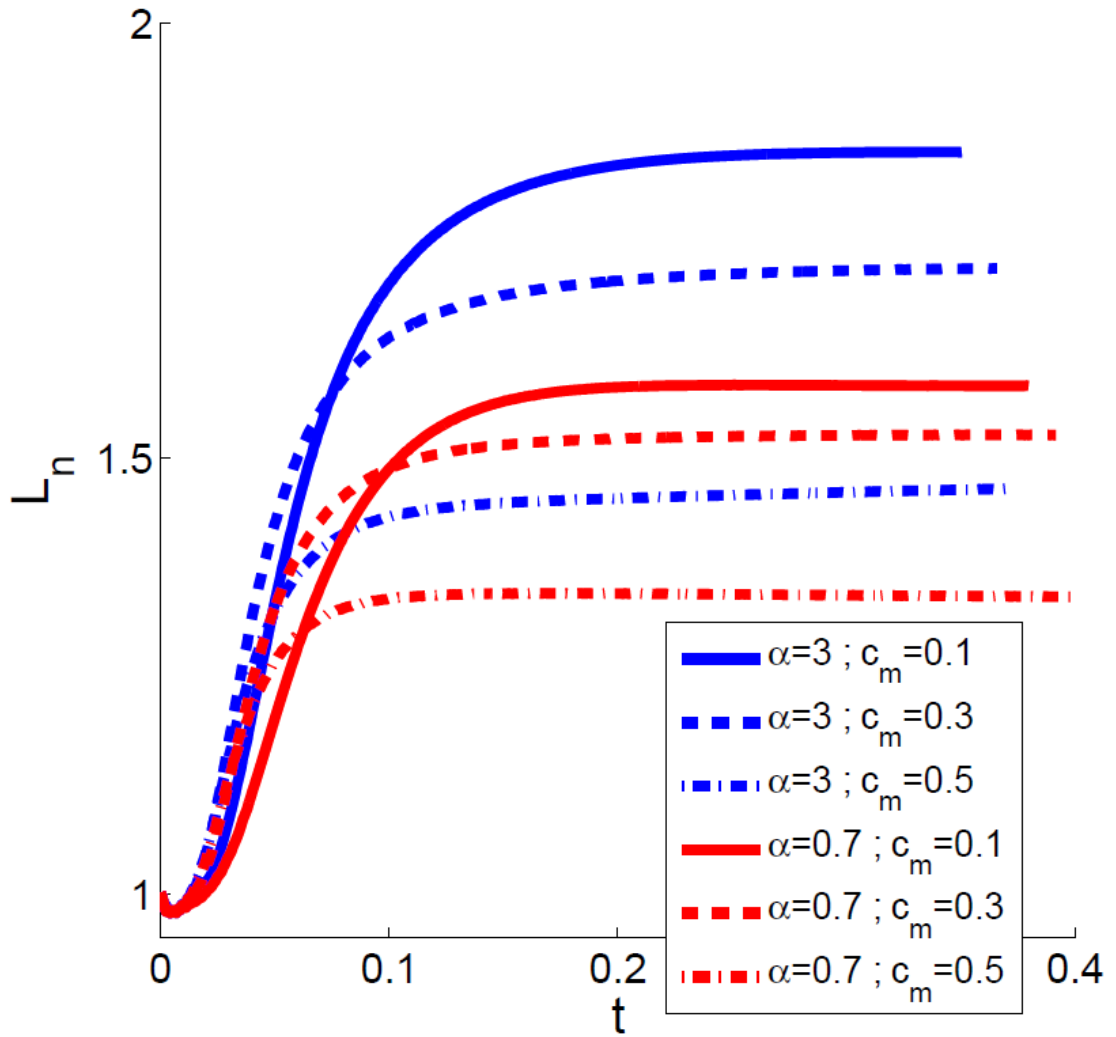


Figure 19: Evolutions of the normalized interfacial lengths for $Pe=400$ with the six viscosity profiles shown in Fig. 17. The most unstable interface at a later time stage is always triggered by a smallest $c_m=0.1$, whose viscosity profile appears more concave, for both unfavorable and favorable end-point conditions. The trend agrees well with the findings presented in Fig. 18.

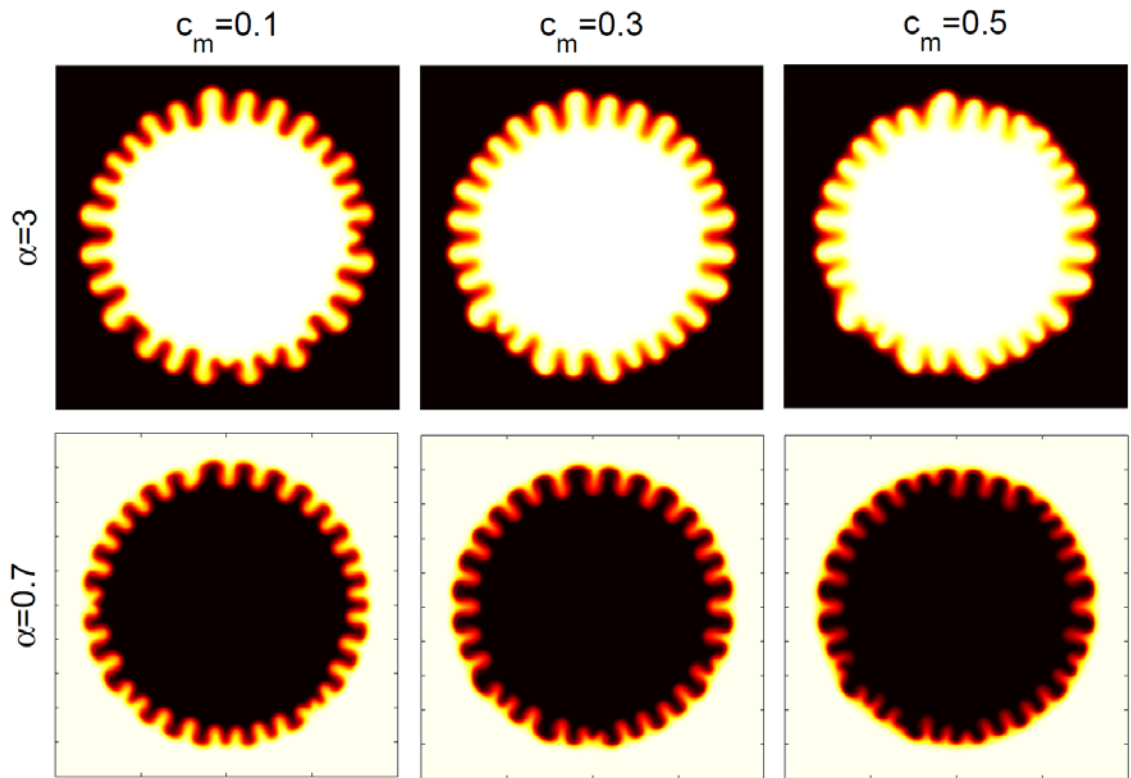


Figure 20: Concentration images for the non-monotonic viscosity profiles shown in Fig. 17 with $Pe=400$ and $\mu_m=4$ at $t=0.30$. Unfavorable viscosity contrast of $\alpha=3$ and $c_m=0.1, 0.3,$ and 0.5 . Favorable viscosity contrast of $\alpha=0.2$ and $c_m=0.1, 0.3,$ and 0.5 . The lower c_m enhances fingering instability significantly. Even an original unstable interface in higher c_m appears significantly more unstable either favorable or unfavorable shown in Fig. 19.

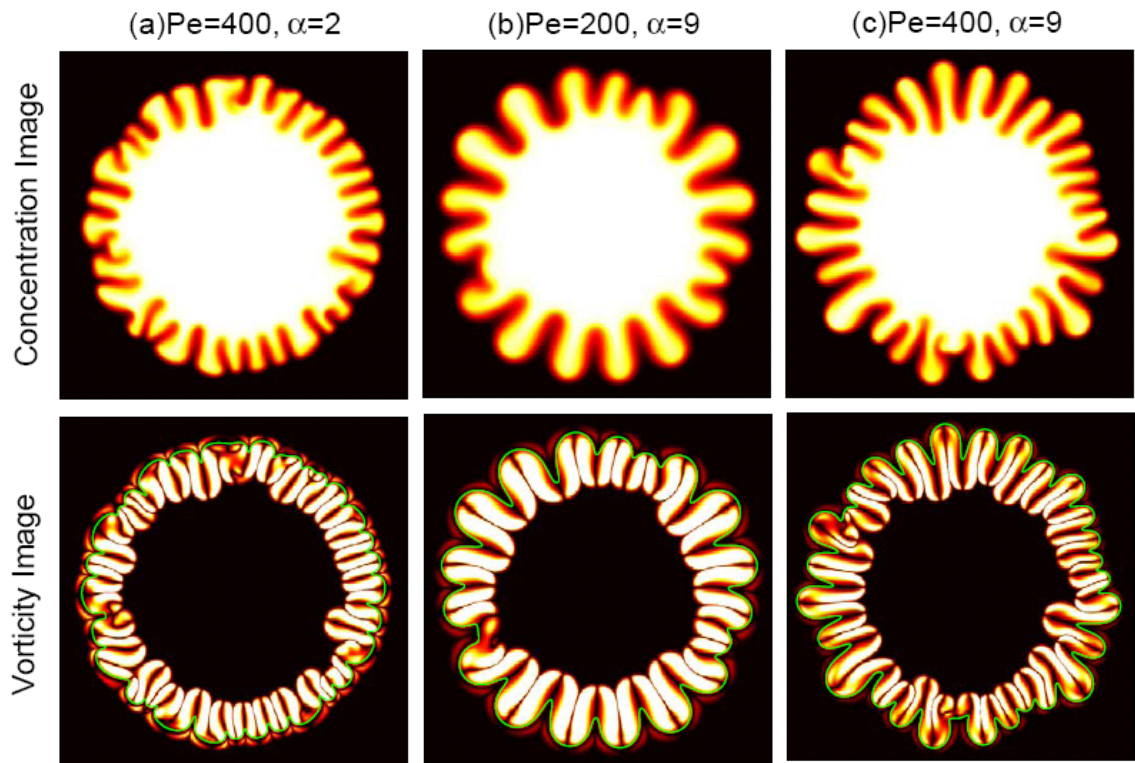


Figure 21: Concentration images (top row) and vorticity images (bottom row) for viscosity profile set with $\mu_m=13$ and $c_m=0.1$ for (a) $Pe=400$ and $\alpha=2$. (b) $Pe=200$ and $\alpha=9$. (c) $Pe=400$ and $\alpha=9$ at $t=0.30$. The outer fluid is more viscous ($\mu_2 > \mu_1$).

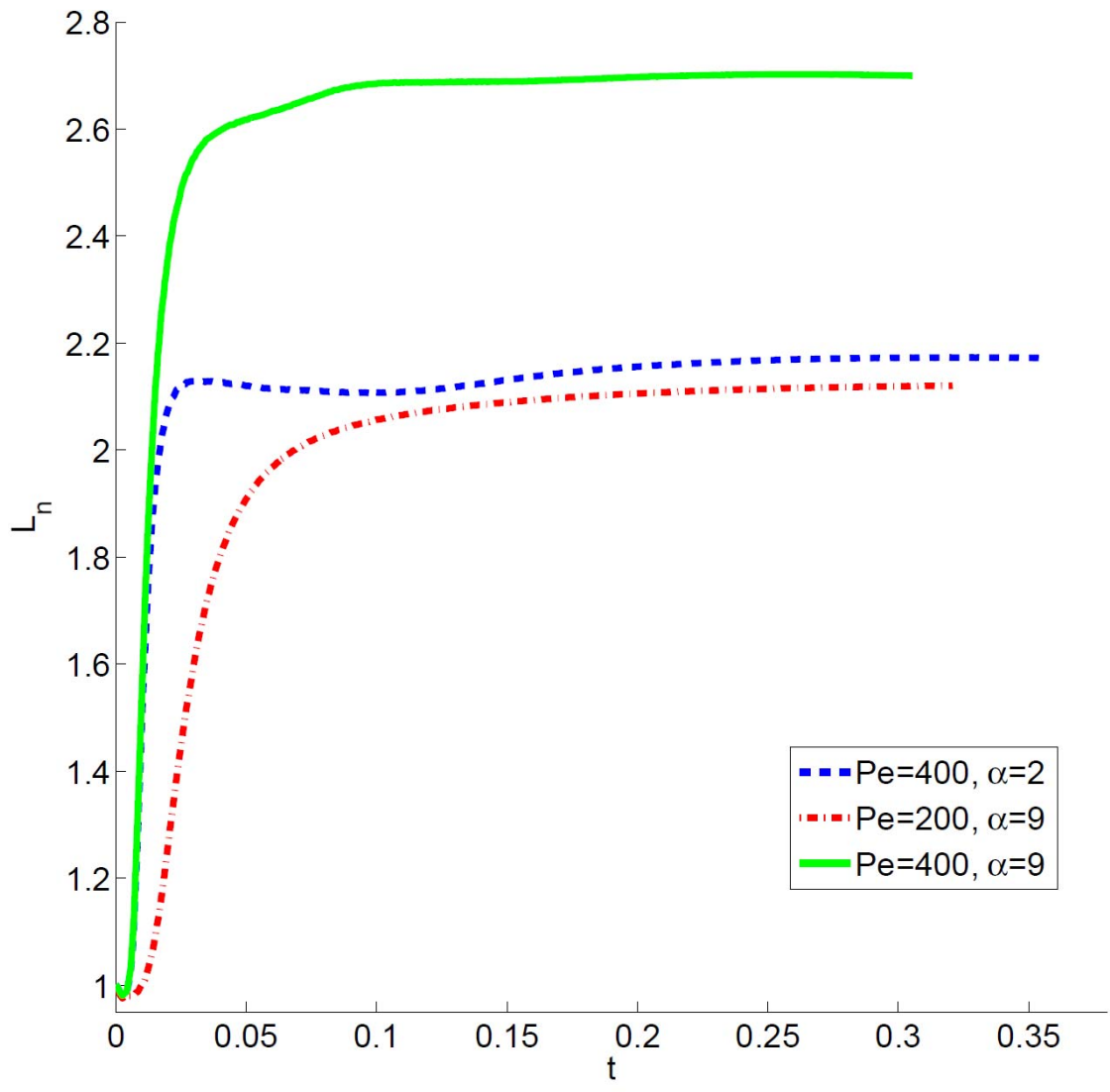


Figure 22: Evolutions of the normalized interfacial lengths for Fig. 21.

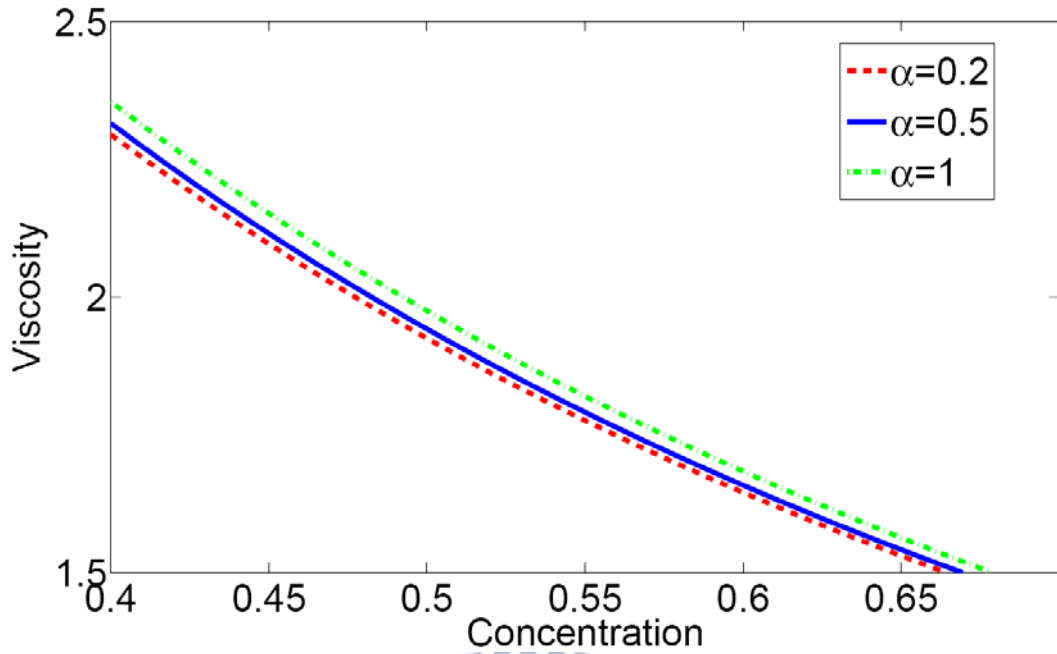


Figure 23: Zoom in the nonmonotonic viscosity profiles for $\mu_m=4$, $c_m=0.1$, and $\alpha=0.2, 0.5$, and 1.

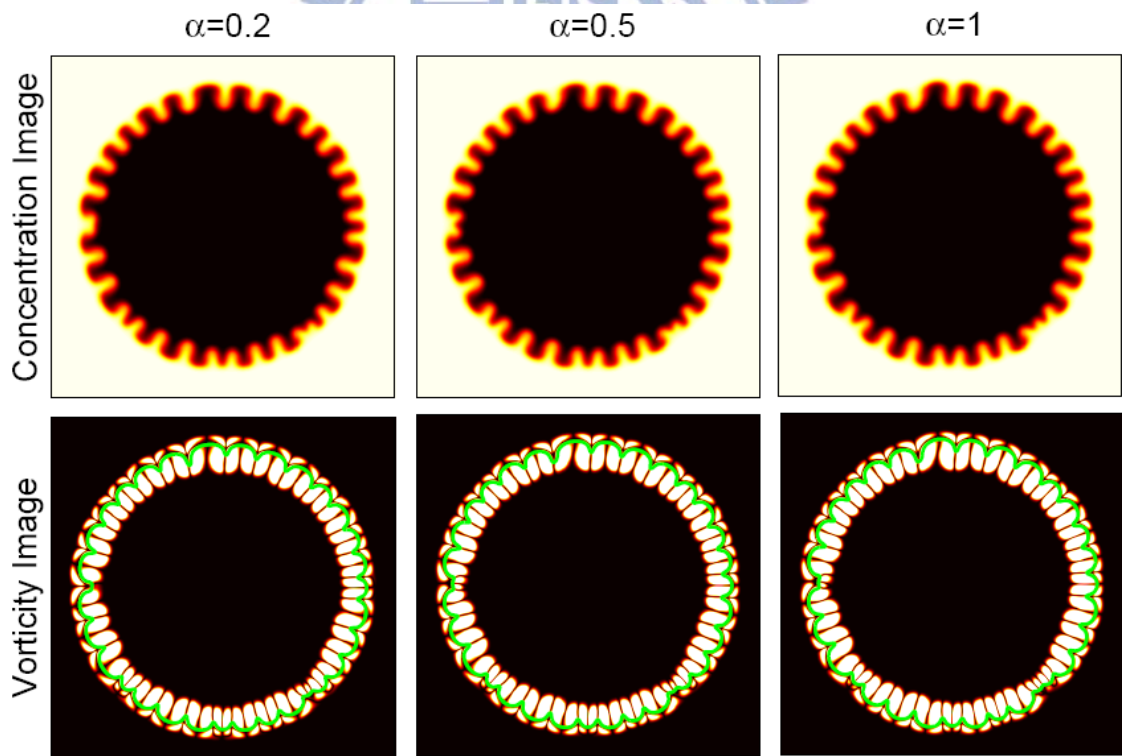


Figure 24: Concentration images (top row) and vorticity images (bottom row) for $Pe=400$, $\mu_m=4$, $c_m=0.1$, $\alpha=0.2, 0.5$, and 1 at $t=0.30$. The inner fluid is more viscous ($\mu_1 > \mu_2$) and the green lines in vorticity images indicate the position of μ_m .

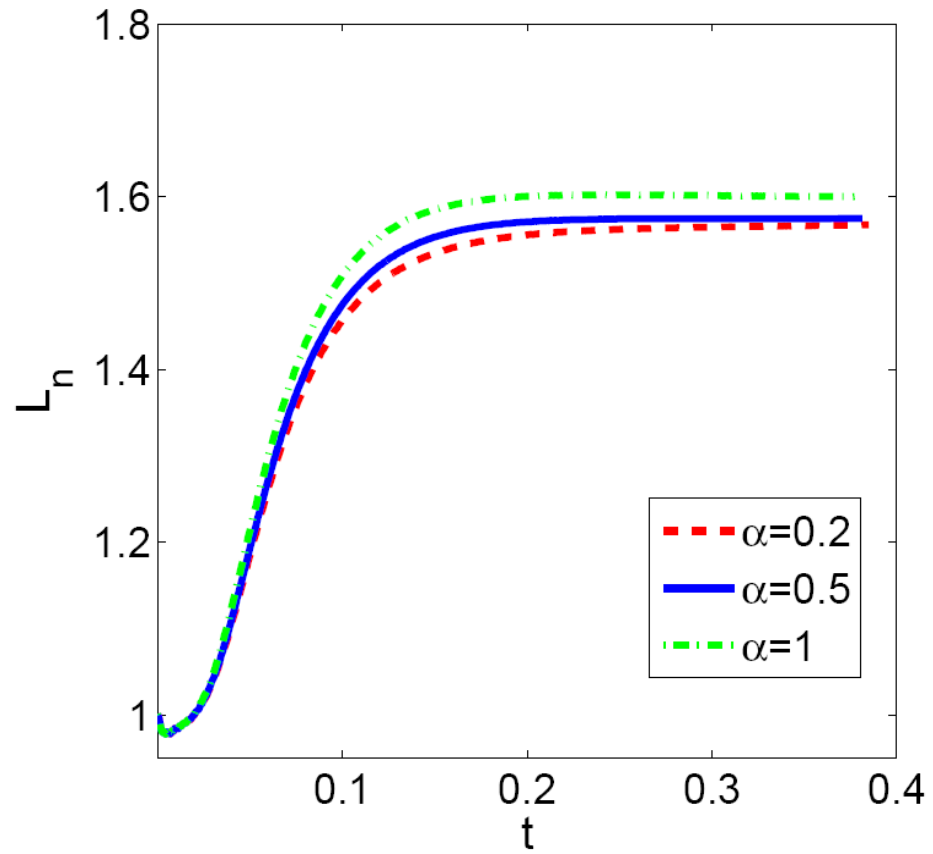


Figure 25: Time evolution of the interfacial length with $\mu_m=4$, $c_m=0.1$, $\alpha=0.2$, 0.5 , and 1 for $Pe=400$. In the inset the detail viscosity profiles for the three parameters sets. No significant main effect for favorable end-point contrast was found.

Chapter 4 Controlling Radial Fingering Patterns in Miscible Lifting Hele-Shaw Flow

We begin our numerical investigating the effectiveness of adjusting the time-dependent gap width and perturbation for these complex fingered structures, then performing a systematic study of the concentration images obtained for different viscosity profiles. The layout of the rest of this chapter is as follows. Section 4.1 focuses on comparing the fingering in conventional linear or exponential time dependencies. In Section 4.2, we analyze how the perturbation can influence the ultimate appearance of the fluid-fluid diffusive interface. As pointed out in Chapter 3, Section 4.3 discusses the influence of four kinds of viscosity profiles on the interface dynamics: concave, linear, and convex monotonic viscosity profiles, and nonmonotonic viscosity profile are compared. Various parameters, such as the overall viscosity contrast of both monotonic and nonmonotonic viscosity profile, and local maximum viscosity contrast and position of local maximum viscosity for nonmonotonic viscosity profile, are also analyzed systematically in Section 4.4.

4.1 Influence of the Lifting Scenarios

Here we turn to the numerical results of comparing the resulting patterns with variant lifting. Compare the fingering patterns under the same dimensional lifting effectiveness, i.e., we contrast the situations in which the patterns for exponential and variant lifting have reached an equal gap width at equal times: $h_{exp} = h_v = h$. In the following simulations, we consider characteristic values for the lifting Péclet number $Pe=3000$, and viscosity contrast $A=0.925$. In addition, we take the lifting ratio $a=\delta/\gamma=1/3$. In order

to ensure the appropriateness of the Hele-Shaw approach [6], only situations of relatively small gap spacing, namely $h=2h_0$, $3h_0$ and $4h_0$ are considered.

Figure 26 illustrates the concentration images obtained for increasingly larger values of the dimensionless gap width $h/h_0=2, 3$, and 4 , both for the exponential (top row) and variant (bottom row) lifting cases. This is done for a given set initial random perturbations (perturbation set 1). During exponential lifting with $h/h_0=2$, we see the development of a large number of small fingers of the less viscous fluid penetrating the more viscous one. At $h/h_0=3$, fingering is considerably stronger where invading inward moving fingers compete more intensively giving rise to a deformed diffusive interface. Finally, for the dimensionless gap distances $h/h_0=4$, the patterns are even more ramified, revealing plenty of finger competition (length variability) among less viscous fingers, resulting in convoluted structures presenting forms which resemble forks and tridents.

On the other hand, variant lifting reveals a quite different set of morphologies. When $h/h_0=2$, the boundary of the droplet is nearly circular, so that fingers are absent. Very mild fingering formation is then observed for $h/h_0=3$. Finally, if $h/h_0=4$ fingers emerge (about 40 or so) but in a more orderly fashion, finger competition among inward moving fingers is substantially suppressed. This points to the stabilizing nature of the variant lifting process.

Concerning the specific role of Pe and A , we have performed simulations for several other values of the Péclet number in the interval $2000 \leq Pe \leq 4000$ for several other values of the viscous contrast in the interval $0.762 \leq A \leq 0.925$ in Fig. 27. The results identify the very similar stabilizing behavior. Despite of this variation in the values of Pe , we found a relatively small modification in the number of resulting fingers: for example, when $h/h_0=4$, the number of fingers changes only from 38 to 42. This supports

the suitability of the controlling mechanism provided by the variant lifting in spite of sizable modifications in the Péclet number.

Examine the response of the patterns to modifications in the viscous contrast. It can be observed as $A=0.762$, even the $Pe=4000$, the boundary of the droplet is nearly circular, so that fingers are absent. Figure 28 illustrates that the behavior of the dimensionless interfacial length L in terms of h/h_0 for three different Péclet number and Atwood number sets. For the situations involving no significant fingering, i.e., $A=0.762$ (solid curves), the interfacial lengths behave quite similarly to the base state during the whole lifting process, presenting a nearly exponential decay, decrease as time progresses, and always locate far below the other ones. Represent the strong stabilization role of the small viscosity contrast.

A dimensionless gap distances h/h_0 series of the contours on the concentration to the parameters set $Pe=3000$, $A=0.925$ for the exponential lifting case are illustrated in Fig. 29. As shown in Fig. 28, there are two critical points at $h/h_0=1.5$, 2.7. Choose $h/h_0=1.5$, 2, 2.5, and 4 for analysis. At $h/h_0=1.5$, the boundary of the droplet is nearly circular, and the fingers are absent. For later times, the length of the fingers becomes longer. It is worthwhile to note during $h/h_0=2.5$ and 4. Although the length of fingers continues increase, some fingers merge and the number of fingers decrease. The behaviors of the dimensionless interfacial length L in terms of h/h_0 also decrease during this period.

By contrasting these normalized interfacial lengths to the parameters set as Fig. 29, the variant lifting situations are illustrated in Fig. 30. Choose $h/h_0=2$, 3, and 4 for analysis. Like the exponential lifting case, before $h/h_0=3$, the boundary of the droplet is nearly circular, and the fingers are absent. However, for later times, the length of the fingers becomes longer. Without fingers merge, the dimensionless interfacial length L_s in terms of h/h_0 increases (shown in Fig. 32 and to be discussed later). Figure 29 and 30

highlights differences between the two strategies of time-dependent gap width control the complex finger structure.

4.2 Influence of the Perturbation Set

We examine the response of the patterns to modifications in the initial conditions. This issue is addressed in Fig. 31 which depicts patterns at $h/h_0=4$ for both types of lifting, and two additional collections of initial conditions: perturbation set 2 (first column) and perturbation set 3 (second column). The perturbation sets are produced stochastic by Matlab. It is clear that the structures obtained in Fig. 31 are not far different from those obtained in Fig. 26. However, it is worth pointing out that under variant lifting the final number of fingers does not practically change (it varies only from 41 to 43) if initial conditions are altered. A more quantitative account about this result is shown in Fig. 32 which describes the behavior of the dimensionless interfacial length L_s in terms of h/h_0 for exponential lifting EL (solid curves) and variant lifting VL (dashed curves). This is done for the three sets of initial perturbations considered in Fig. 26 and Fig. 31. Note the collapse of the dashed curves, a fact that reinforces the indifference of the variant lifting protocol with regards to changes in initial conditions. The strong stabilization role of the variant lifting is also evident (dashed curves located far below the solid ones).

To detail the effect of perturbation, we choose the most unstable situation in Fig. 32 for exponential lifting case. Figure 33 illustrates the concentration images obtained for increasing larger values of the amplitude of initial random perturbation 5 and 10 times. It is clear that the structures obtained in Fig. 33 are not far different from those in Fig. 26 for h/h_0 series. Although the number of fingers does not practically change, only the length of finger increases with increasing amplitude of perturbation.

4.3 Monotonic Viscosity Profile

As discussed in Chapter 3, the effect for four kinds of viscosity profiles on the interface dynamics: vary-monotonic (including concave, linear and convex) and nonmonotonic viscosity profiles are studied in this section. To address this issue, four kinds of viscosity profiles are depicted in Fig. 35. Because we have proved that exponential lifting situation leads to the fluid more unstable than variant lifting case, we only discuss exponential lifting situation after this section. To ensure the effect of different viscosity profiles, the quasi-nonmonotonic viscosity profile is not across the aforementioned three monotonic viscosity profiles and decreases the impact of the μ_m , set μ_m equal to $\alpha+0.1$, and set c_m at 0.1.

We begin our numerical investigation performing a systematic study of the concentration images obtained from different viscosity profiles. Figure 36 depicts the sequential images of the concentration obtained for increasing larger values of the dimensionless gap width $h/h_0=2, 3$, and 4, for four viscosity profile cases in Fig. 35 with the relevant control parameters $Pe=2000$ and $A=0.925$, which the cell's gap width grows exponentially. During the process of lifting with $h/h_0=2$, with only monotonic (concave) viscosity profile, the development of the largest number of small fingers of the less viscosity fluid penetrates the more viscosity one. The boundary of the droplet with other types of viscosity profiles is nearly circular, so that fingers are absent. At $h/h_0=3$, fingering is considerably stronger where invading inward moving fingers compete more intensively giving rise to a deformed diffusive interface. Very mild fingering formations are then observed for other types of viscosity profile cases. Finally, for $h/h_0=4$, we only observe fingers emerge with linear viscosity profile, but in a more orderly fashion than concave viscosity profile. For convex and quasi-monotonic viscosity profile cases, only smoother shrinking interface which remains nearly circular can be

observed.

A more quantitative account about this result is shown in Fig. 37 which describes the behavior of the dimensionless interfacial length L_s in terms of h/h_0 for exponential lifting. This is done for the four viscosity profiles illustrated in Fig. 35. Figure 37 gives correct trends regarding the stabilizing effects for different viscosity profiles, and most importantly, provides a quantitative verification of the interesting droplet recircularization phenomenon as discussed previously, based on the concept of interfacial lengths L_s . As the case of concave viscosity profile, initially L_s decreases at first, then increases sharply than other profiles. Linear viscosity profile is the second increasing case, and shorter interfacial length is observed. Convex viscosity profile is more stable than linear one. For the quasi-monotonic situation does not involve significant fingering, the interfacial length behave quite similarly to the base state during the whole lifting process.

Moreover, similar to what we have done for injection flow, we examine the response of the pattern to modifications at higher Pe as 4000 and lower A as 0.85. Choose an appropriate c_m to let the quasi-monotonic viscosity profile to cross the convex one, and add a new nonmonotonic viscosity profile to compare the effect of different viscosity profile. All of the five viscosity profiles are illustrates in Fig. 38. Figure 39 plots the dimensionless interfacial length L_s as a function of the dimensionless gap distance h/h_0 for monotonic (dashed curves) and nonmonotonic (solid curve) viscosity profiles. That is just as what we expected that the concave viscosity profile create the most unstable flow between the three monotonic ones, however, nonmonotonic cases demonstrated uncharacteristic behavior. We chose four concentration images of the five cases are illustrated in Fig. 40. Concave viscosity profile is the most unstable case of monotonic scenario, but nonmonotonic viscosity profile reveals more vigorous

fingering than concave case. The unstable response of nonmonotonic viscosity profiles attracted our notice and will be further discussed later.

4.4 Nonmonotonic viscosity profile

Investigating the stability of nonmonotonic viscosity profiles in lifting flow, the influence of the parameter Pe is quite intuitive as expected that demonstrate more vigorous fingering. Moreover, the influence of μ_m , α , and c_m need further discussed.

4.4.1 Influence of the maximum viscosity μ_m

In order to elucidate the influence of the maximum viscosity μ_m on the global and local features of the displacement process, we carried out a series of simulations for which Pe , c_m , and α were held fixed at the values of 3000, 0.1, and 3, respectively. In addition, the same random realization of the permeability field was employed in all simulations. The fingering instabilities at maximum viscosity μ_m , which provide stronger concentration gradient in the unstable zone of viscosity profile, are mostly produced by the inward motion of the less viscous fingers penetrating the more viscous fluid. In this section, by comparing displacements at μ_m are varied between 8 and 32 with increments of 8.

Figure 41 demonstrates the concentration field at much later time $h/h_0=4$. This motion occurs in such a way that the relative lengths of the less viscous fingers longer, making the interface in their tips is much more ramified, presenting outgoing fingers which develop a peculiar forklike or trident like shape. But define an approximately circular internal region in the more viscous. Compare with the result shown in Fig. 12 in injection flow, higher maximum viscosity μ_m leads to not only longer finger length, but more vigorous fingering in lifting flow. Indicate that higher maximum viscosity μ_m plays different role in lifting flow and injection flow. Figure 42

describes the behavior of the dimensionless interfacial length L_s in term of h/h_0 for four maximum viscosity μ_m . As expect, longer interfacial lengths are mainly observed for larger μ_m .

4.4.2 Influence of the end-point viscosity contrast α

Now we turn to the investigation of the role played by the end-point viscosity contrast α with nonmonotonic viscosity profile and monotonic one with equal end-point viscosity contrast ($\alpha_{mono}=\mu_m$). Figure 43 describes the behavior of the dimensionless interfacial length L_s in term of h/h_0 for four sets of nonmonotonic viscosity profiles with constant $\mu_m=16.44$ and two sets of monotonic ones, one is with end-point contrast $\alpha_{mono}=\mu_m=16.44$, another is with higher $\alpha_{mono}=20.08$. For the sake of providing a visual picture of the distinction, dash lines present the result of monotonic viscosity profile cases, and solid lines show the result of nonmonotonic ones. Three points are worth making about this figure. First, we noticed that solid curves stand above the dashed one as α_{mono} equal to μ_m , indicating more fingering and interfacial irregularities for the cases of nonmonotonic viscosity profile than monotonic one while μ_m of nonmonotonic cases is equal to α_{mono} of the monotonic one. Second, as expected, as the monotonic one with higher α_{mono} than μ_m of nonmonotonic scenarios contribute flow to more unstable. Moreover, note that solid curves almost overlap, while the dashed curves are not as close to each other. Figure 44 demonstrates the concentration field at much later time $h/h_0=4$ by different sets of α . Not only the finger lengths of different cases are very close, but the morphology in each set is quite similar. This indicates that lifting fluid with nonmonotonic viscosity profile is quite insensitive to modifications in the viscosity contrast α .

Manickam and Homsy [10] found that nonmonotonic viscosity profile can be divided into an unstable zone (from injection fluid to the viscosity

maximum μ_m) and a stable zone (from viscosity maximum μ_m to displaced fluid). Vorticity image of the four nonmonotonic viscosity profiles we chosen are shown in Fig. 45. Like the dual vortex pair in injection fluid, the inner vortexes become weak as the difference between α and μ_m decrease. However, the area of inner vortex ring in lifting flow are less than in injection one. Because inner vortex ring means stable zone of the viscosity profile, it takes a very faint influence in stability and indicate the stable zone in lifting case play less effect than injection one. Compare the dimensionless interfacial length L_s in term of h/h_0 which illustrated in Fig. 43 with $Pe=3000$, even now its relatively large variation between values of 3 and 15, a small difference in α can dramatically influence the result in time evolution of the interfacial length L_s . This is far different from the role of α which play in injection flow (discussed before in Section 3.2.2), which implies the stable zone of nonmonotonic viscosity profile plays less effect in lifting flow than injection scenario.

4.4.3 Influence of the location of the maximum viscosity c_m

In order to study the influence of c_m , we present a series of numerical simulations under equivalent conditions. The viscosity profiles are illustrated in Fig. 46. Because higher c_m would easy to cause our numerical code become unstable, in order to assess the magnitude of this effect, we carried out a relevant parameter set in which Pe , α and μ_m were kept constant, which fingering generated by different sets of c_m . A comparison shows that approximately the same number of fingers develops in Fig. 47 (a) and (b), and the formation where tip-splitting and side-branch events can be observed. Viscous fingers in Fig. 47 (a) are more plentiful than (b). The behavior of the dimensionless interfacial length L_s in term of h/h_0 for four sets of nonmonotonic viscosity profiles are depicted in Fig. 48 also illustrated that as c_m decrease, lead to intricate morphologies, the fluid

demonstrate more vigorous fingering. Although as the Péclet number decrease to close to critical number Pe_c demonstrated by Tan and Homsy [1], stability of the scenario did not follow the rule we found. However, in this scenario the fingering is not mature, render parameters vary ineffective. It acceptable to neglect the error in predicts.

Another important interfacial behavior need be studied more quantitatively is the one related to different morphological interfacial features induced by end-point viscosity contrast α and the location of the maximum viscosity c_m . Because higher c_m leads the μ_m closer to the outer fluid in lifting flow. Especially with favorable end-point viscosity contrast case, it cause steeper slope in unstable zone, may lead to more violent phenomenon. To find the interaction between the two parameters, we choose a favorable end-point viscosity contrast ($\alpha=0.25$) equal the inverse of unfavorable scenario ($\alpha'=1/\alpha=4$) for other parameters $Pe=3000$ and $\mu_m=8$ are held constant. Figure 49 illustrates the concentration images of the simulation. The overall patterns show great similarities in favorable and unfavorable case (top law and bottom law), however, far different from (first column and second column) with various c_m . The phenomenon indicates insignificant influences of the local correlations between fluid α and c_m .

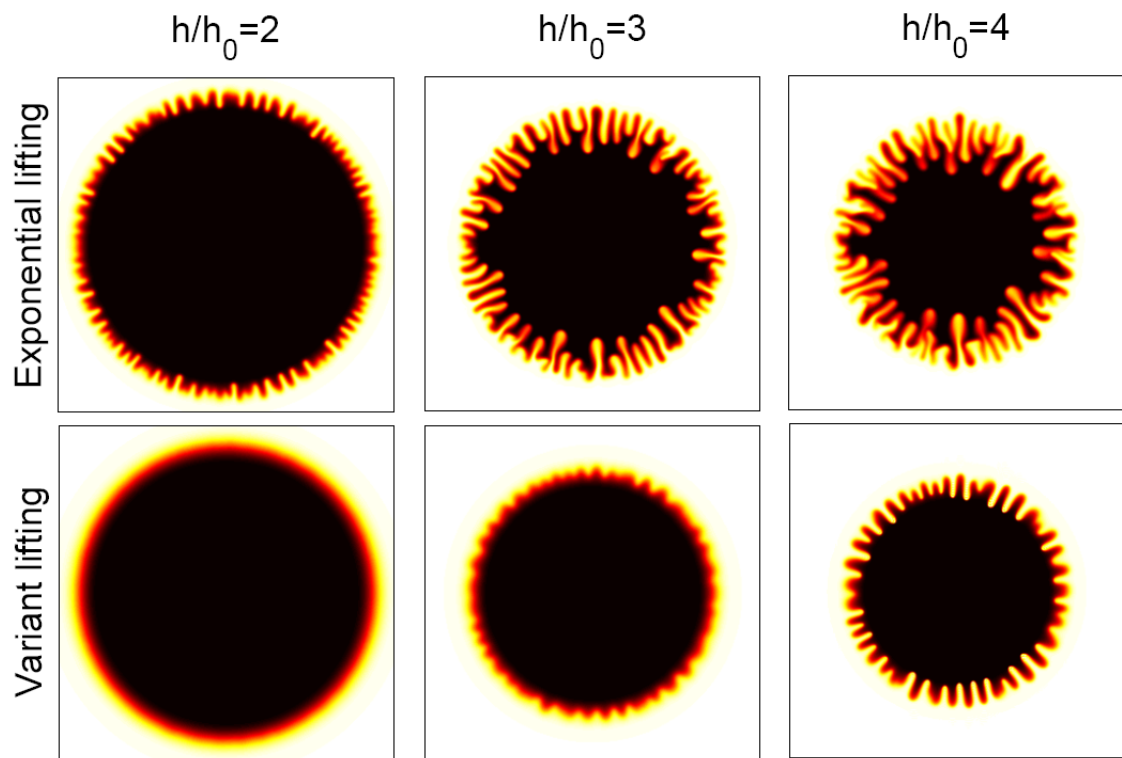


Figure 26: Concentration images for the dimensionless gap distances $h/h_0=2, 3,$ and $4,$ for the cases of exponential lifting (top row), and variant lifting (bottom row) to the parameter set as $Pe=3000, A=0.925.$ The domain of x and y axis are -0.8 to $0.8.$

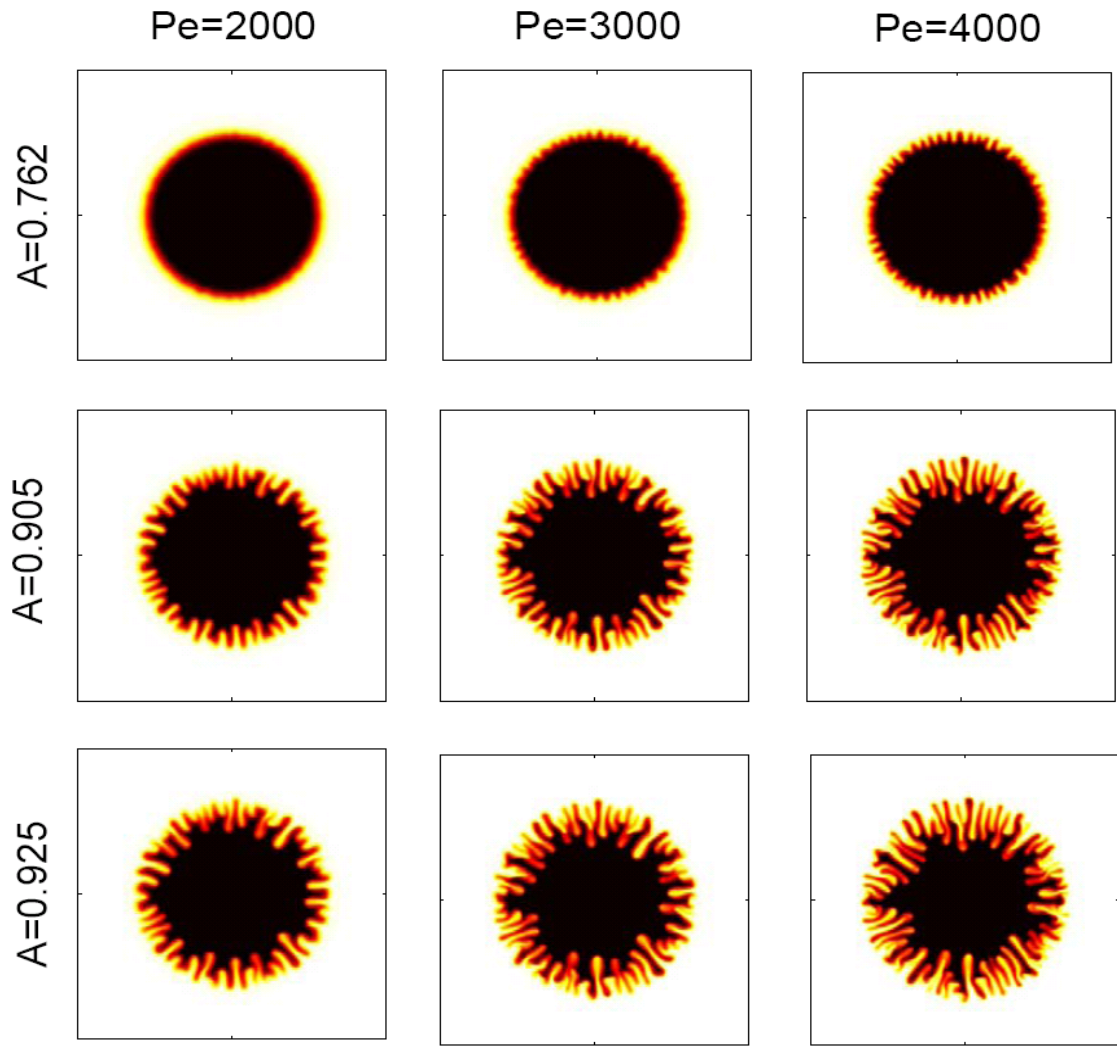


Figure 27: Concentration images for $Pe=2000$ (first column), 3000 (second column), 4000(third column), and $A=0.762$ (top row), 0.905 (mid row), 0.925 (bottom row) at dimensionless gap distances $h/h_0=4$, for the cases of exponential lifting. The domain of x and y axis are -0.5 to 0.5 .

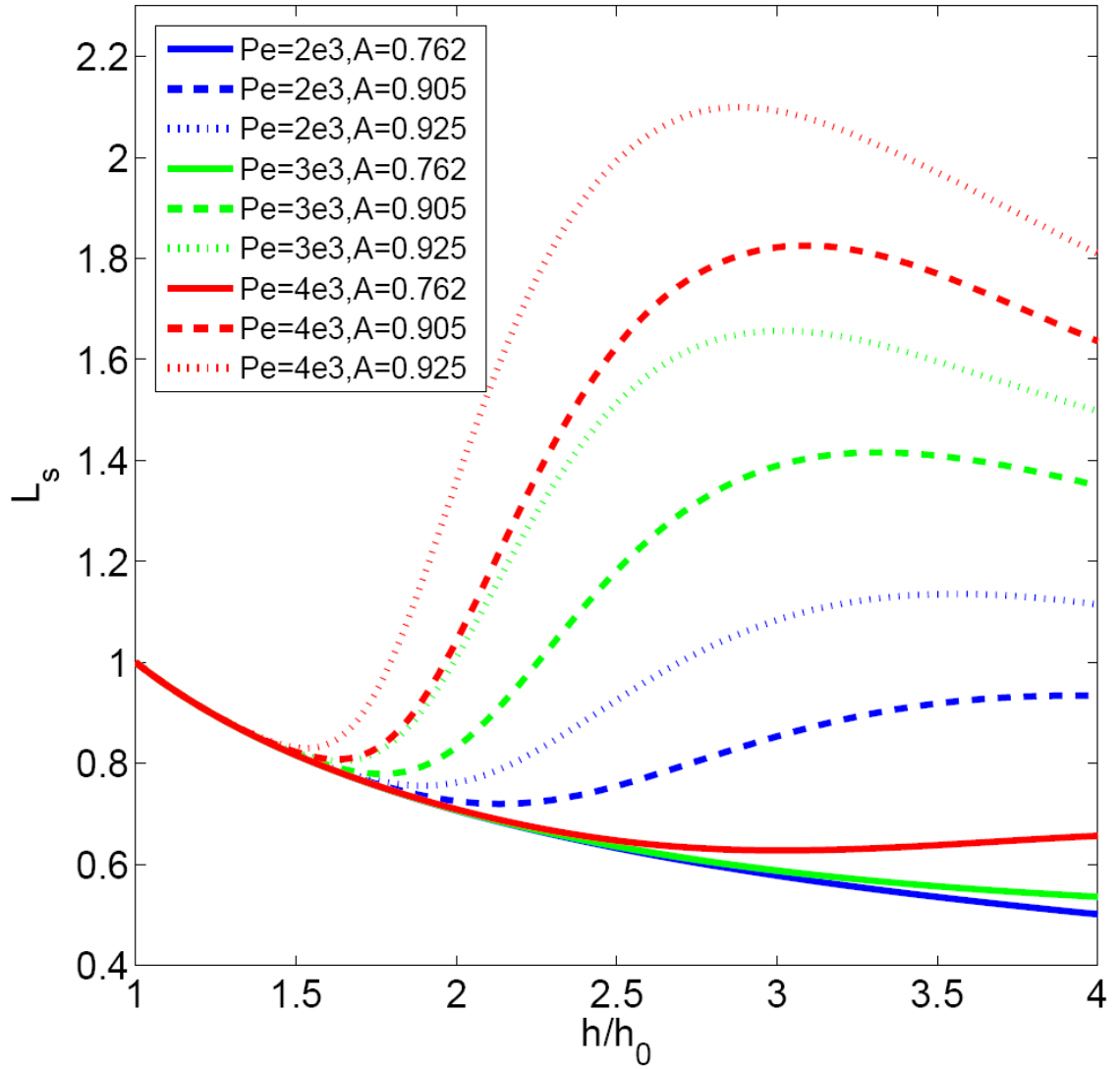


Figure 28: Interfacial lengths L_s as a function of the dimensionless gap distance h/h_0 for the exponential lifting case. These simulations used the same physical parameters as in Fig. 27. In the inset the numbers label the distinct Pe and A sets.

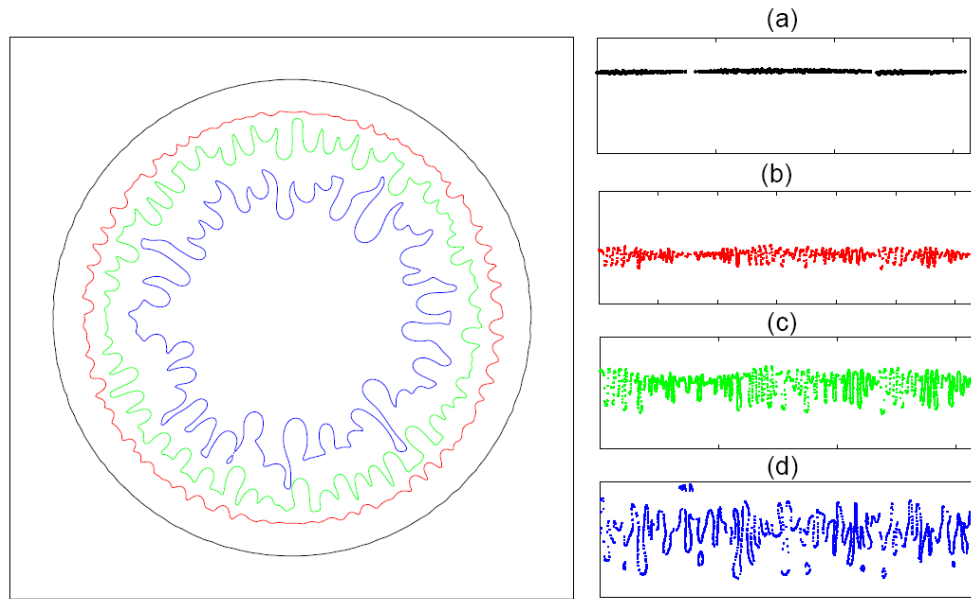


Figure 29: A dimensionless gap distances h/h_0 series of the contours on the concentration to the parameters sets as $Pe=3000$, $A=0.925$ for the exponential lifting case. For the dimensionless gap distance $h/h_0=$ (a) 1.5, (b) 2, (c) 2.5, and (d) 4.

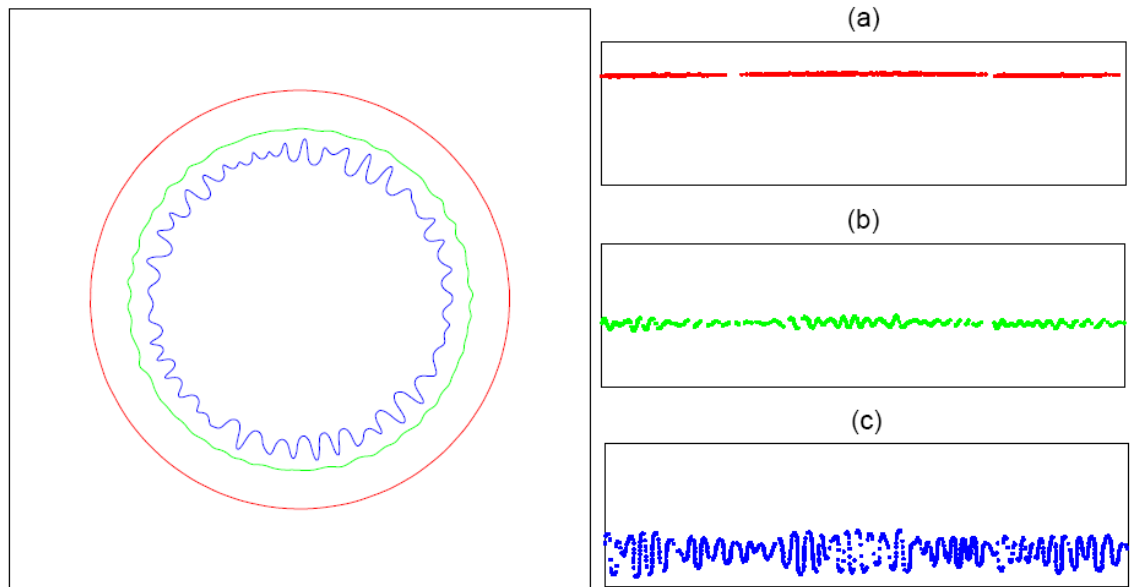


Figure 30: A dimensionless gap distances h/h_0 series of the contours on the concentration to the parameters sets as $Pe=3000$, $A=0.925$ for the variant lifting situation. For the dimensionless gap distance $h/h_0=$ (a) 1.5, (b) 2, (c) 2.5, and (d) 4.

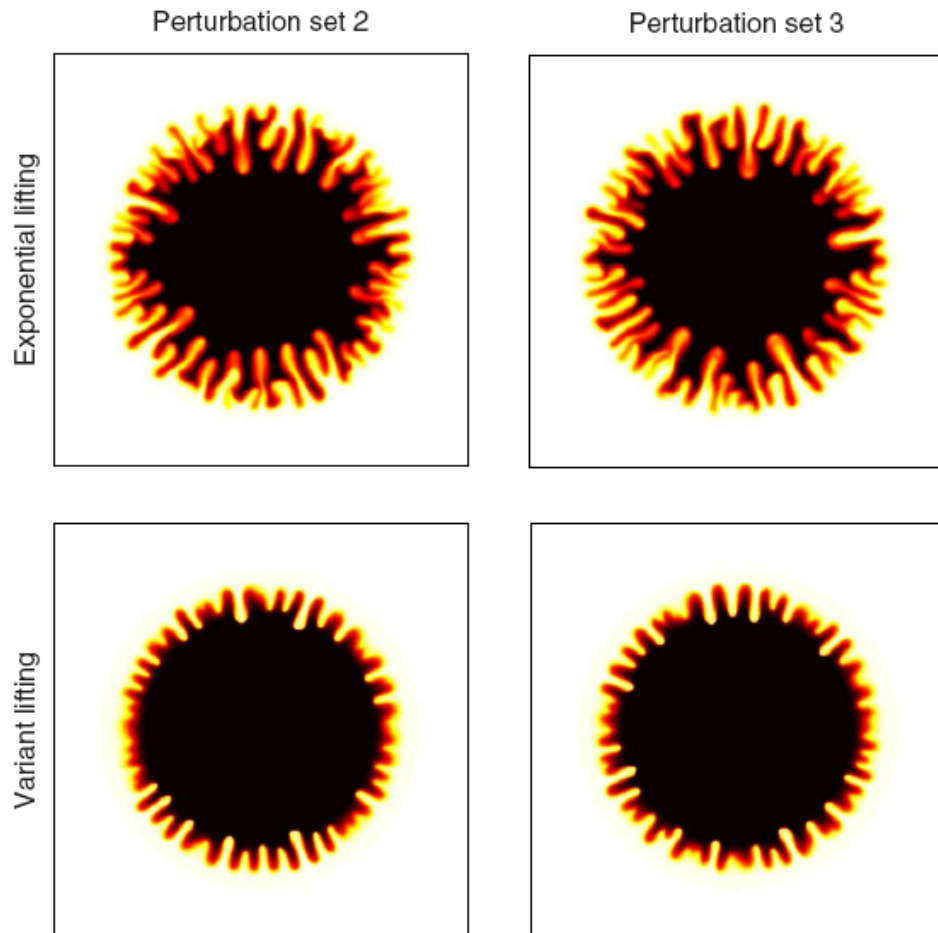


Figure 31: Concentration images for the dimensionless gap distance $h/h_0=4$ for the cases of exponential lifting (top row), and variant lifting (bottom row). These simulations used the same physical parameters as in Fig. 26, but utilized two distinct set of initial random conditions: perturbation set 2 (first column), and perturbation set 3 (second column).

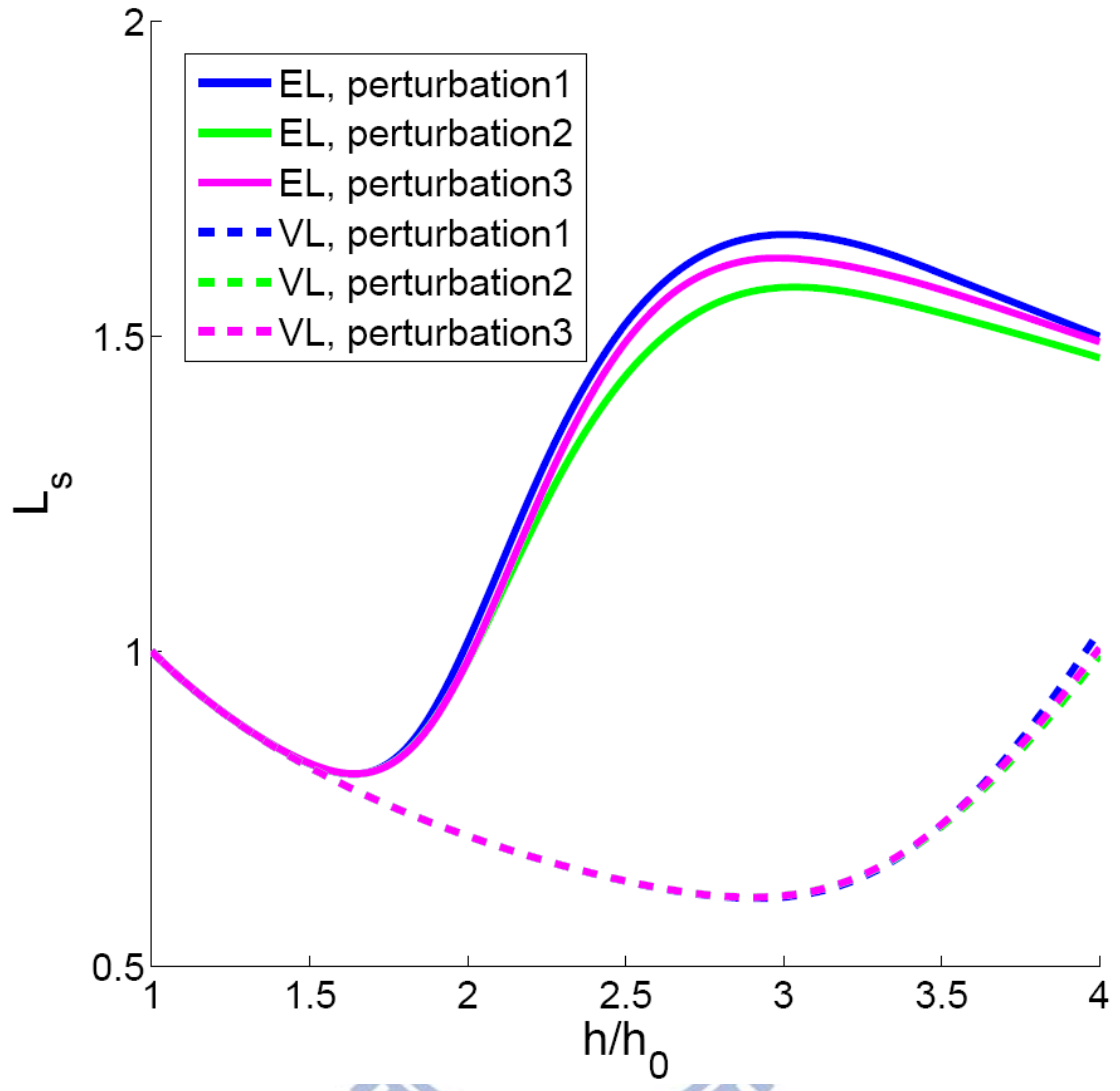


Figure 32: Interfacial length L_s as a function of the dimensionless gap distance h/h_0 for the exponential lifting (*EL*) case, and three different sets of initial perturbations (solid curves). The dashed curves represent similar sets of data for the variant lifting (*VL*) situation. In the inset the numbers label the distinct perturbation sets.

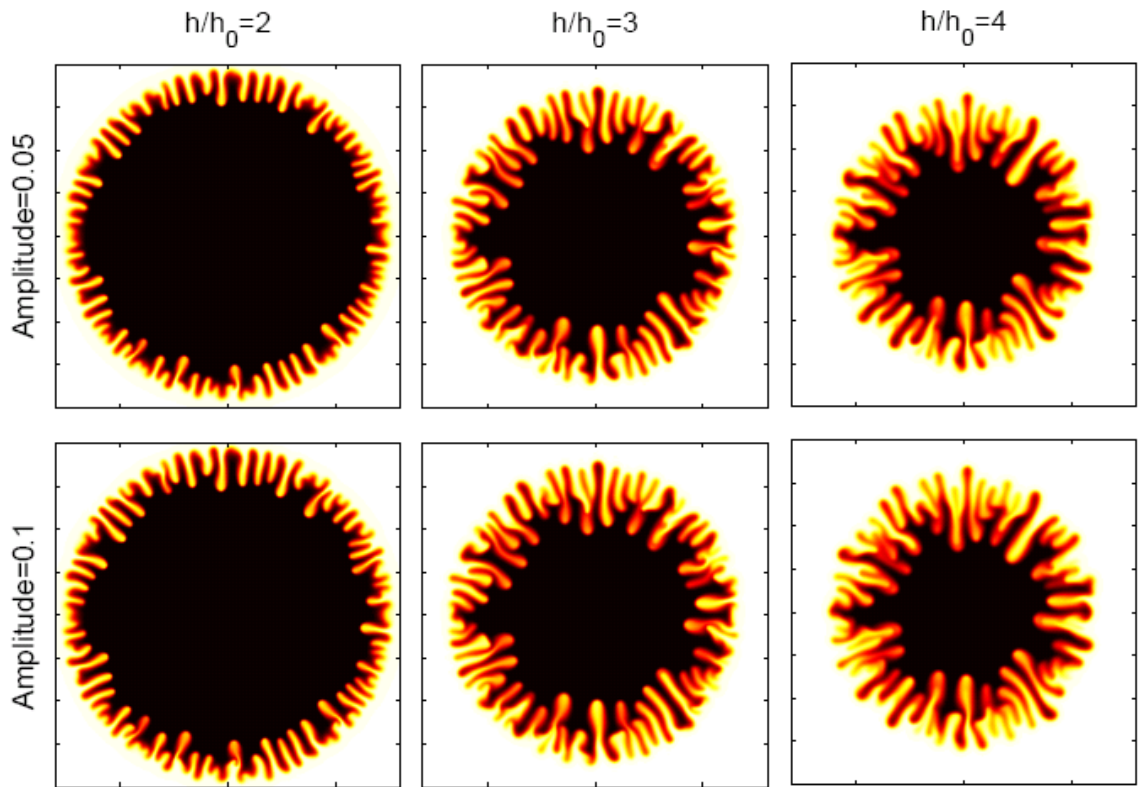


Figure 33: Concentration images for the dimensionless gap distance $h/h_0=2$, 3, and 4 for the cases of exponential lifting. These simulations used the same physical parameters as in Fig. 29, but utilized two distinct set of initial random conditions: amplitude=0.05 (top row), and amplitude=0.1 (bottom row).

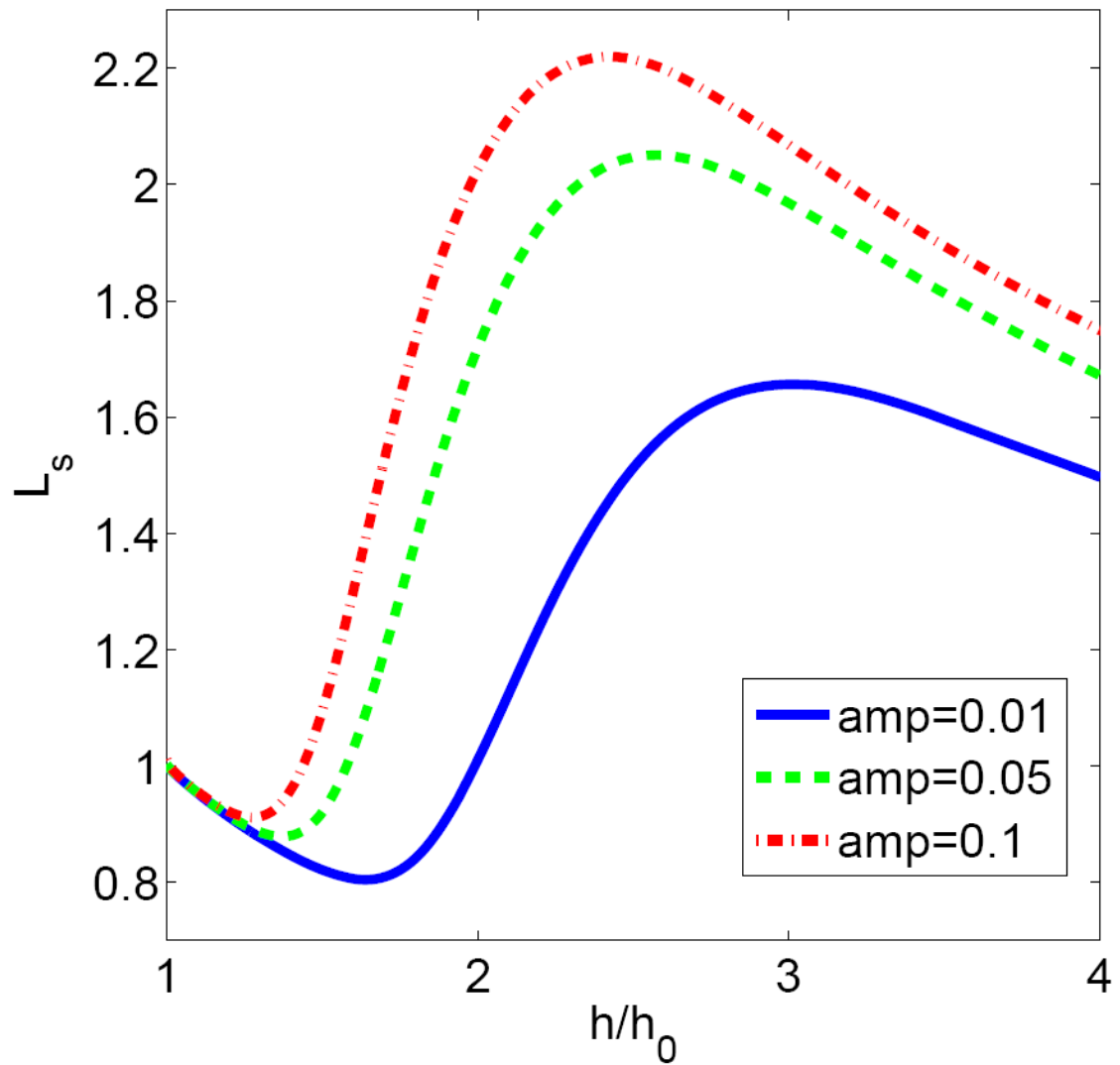


Figure 34: Interfacial lengths L_s as a function of the dimensionless gap distance h/h_0 for the exponential lifting case. These simulations used the same physical parameters as in Fig. 27. In the inset the numbers label the amplitude sets.

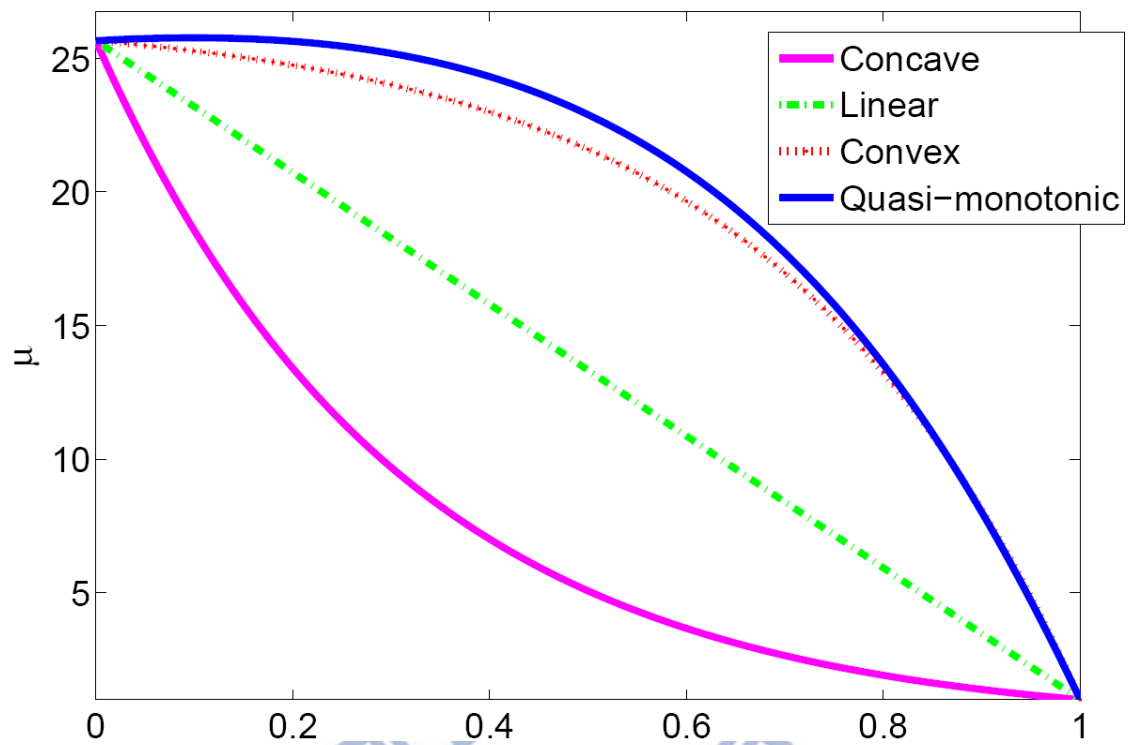


Figure 35: Four kinds of viscosity profiles with $A=0.925$ ($\alpha=25.67$). The parameters set of the Quasi-monotonic viscosity profile is $c_m=0.1$ and $\mu_m=25.77$.

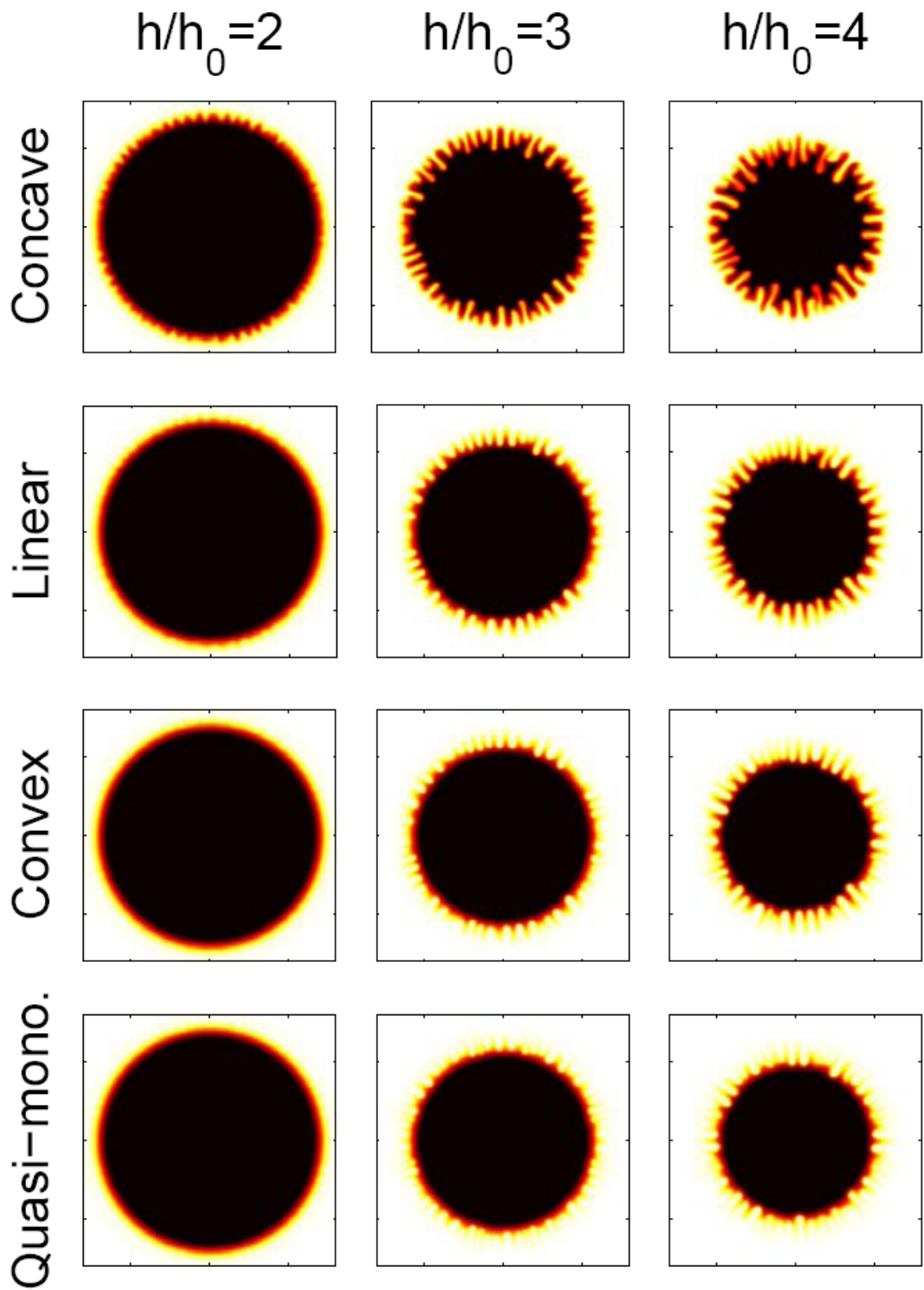


Figure 36: Concentration images for the dimensionless gap distance $h/h_0=2$, 3, and 4, for the cases in Fig. 35 with $Pe=2000$ and $A=0.925$ for (a) Concave (b) Linear (c) Convex (d) Quasi-monotonic. The inner fluid is more viscous ($\mu_2 > \mu_1$).

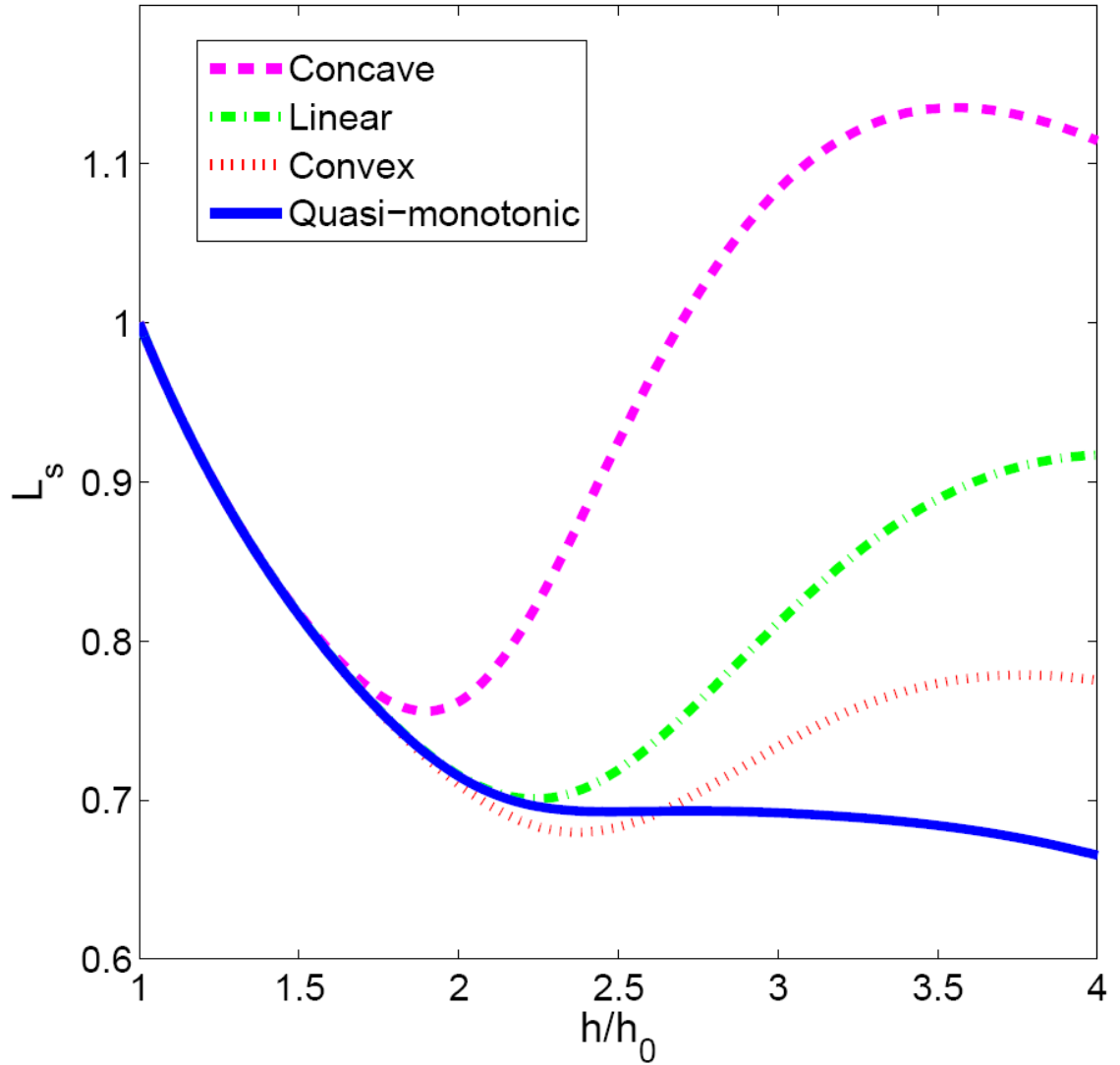


Figure 37: Interfacial length L_s as a function of the dimensionless gap distance h/h_0 for the exponential lifting case and four kinds of different viscosity profiles for Fig. 35 with $Pe=2000$. In the inset the numbers label the distinct viscosity profiles.

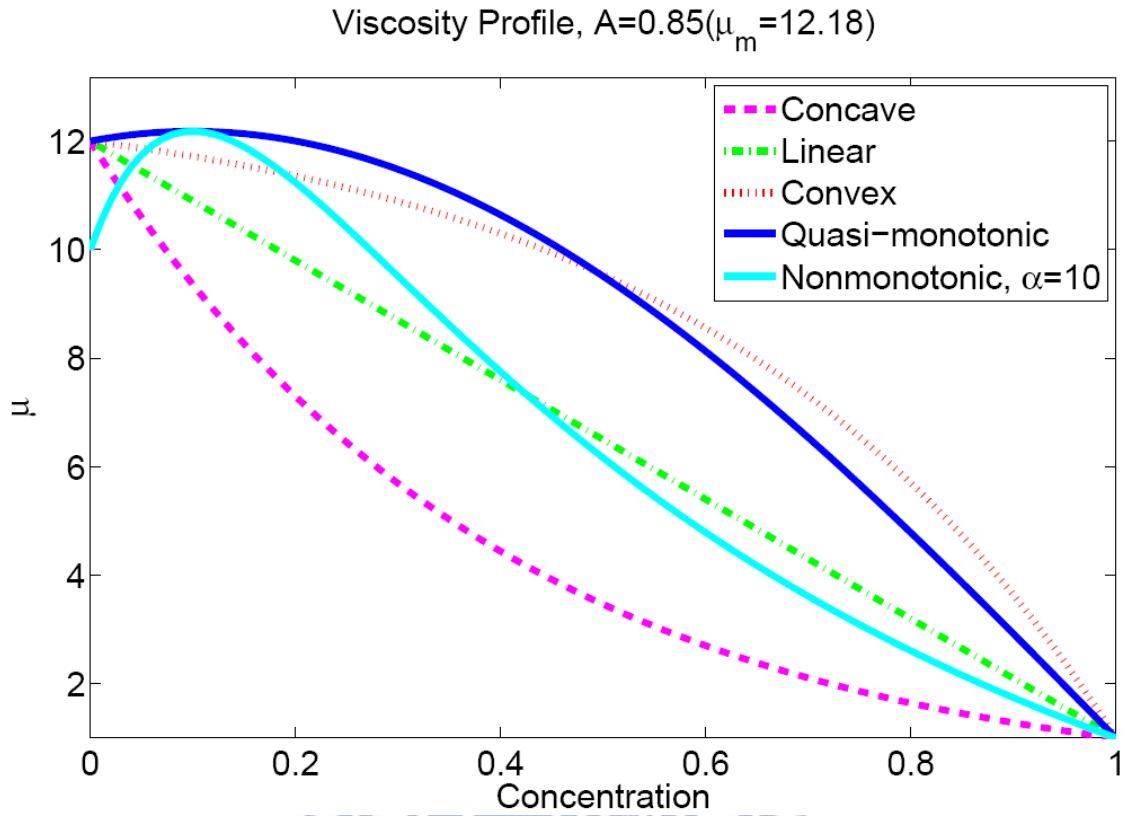


Figure 38: Five kinds of viscosity profiles with $A=0.848$ ($\mu_m=e^A=12.18$). The parameters set of the nonmonotonic viscosity profile is $c_m=0.1$ and $\alpha=10$.

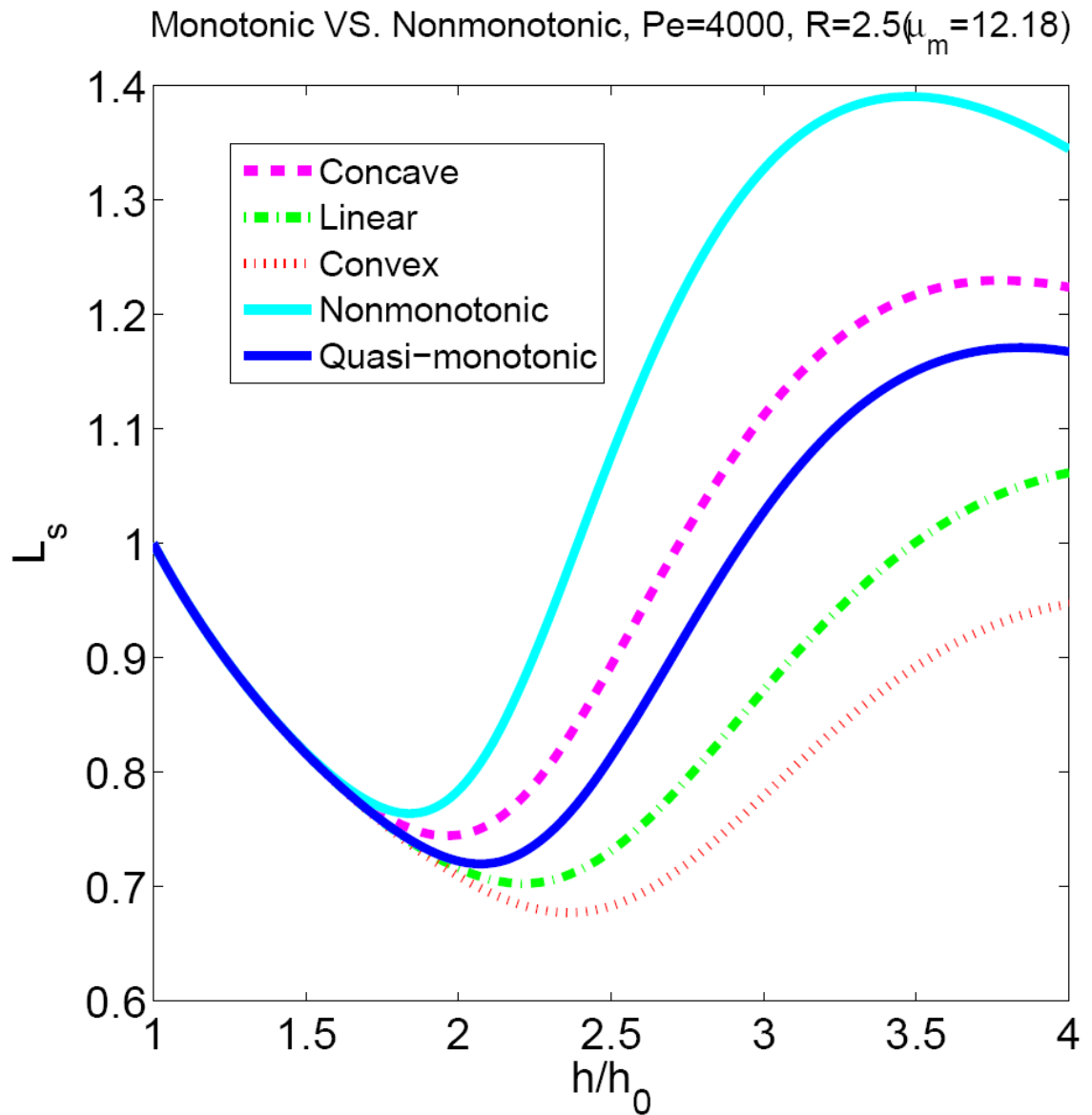


Figure 39: Interfacial length L_s as a function of the dimensionless gap distance h/h_0 for the exponential lifting case and five viscosity profiles in Fig. 38 with $Pe=4000$. In the inset the numbers label the distinct viscosity profiles.

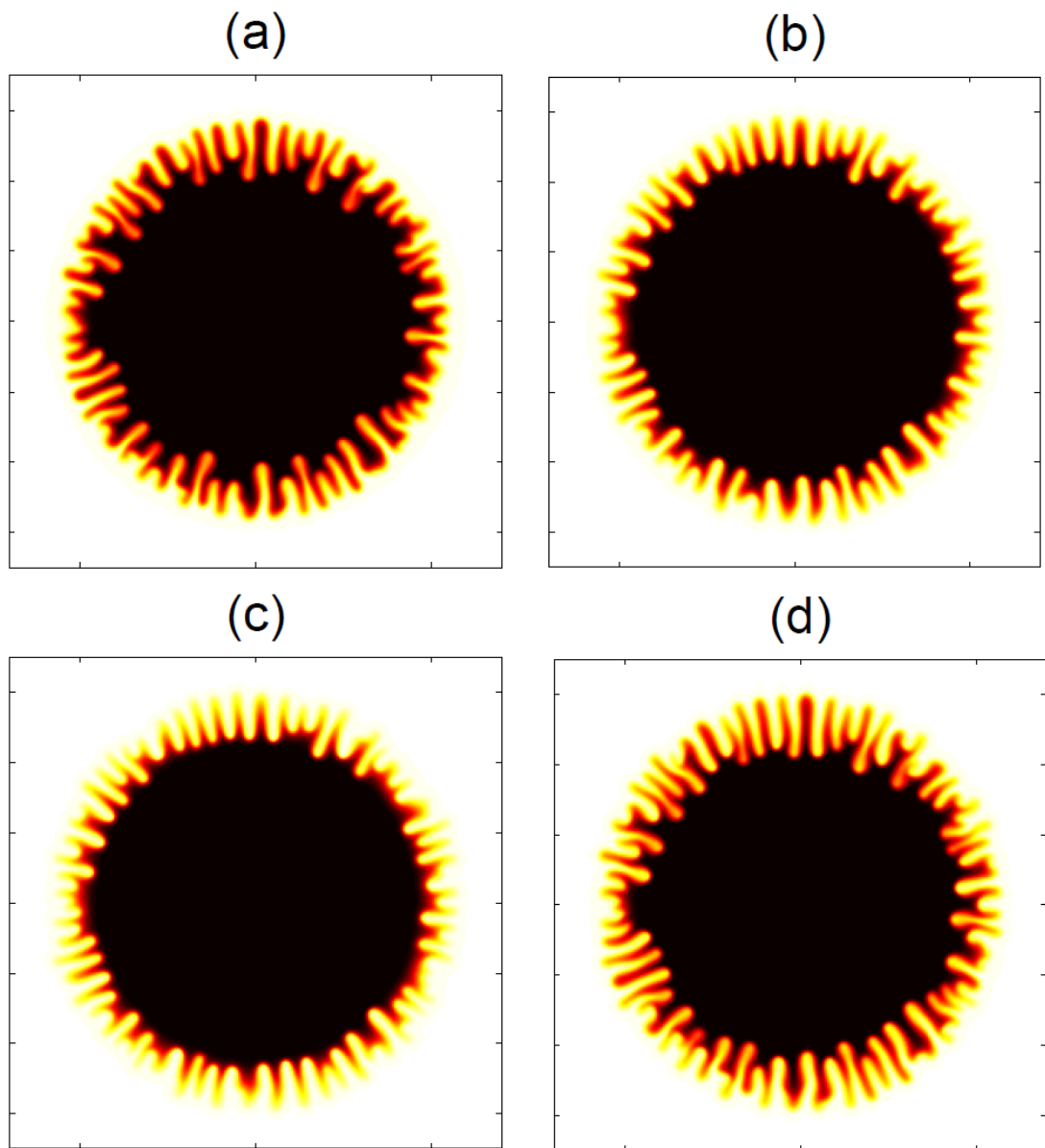


Figure 40: Concentration images for the dimensionless gap distance $h/h_0=4$ with $Pe=4000$, for the viscosity profile depicted in Fig. 38 for (a) Concave (b) Linear (c) Convex (d) Nonmonotonic, $\alpha=10$. The inner fluid is more viscous ($\mu_2 > \mu_1$).

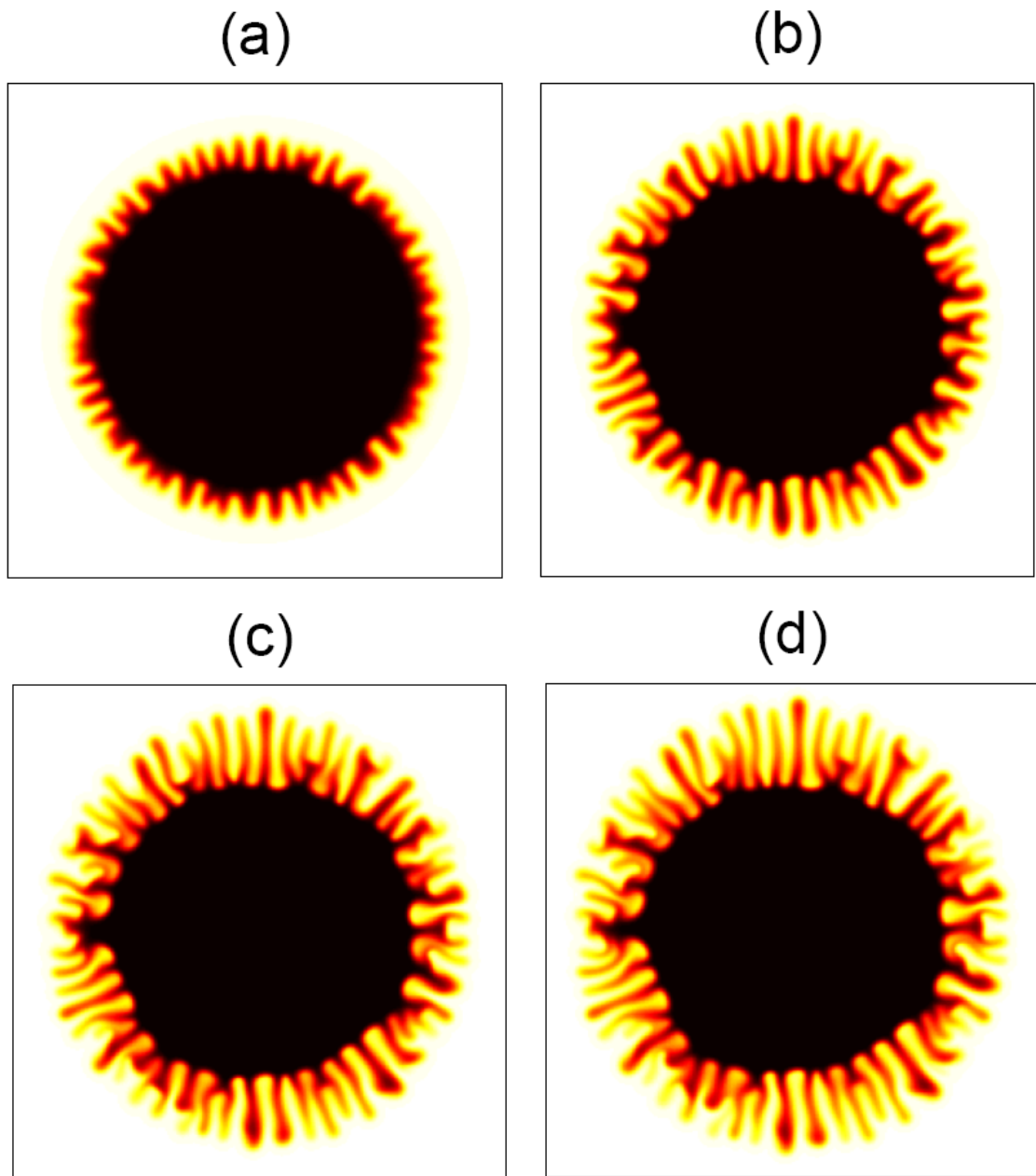


Figure 41: Concentration images of parameters set $\alpha=3$ and $c_m=0.1$ with $Pe=3000$ for the exponential lifting case (a) $\mu_m=8$, (b) $\mu_m=16$, (c) $\mu_m=24$ and (d) $\mu_m=32$ for the dimensionless gap distance $h/h_0=4$,

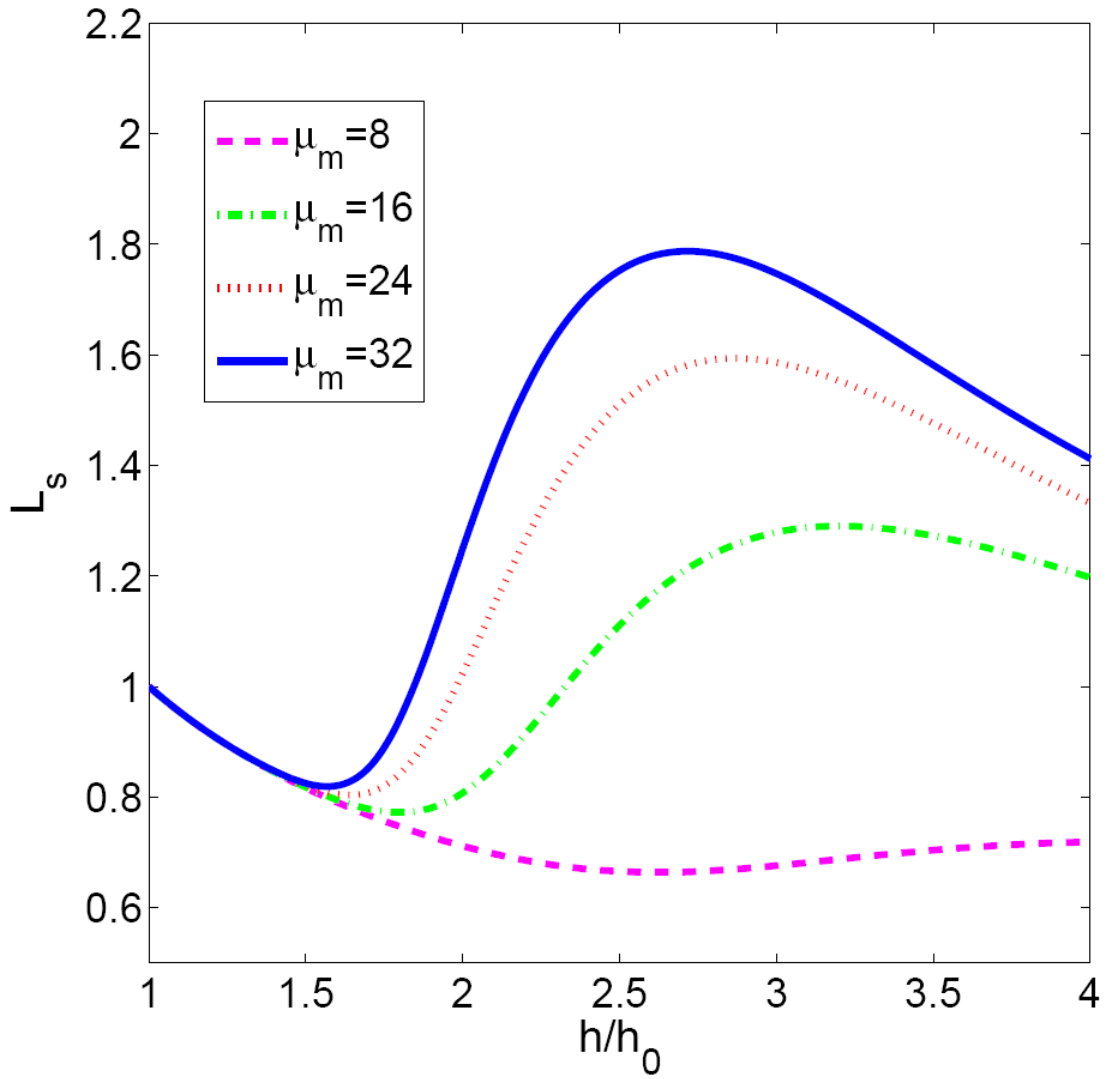


Figure 42: Interfacial length L_s as a function of the dimensionless gap distance h/h_0 for the four cases shown in Fig. 41. In the inset the numbers label the distinct maximum viscosity μ_m .

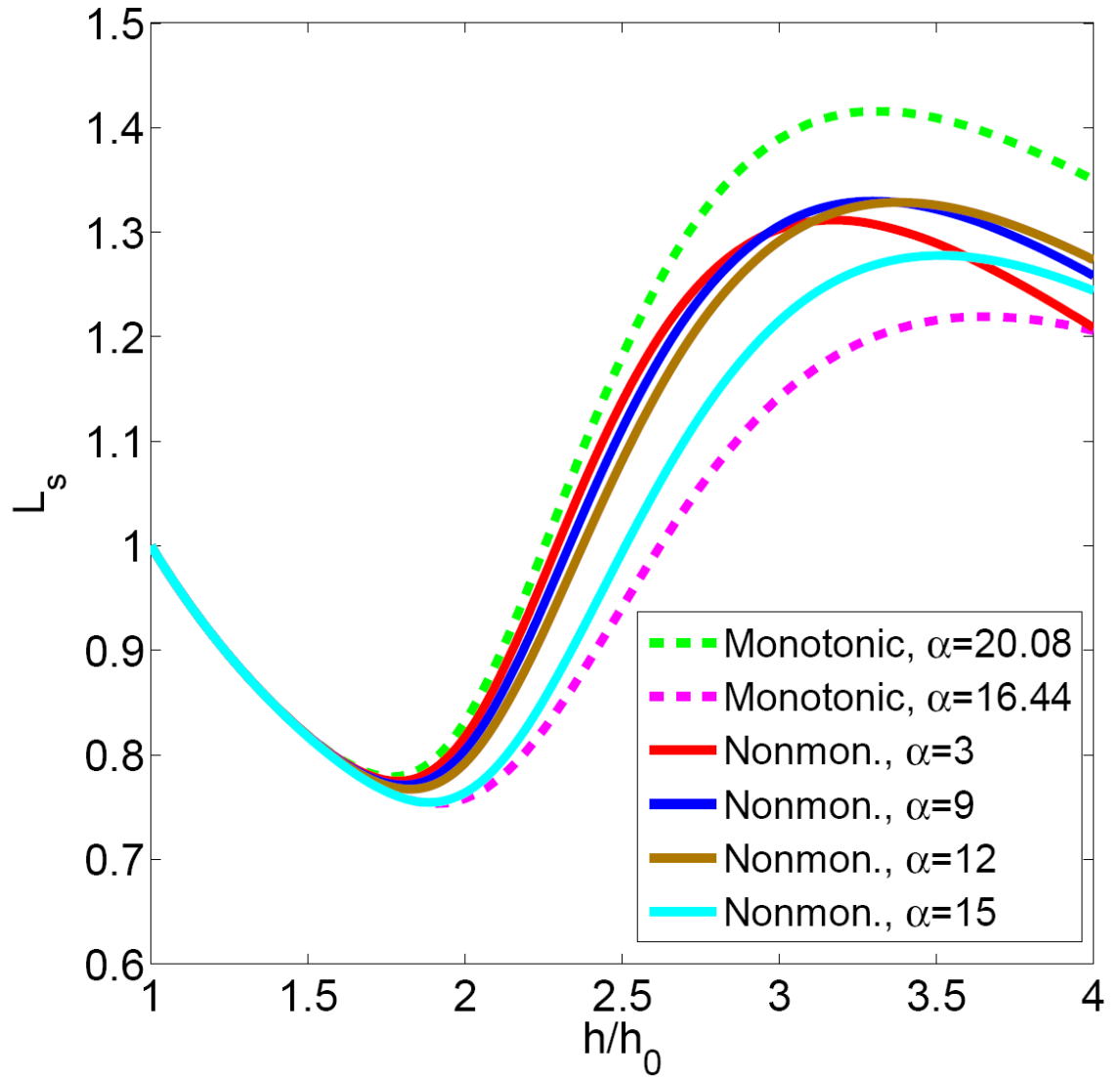


Figure 43: Time evolution of the interfacial length L_s for two monotonic viscosity profiles with $\alpha=20.08$ and 16.44 and four nonmonotonic viscosity profiles with $\mu_m=16.44$, $c_m=0.1$, $\alpha=3, 9, 12$, and 15 for $Pe=3000$. In the inset the detail viscosity profiles for the seven parameters sets.

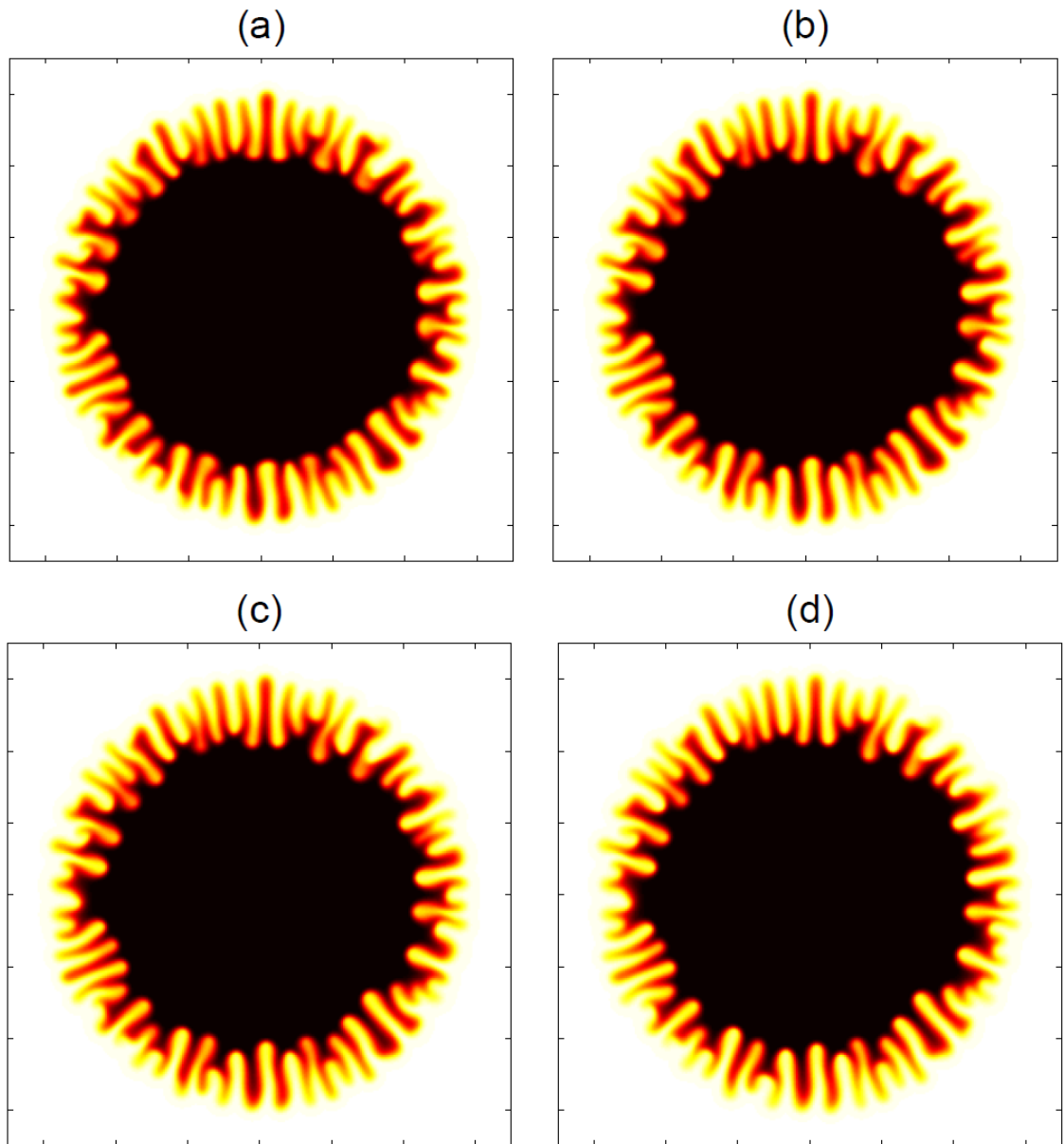


Figure 44: Concentration images of parameters set $\mu_m=16.44$ and $c_m=0.1$ with $Pe=3000$ for the exponential lifting case (a) $\alpha=3$, (b) $\alpha=9$, (c) $\alpha=12$ and (d) $\alpha=15$ for the dimensionless gap distance $h/h_0=4$. Despite the finger lengths of different cases are very close; the morphology in each set is quite similar.

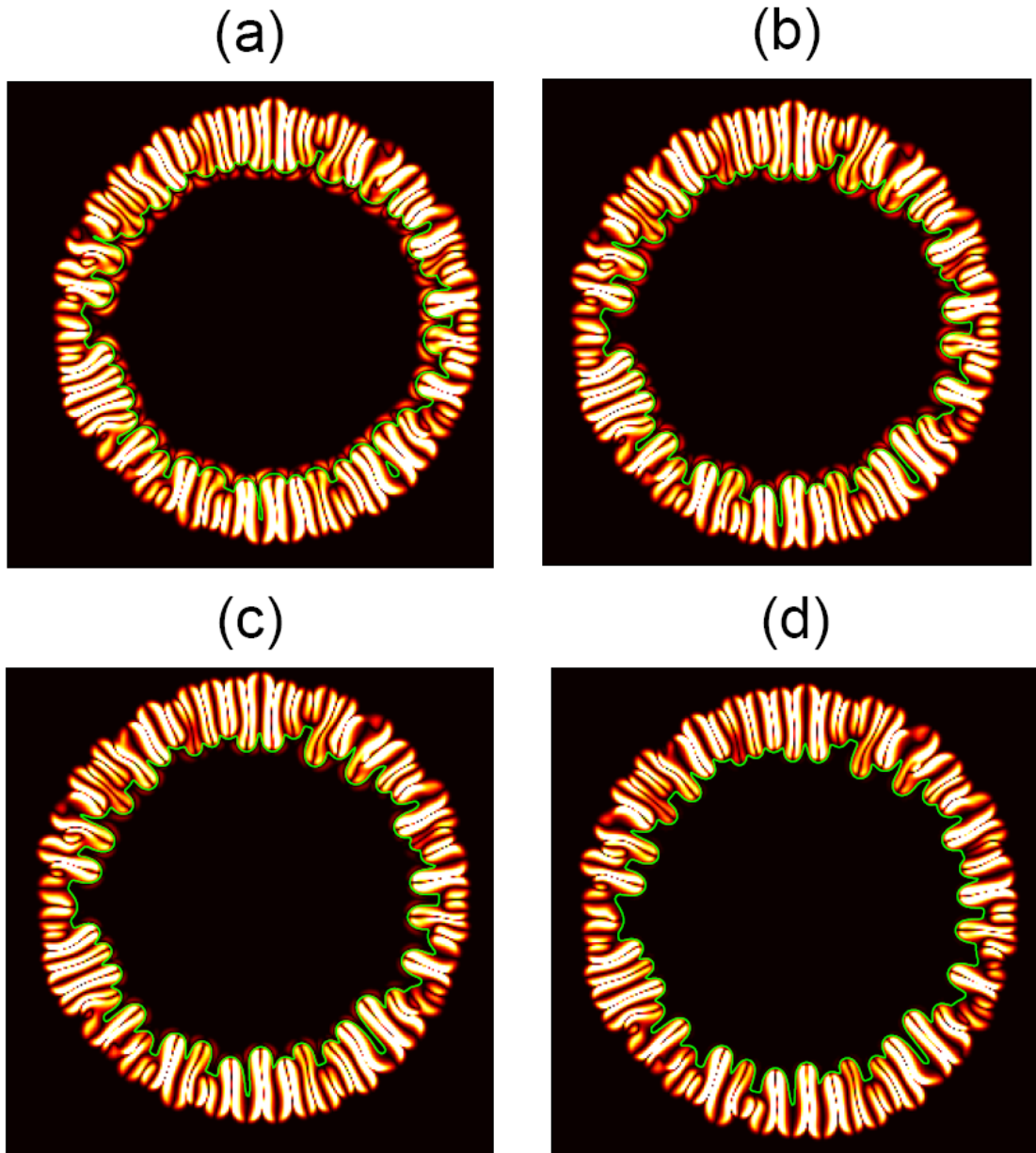


Figure 45: Correspondent images of vorticity for the cases shown in Figure 43 for the dimensionless gap distance $h/h_0=4$, (a) $\alpha=3$; (b) $\alpha=9$; (c) $\alpha=12$ and (d) $\alpha=15$ for $Pe=3000$. Unlike the inner fingers in injection flow, it may become disappear, as the difference between α and μ_m decrease.

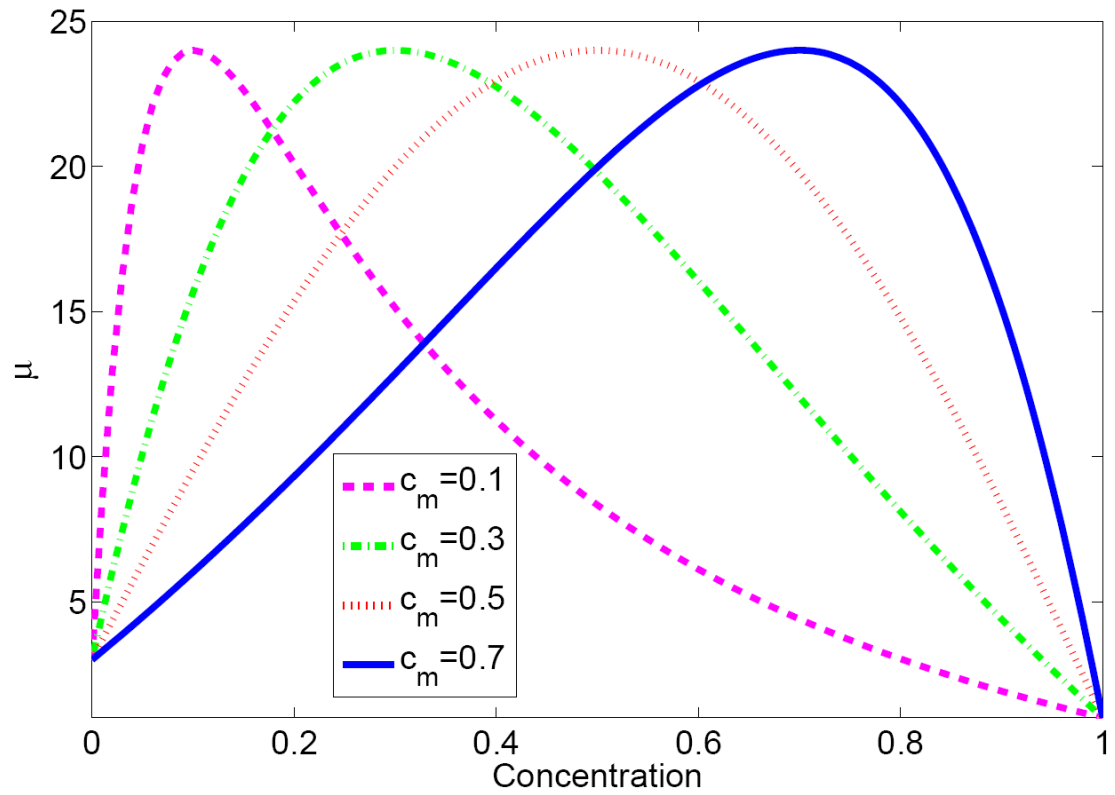


Figure 46: Representative profiles of non-monotonic viscosity profiles show end-point viscosity contrasts with $\alpha=3$, $\mu_m=24$ for $c_m=0.1$, 0.3, 0.5 and 0.7.

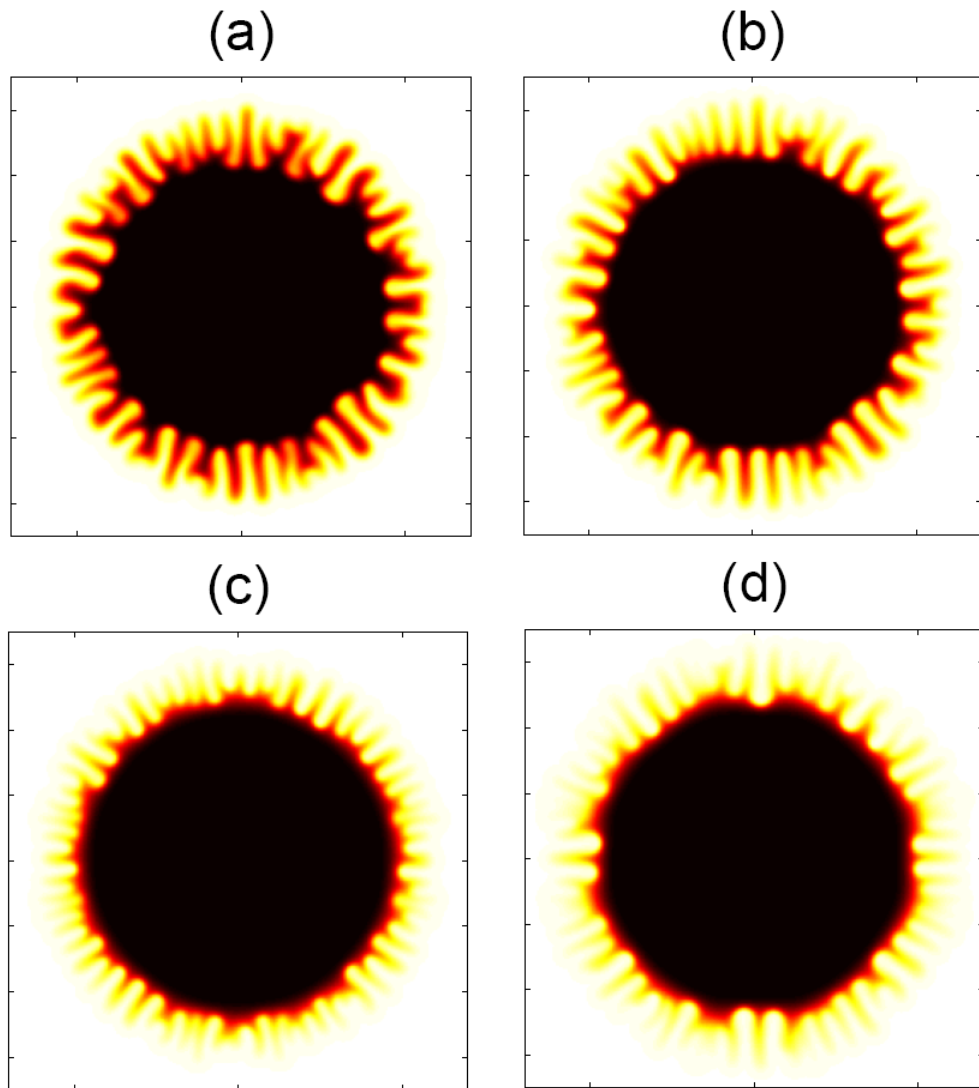


Figure 47: Concentration images for the dimensionless gap distance $h/h_0=4$ with the non-monotonic viscosity profiles shown in Fig. 46 with $Pe=2000$ for series of (a) $c_m=0.1$, (b) $c_m=0.3$, (c) $c_m=0.5$ and (d) $c_m=0.7$.

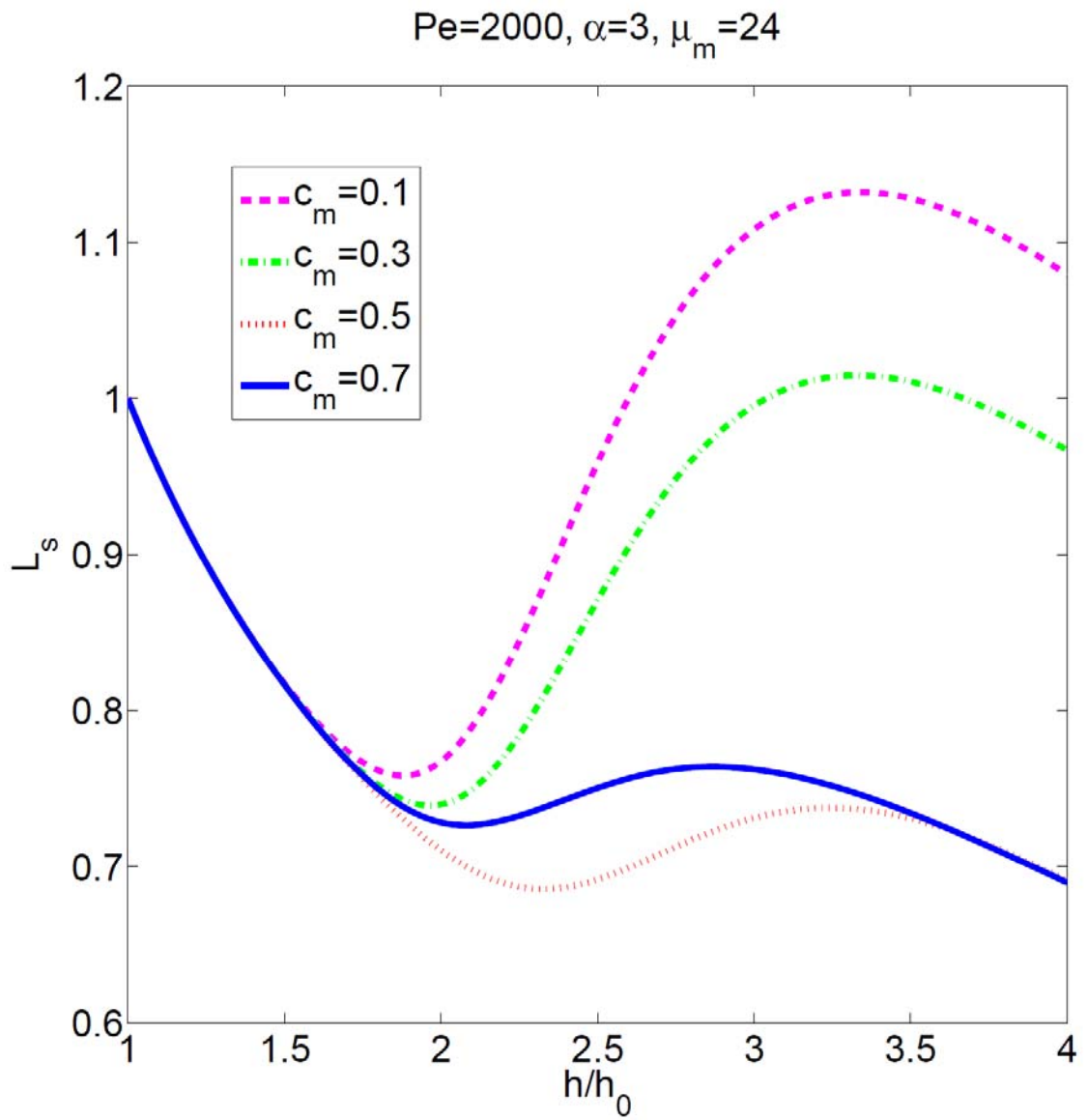


Figure 48: Time evolution of the interfacial length with viscosity profile $\alpha=3, \mu_m=24$ with $Pe=2000$ for $c_m=0.1, 0.3, 0.5$ and 0.7 .

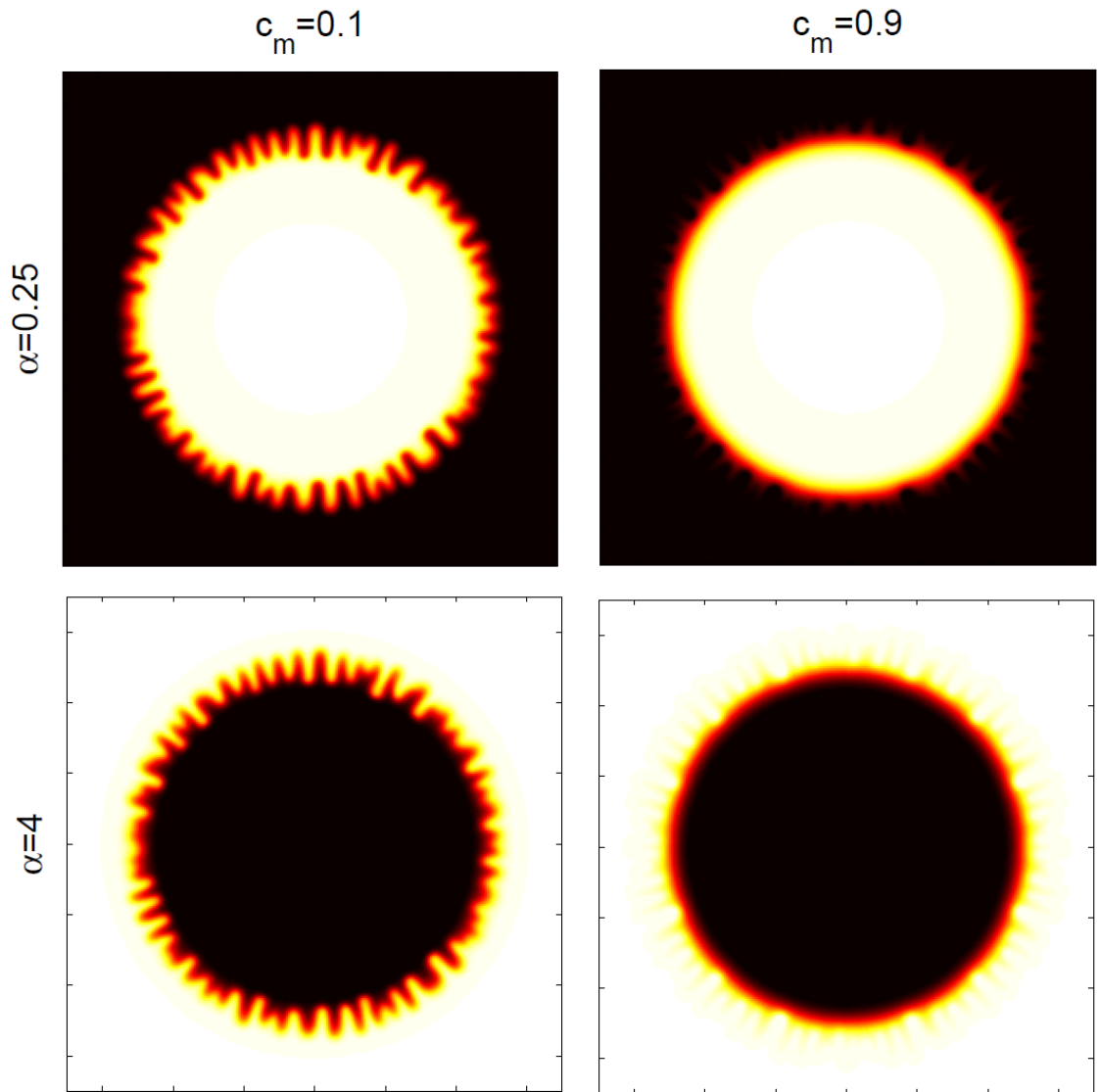


Figure 49: Concentration images for the dimensionless gap distance $h/h_0=4$ for the favorable end-point contrast cases of $\alpha=0.25$ (top row), and the unfavorable end-point contrast cases of $\alpha=4$. Utilized two distinct set of the location of the maximum viscosity: $c_m=0.1$ (first column), and $c_m=0.9$ (second column). Other parameters set are $Pe=3000$ and $\mu_m=8$.

Chapter 5 Conclusions and Recommendations of Future Work

5.1 Conclusions

This study analyzes both of the injection flow and the lifting flow by highly accurate simulation with different viscosity profiles. In this chapter, the major findings of the thesis are summarized as follows in turn as: 1) injection flow; 2) lifting flow in Hele-Shaw Cell, with the monotonic and nonmonotonic viscosity profile, respectively.

5.1.1 Fingering Instability of Miscible Injection Hele-Shaw Flows

Usual miscible flows in radial Hele-Shaw geometry lead to the formation of complex morphological structures. In this work, we have presented highly accurate numerical simulations for an injection-driven radial Hele-Shaw flow with miscible fluids. The present investigation explores the influence of these parameters up to values of $R=2$ ($A=0.762$, $\alpha=7.34$) and $Pe=800$ with both monotonic and nonmonotonic viscosity profiles to study the effect of different viscosity profiles, then higher to the values of $\alpha=14$ and $\mu_m=14.1$ to investigate the nonmonotonic viscosity profiles.

The interfacial instabilities have been analyzed systematically both qualitatively and quantitatively. The results of this study have indicated that the differences in different viscosity profiles might not be significant, but it reveals interesting nonlinear behaviors when nonmonotonic viscosity profiles is cross the convex viscosity profile. Our analysis with nonmonotonic viscosity profiles explicitly indicates how the relevant parameters of the system influence the morphology of the interfacial patterns.

First, we studied the stability problem: as the Péclet number is higher than the critical Péclet number Pe_c , the convection dominate the flow. The

disturbances grow with increase in the Péclet number Pe and the maximum viscosity μ_m , vice versa. It is an interesting phenomenon that the interfacial lengths will reveal a damping effect when the favorable end-point viscosity contrasts α with high maximum viscosity μ_m .

In contrast, the effect of the end-point viscosity contrast α and the location of the maximum viscosity c_m to the stability of fluid are complicated. Both the variable in the location of the maximum viscosity c_m and the end-point viscosity contrast α is in good agreement with the prediction as state in our previous analysis.

5.1.2 Controlling Radial Fingering Patterns in Miscible Lifting Hele-Shaw Flow

Time-dependent gap flows in radial Hele-Shaw geometry lead to the formation of complex morphological structures if the cell's gap width grows exponentially with time. The parameters Pe and viscosity contrast A or μ_m are quite intuitive as expected and that demonstrate more vigorous fingering. Nevertheless, the difference of different viscosity profile to lifting Hele-Shaw cell still remains an open question.

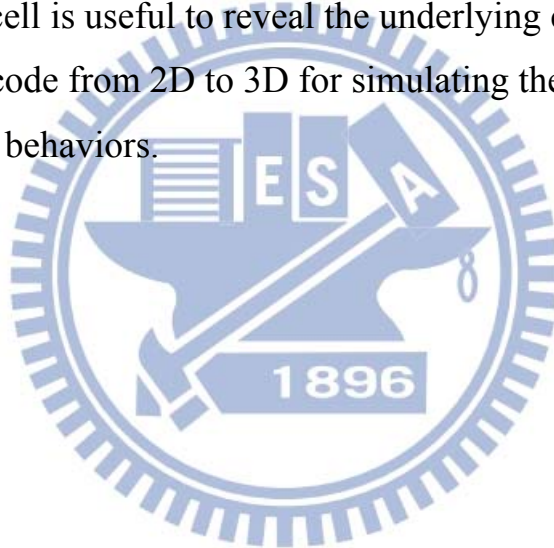
In this work, we have presented highly accurate numerical simulations to prove exponentially varying time dependent gap width leading to the formation of more complex morphological structures than variant lifting in the beginning. Then we investigate the influence of different viscosity profile in a lifting Hele-Shaw cell. We find that in monotonic viscosity profiles, the instability of fluid is always follows the series of concave, linear and convex. However, nonmonotonic viscosity is not unconditionally more unstable than monotonic ones, unless the curve of nonmonotonic case crosses the convex curve. Moreover, we have verified that the viscosity profile changes quite sensitively in higher Péclet number and the inner

vortices in lifting flow are weaker than the injection flow.

5.2 Recommendations of Future Work

Based on these achievements, the directions of research recommended for further study are summarized as follows:

- (1) In conclusion, we hope experimentalist will feel motivated to check, and hopefully validate the ideas put forward in this work.
- (2) To study the effect of chemistry both in injection and lifting flow. Most of the details of chemistry remain unclear due to the difficulties in detailed measurements. Using the developed tool to simulate the effect in Hele-Shaw cell is useful to reveal the underlying complex physics.
- (3) To extend the code from 2D to 3D for simulating the discharges with unsymmetrical behaviors.



Appendix 1 Vorticity

Following Darcy's (1856) investigations into the hydrology of the water supply, proportionality between flow rate and the applied pressure difference is expressed as:

$$\frac{\partial P}{\partial x} = -\frac{\mu}{k}u \quad (1.1)$$

$$\frac{\partial P}{\partial y} = -\frac{\mu}{k}v \quad (1.2)$$

As we know, $\omega = \frac{\partial v}{\partial x} - \frac{\partial u}{\partial y}$, given a differential equation of the form

$$\frac{\partial}{\partial y} \left(\frac{\partial P}{\partial x} \right) = \frac{\partial^2 P}{\partial x \partial y} = -\frac{\partial}{\partial y} \left(\frac{\mu}{k}u \right) \quad (1.3)$$

$$\frac{\partial}{\partial x} \left(\frac{\partial P}{\partial y} \right) = \frac{\partial^2 P}{\partial x \partial y} = -\frac{\partial}{\partial x} \left(\frac{\mu}{k}v \right) \quad (1.4)$$

Where eq. (1.3) is equal to eq. (1.4)

$$-\frac{\partial}{\partial y} \left(\frac{\mu}{k}u \right) + \frac{\partial}{\partial x} \left(\frac{\mu}{k}v \right) = 0 \quad (1.5)$$

The viscosity μ is supposed to be a function of the injecting fluid concentration and the permeability is a spatial distribution with the expression

$$\mu = \mu(c), k = k(x, y), \quad (1.6)$$

where

$$-\left(\frac{\mu}{k} \frac{\partial u}{\partial y} + \frac{u}{k} \frac{\partial \mu}{\partial c} \frac{\partial c}{\partial y} - u \frac{\mu}{k^2} \frac{\partial k}{\partial y} \right) + \left(\frac{\mu}{k} \frac{\partial v}{\partial x} + \frac{v}{k} \frac{\partial \mu}{\partial c} \frac{\partial c}{\partial x} - v \frac{\mu}{k^2} \frac{\partial k}{\partial x} \right) = 0$$

$$\frac{\mu}{k} \left(\frac{\partial u}{\partial y} - \frac{\partial v}{\partial x} \right) = \frac{1}{k} \frac{\partial \mu}{\partial c} \left(u \frac{\partial c}{\partial y} - v \frac{\partial c}{\partial x} \right) - \frac{\mu}{k^2} \left(u \frac{\partial k}{\partial y} - v \frac{\partial k}{\partial x} \right), \quad (1.7)$$

From streamfunction

$$u = \frac{\partial \phi}{\partial y}, v = -\frac{\partial \phi}{\partial x}, \omega = -\left(\frac{\partial u}{\partial y} - \frac{\partial v}{\partial x}\right), \quad (1.8)$$

It appears that one can do is to replace Eq. (1.7) by

$$\omega = \frac{1}{\mu} \frac{d\mu}{dc} (\nabla \phi \cdot \nabla c) - \frac{1}{k} (\nabla \phi \cdot \nabla k). \quad (1.9)$$

Here k is a fix parameter in Hele-Shaw cell, which is permeability of the media. Applying the concept to Eq. (5), the result is:

$$\omega = \frac{1}{\mu} \frac{d\mu}{dc} (\nabla \phi \cdot \nabla c). \quad (1.10)$$

Following other researchers (e.g. Tan and Homsy [23] and Rogerson Meiburg [39]), we define

$$R = -\frac{1}{\mu} \frac{d\mu}{dc}$$

a. Mobility ratio of the monotonic viscosity profile is:

$$\mu(c) = \exp[R(1-c)],$$

where

$$R_{mon} = -\frac{1}{\mu} \frac{d\mu}{dc} = \frac{-1}{\exp[R(1-c)]} \cdot \exp[R(1-c)] \cdot R \cdot (-1) = R. \quad (1.11)$$

b. Mobility ratio of Convex monotonic viscosity profile is:

$$\mu_{vex}(c) = \frac{\mu_2}{\mu_1} - \frac{\frac{\mu_2}{\mu_1}}{\exp\left(\ln\left(\frac{\mu_2}{\mu_1}\right) \times (1-c)\right)} + 1$$

$$\left. \frac{d\mu}{dc} \right|_{vex} = -\frac{\mu_2}{\mu_1} \frac{-\exp\left(\ln\left(\frac{\mu_2}{\mu_1}\right) \times (1-c)\right) - \ln\left(\frac{\mu_2}{\mu_1}\right)}{\exp\left(\ln\left(\frac{\mu_2}{\mu_1}\right) \times (1-c)\right)^2} = \frac{-\alpha R}{\exp\left(\ln\left(\frac{\mu_2}{\mu_1}\right) \times (1-c)\right)},$$

where

$$\begin{aligned}
R_{\text{vex}} &= -\frac{1}{\mu_{\text{vex}}} \left. \frac{d\mu_{\text{vex}}}{dc} \right|_{\text{vex}} = \frac{-1}{\frac{\mu_2}{\mu_1} - \frac{\frac{\mu_2}{\mu_1}}{\exp\left(\ln\left(\frac{\mu_2}{\mu_1}\right) \times (1-c)\right)} + 1} \frac{-\alpha R}{\exp\left(\ln\left(\frac{\mu_2}{\mu_1}\right) \times (1-c)\right)} \\
&= \frac{-1}{\alpha - \frac{\alpha}{\exp(R \times (1-c))} + 1} \frac{\alpha}{\left[\exp(R \times (1-c))\right]} \quad (1.12)
\end{aligned}$$

c. Mobility ratio of Linear monotonic viscosity profile is:

$$\left. \frac{d\mu}{dc} \right|_{\text{dir}} = -\alpha + 1,$$

where

$$R_{\text{linear}} = -\frac{1}{\mu_{\text{linear}}} (-\alpha + 1) = \left(\frac{1 - \alpha}{\alpha - \alpha c + c} \right). \quad (1.13)$$

d. Mobility ratio of Non-monotonic viscosity profile is:

$$\mu(c) = \mu_m \sin(\gamma), \quad \gamma = \gamma_0(1 - \beta) + \gamma_1\beta, \quad \beta = \frac{(1 + a)c}{1 + ac}$$

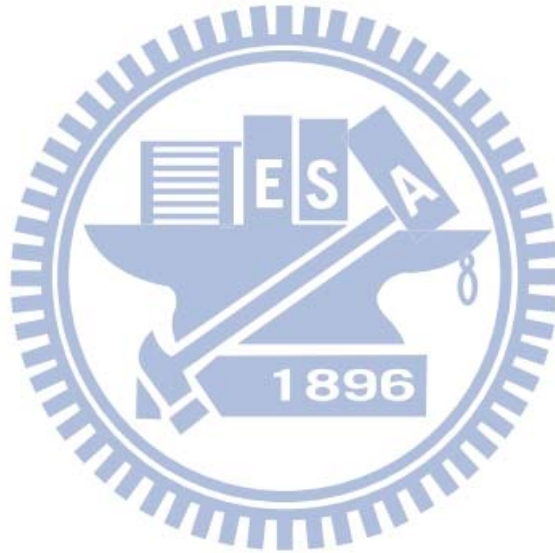
$$\gamma_0 = \sin^{-1}(\alpha/\mu_m), \quad \gamma_1 = \pi - \sin^{-1}(1/\mu_m),$$

$$a = \frac{c_m - \beta_m}{c_m(\beta_m - 1)}, \quad \beta_m = \frac{\frac{1}{2}\pi - \gamma_0}{\gamma_1 - \gamma_0},$$

where

$$\begin{aligned}
R_{\text{non}}(\mu) &= -\frac{1}{\mu} \frac{d\mu}{dc} = \frac{-1}{\mu_m \sin(\gamma)} \mu_m \frac{d \sin(\gamma)}{dc} = \frac{-1}{\sin(\gamma)} \cos(\gamma) \frac{d\gamma}{dc} \\
&= \cot(\gamma) \frac{d[\gamma_0(1 - \beta) + \gamma_1\beta]}{dc} \\
&= \cot(\gamma) \left[\gamma_0 \frac{d(1 - \beta)}{dc} + (1 - \beta) \frac{d\gamma_0}{dc} + \gamma_1 \frac{d\beta}{dc} + \beta \frac{d\gamma_1}{dc} \right]
\end{aligned}$$

$$\begin{aligned}
&= \cot(\gamma) \left\{ -\gamma_0 \frac{d\left[\frac{(1+a)c}{1+ac}\right]}{dc} + \gamma_1 \frac{d\left[\frac{(1+a)c}{1+ac}\right]}{dc} \right\} \\
&= \cot(\gamma) (\gamma_1 - \gamma_0) \frac{(1+ac)(1+a) - a(1+a)c}{(1+ac)^2} \\
&= (\gamma_1 - \gamma_0) \frac{(1+a)}{(1+ac)^2} \cot(\gamma)
\end{aligned} \tag{1.14}$$



Appendix 2 Hele-Shaw cell

The Navier-Stokes equation, which neglecting gravity, become

$$\frac{\partial V}{\partial t} + (V \cdot \nabla)V = \frac{1}{\rho}(-\nabla P + \mu\Delta V) \quad (2.1)$$

Assume the injection of fluid is slow enough for the flow to be approximately steady, parallel, and incompressible.

$$\frac{\partial V}{\partial t} = 0, V_z = 0, \nabla \cdot V = 0 \quad (2.2)$$

Simplifying, we get

$$u \frac{\partial u}{\partial x} + v \frac{\partial u}{\partial y} = -\frac{1}{\rho} \frac{\partial P}{\partial x} + \frac{\mu}{\rho} \left(\frac{\partial^2 V_x}{\partial x^2} + \frac{\partial^2 V_x}{\partial y^2} + \frac{\partial^2 V_x}{\partial z^2} \right) \quad (2.3)$$

$$u \frac{\partial v}{\partial x} + v \frac{\partial v}{\partial y} = -\frac{1}{\rho} \frac{\partial P}{\partial y} + \frac{\mu}{\rho} \left(\frac{\partial^2 V_y}{\partial x^2} + \frac{\partial^2 V_y}{\partial y^2} + \frac{\partial^2 V_y}{\partial z^2} \right) \quad (2.4)$$

If h is sufficiently small and the flow is slow, the first and second derivative of u and v with respect to x and y are negligible and prescribed as follows:

$$\frac{\partial u}{\partial y} = \frac{\partial v}{\partial y} = \frac{\partial^2 u}{\partial y^2} = \frac{\partial^2 v}{\partial y^2} = 0, \quad (2.5)$$

$$\frac{\partial u}{\partial x} = \frac{\partial v}{\partial x} = \frac{\partial^2 u}{\partial x^2} = \frac{\partial^2 v}{\partial x^2} = 0. \quad (2.6)$$

The derivate of pressure are specified as

$$\frac{\partial P}{\partial x} = \mu \frac{\partial^2 u}{\partial z^2}, \quad (2.7)$$

$$\frac{\partial P}{\partial y} = \mu \frac{\partial^2 v}{\partial z^2}, \quad (2.8)$$

$$\frac{\partial P}{\partial z} = 0. \quad (2.9)$$

The equation means that in the system, P does not depend on z .

$$\frac{\partial P}{\partial x} = \mu \frac{\partial^2 u}{\partial z^2} \quad (2.10)$$

$$\frac{\partial u}{\partial z} = \frac{1}{\mu} \left(\frac{\partial P}{\partial x} \right) z + C_1 \quad (2.11)$$

$$u(z) = \frac{1}{2\mu} \left(\frac{\partial P}{\partial x} \right) z^2 + C_1 z + C_2 \quad (2.12)$$

with boundary conditions and viscous force

$$u|_{z=0,h} = v|_{z=0,h} = 0, \quad \frac{\partial u}{\partial x}|_{z=\frac{h}{2}} = \frac{\partial v}{\partial y}|_{z=\frac{h}{2}} = 0$$

$$u(0) = u(h) = 0, \quad C_2 = 0, \quad C_1 = \frac{-1}{2\mu} \left(\frac{\partial P}{\partial x} \right) h$$

$$u(z) = \frac{1}{2\mu} \left(\frac{\partial P}{\partial x} \right) (z^2 - hz)$$

The integral means \tilde{u} and \tilde{v} of u and v across the gap are

$$\begin{aligned} \tilde{u} &= \frac{1}{2\mu h} \left(\frac{\partial P}{\partial x} \right) \int_0^h (z^2 - hz) dz \\ &= \frac{1}{2\mu h} \left(\frac{\partial P}{\partial x} \right) \left(\frac{z^3}{3} - \frac{hz^2}{2} \right) \Big|_0^h = \frac{-h^2}{12\mu} \left(\frac{\partial P}{\partial x} \right) \end{aligned} \quad (2.13)$$

$$\tilde{v} = \frac{-h^2}{12\mu} \left(\frac{\partial P}{\partial y} \right) \quad (2.14)$$

So the integral mean \tilde{V} of V satisfies

$$\tilde{V} = \frac{-h^2}{12\mu} \nabla P. \quad (2.15)$$

References

- [1] C. T. Tan and G. M. Homsy, “Stability of Miscible Displacements in Porous Media: Radial Source Flow”, *Physics of Fluids*, volume 30 issue 5, pp. 1239-1245, May 1987.
- [2] C. T. Tan and G. M. Homsy, “Simulation of Nonlinear Viscous Fingering in Miscible Displacement”, *Physics of Fluids*, volume 31 issue 6, pp. 1330-1338, June 1988.
- [3] O. Manikcam and G. M. Homsy, “Stability of Miscible Displacements in Porous Media with Nonmonotonic Viscosity Profiles”, *Physics of Fluids A*, volume 5, issue 6, pp. 1356-1367, June 1993.
- [4] H. Pascal and F. Pascal, “Dynamics of Non-Newtonian Fluid Interface in a Porous Medium: Incompressible Fluids”, *International Journal for Numerical Methods in Fluids*, volume 8, issue 11, pp. 1389-1401, November 1988.
- [5] C. -Y. Chen and E. Meiburg, “Miscible Porous Media Displacements in the Quarter Five-Spot Configuration. Part 1. The Monotonic Case”, *Journal of Fluid Mechanics*, volume 371, pp. 233-268, May 1998.
- [6] C. -Y. Chen, C. -H. Chen, and J. A. Miranda, “Numerical Study of Miscible fingering in a Time-dependent Gap Hele-Shaw Cell”, *Physical Review E* 71, 056304, 2005.
- [7] E. Meiburg and C. -Y. Chen, “High-accuracy Implicit Finite Difference Simulations of Homogeneous and Heterogeneous Miscible Porous Media Flows”, *Society of Petroleum Engineers Journal*, volume 5 issue 2, pp. 129-137, 2000.
- [8] C. -Y. Chen, C. -W. Huang, H. Gadêlha, and J. A. Miranda, “Radial Viscous Fingering in Miscible Hele-Shaw Flows: A Numerical Study”, *Physical Review E* 78, 016306, 2008.

- [9] C. -Y. Chen, C. -W. Huang, and L. -C. Wang, “Controlling Radial Fingering Patterns in Miscible Confined Flows”, *Physical Review E* 82, 056308, November, 2010.
- [10] O. Manikcam and G. M. Homsy, “Simulation of Viscous Fingering in Miscible Displacements with Nonmonotonic Viscosity Profile”, *Physics of Fluids*, volume 6 issue 1, pp. 95-107, January 1994.
- [11] M. Ruith and E. Meiburg, “Miscible Rectilinear Displacements with Gravity Override, Part 1. Homogeneous Porous Medium”, *Journal of Fluid Mechanics*, volume 420, pp. 225-257, May 2000.
- [12] B. Jha, L. Cueto-Felgueroso, and R. Juanes, “Fluid Mixing from Viscous Fingering”, *Physical Review Letters*, PRL 106, 194502, May 2011.
- [13] C. -Y. Chen and S. Wang, “Interfacial Instabilities of Miscible Fluids in a Rotating Hele-Shaw cell”, *Fluid Dynamics Research*, volume 30 issue 5, pp.315–330, May 2002.
- [14] C. -Y. Chen and Y. C. Liu, “Numerical Simulations of Miscible Fluids on a Rotating Hele-Shaw Cell with Effects of Coriolis Forces”, *International Journal for Numerical Methods in Fluids*, volume 48 issue 8, pp.853–867, July 2005.
- [15] C. -Y. Chen and H. -J. Wu, “Numerical Simulations of Interfacial Instabilities on a Rotating Miscible Magnetic Droplet with Effects of Korteweg Stresses”, *Physics of Fluids*, volume 17, issue 4, 042101, April 2005.
- [16] C. -H. Chen and C. -Y. Chen, “Numerical Simulations of Interfacial Instabilities on a Rotating Miscible Droplet in a Time-dependent Gap Hele-Shaw Cell with Significant Coriolis Effects”, *International Journal for Numerical Methods in Fluids*, volume 51, issue 8, pp.881–895, July 2006.

- [17] C. -H. Chen and C. -Y. Chen, “Fingering Patterns on an Expanding Miscible Drop in a Rotating Hele-Shaw cell”, *International Journal for Numerical Methods in Fluids*, volume 54, issue 10, pp.1201–1214, August 2007.
- [18] C. -H. Chen and C. -Y. Chen, “Numerical Simulations of Interfacial Instabilities on a Rotating Miscible Droplet in a Time-dependent Gap Hele–Shaw Cell with Significant Coriolis Effects”, *International Journal for Numerical Methods in Fluids*, volume 51, issue 8, pp.881–895, July 2006.
- [19] C. Pankiewicz and E. Meiburg, “Miscible Porous Media Displacements in the Quarter Five-spot Configuration. Part3. Non-monotonic Viscosity Profiles”, *Journal of Fluid Mechanics*, volume 388, pp 171-195, June 1999.
- [20] M. Shariati and Y. C. Yortsos, “Stability of Miscible Displacements across Stratified Porous Media”, *Physics of Fluids*, volume 13, number 8, pp. 2245-2257, August 2001.
- [21] S. H. Hejazi, P. M. J. Trevelyan, and De Wit, “Viscous Fingering of a Miscible Reactive $A+B \rightarrow C$ interface: a Linear Stability Analysis”, *Journal of Fluid Mechanics*, volume 652, pp.501-528, June 2010.
- [22] R. L. Chouke, “Stability Analysis for a Secondary Miscible Displacement with an Initially Sharp Solvent-oil Interface”, in *Proceedings of the Society of Petroleum Engineers/Department of Energy Third Joint Symposium on Enhanced Oil Recovery*, Tulsa, Oklahoma (Society of Petroleum Engineers, Dallas, Texas, 1982), SEP-10686, Appendix B of J. W. Gardner and J. G. J. Ypma.
- [23] C. T. Tan and G. M. Homsy, “Stability of Miscible Displacements in Porous Media: Rectilinear flow”, *Physics of Fluids*, volume 29, issue 11, pp. 3549-3556, November 1986.

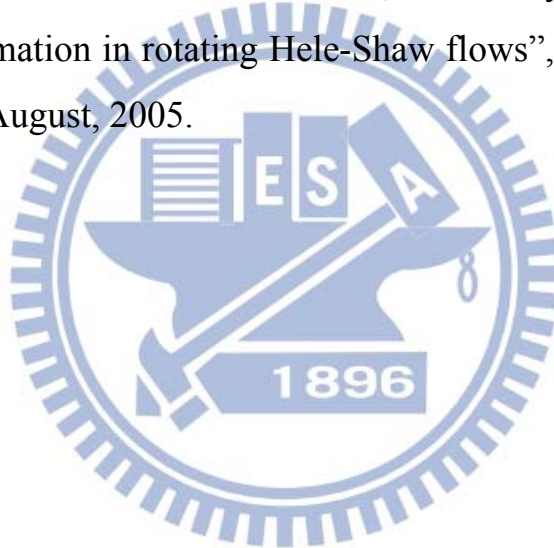
- [24] D. Loggia, D. Salin, and Yortsos, “The Effect of Dispersion on the Stability of Non-monotonic Mobility Profiles in Porous Media”, *Physics of Fluids*, volume 10, number 3, pp. 740-742, March 1998.
- [25] M. C. Kim and C. K. Choi, “The Stability of Miscible Displacement in Porous Media: Nonmonotonic Viscosity Profile”, *Physics of Fluids*, volume 23, issue8, 084105, August 2011.
- [26] A. Goriely and M. Tabor, “Self-Similar Tip Growth in Filamentary Organisms”, *Physical Review Letters*, volume 90, number 10, 108101, March, 2003.
- [27] J. A. Miranda, “Shear-induced effects in confined non-Newtonian fluids under tension”, *Physical Review E* 69, 016311, January 2004.
- [28] S. B. Gorell and G. M. Homsy, “A Theory of the Optimal Policy of Oil Recovery by Secondary Displacement Processes”, *SIAM Journal on Applied Mathematics*, volume 43, number 1, pp.79-98, February 1983.
- [29] M. J. Shelley, F-R. Tian, and K. Wlodarski, “Hele-Shaw Flow and Pattern Formation in a Time-Dependent Gap“, *Nonlinearity*, volume 10, issue 6, pp.1471-1495, November 1997.
- [30] E. Ben-Jacob, R. Godbey, N. D. Goldenfeld, J. Koplik, H. Levine, T. Mueller, and L. M. Sander, “Experimental Demonstration of the Role of Anisotropy in Interfacial Pattern Formation“, *Physical Review Letters*, volume 55, issue 12, pp.1315-1318, September 1985.
- [31] S. Z. Zhang, E. Louis, O. Pla, and F. Guinea, “Linear Stability Analysis of the Hele-Shaw Cell with Lifting Plates”, *The European Physical Journal B*, volume 1, issue 1, pp.123-127, October 1998.
- [32] A. Lindner, D. Derks, and M. J. Shelley, “Stretch Flow of Thin Layers of Newtonian Liquids: Fingering Patterns and Lifting Forces”, *Physics of Fluids*, volume 17, 072107, July 2005.
- [33] J. A. Miranda, R. M. Oliveira, and P. J. David, “Adhesion Phenomena

- in Ferrofluids”, *Physical Review E* 70, p036311, September 2004.
- [34] E. O. Dias and J. A. Miranda, “Control of Radial Fingering Patterns: A Weakly Nonlinear Approach”, *Physical Review E* 81, 016312, January 2010.
- [35] A. Leshchiner, M. Thrasher, M. B. Mineev-Weinstein, and H. L. Swinney, “Harmonic Moment Dynamics in Laplacian Growth”, *Physical Review E* 81, 016206, January 2010.
- [36] R. B. Bird, W. E. Stewart, and E.N. Lightfoot, Transport Phenomena, Wiley, New York, pp.150, 1960.
- [37] G. Rousseaux, A. De Wit, and M. Martin, “Viscous Fingering in Packed Chromatographic Columns: Linear Stability Analysis”, *Journal of Chromatography A*, 1149, pp.254-273, March 2007.
- [38] B. Gustafsson and A. Vasil’ev, “Conformal and Potential Analysis in Hele-Shaw Cells”, Birkhäuser Verlag, Switzerland, 2006.
- [39] A. Rogerson and E. Meiburg, “Shear Stabilization of Miscible Displacement Processes in Porous Media”, *Physics of Fluids A*, volume 5, issue6, pp. 1344-1355, June 1993.
- [40] E. Meiburg and C. Y. Chen, “High-Accuracy Implicit Finite Difference Simulations of Homogeneous and Heterogeneous Miscible-Porous-Medium-Flows”, *Society of Petroleum Engineers Journal*, volume 5, issue 2, pp.129-137, 2000.
- [41] C. -Y. Chen, L. -L. Wang, and E. Meiburg, “Miscible Droplets in a Porous Medium and the Effects of Korteweg Stresses”, *Physics of Fluids*, volume 13, issue 9, pp.2447-2456, September, 2001.
- [42] C. -Y. Chen, C. -H. Chen, and J. A. Miranda, “Numerical Study of Pattern Formation in Miscible Rotating Hele-Shaw Flows”, *Physics Review E* 73, 046306, April, 2006.
- [43] H. H. Hu and D. D. Joseph, “Miscible Displacement in a Hele-Shaw

- Cell”, *Zeitschrift für Angewandte Mathematik und Physik ZAMP*, volume 43, issue 4, pp. 626-644, July 1992.
- [44] Y. C Yortsos, “Stability of Displacement Processes in Porous Media in Radial Flow Geometries”, *Physics of Fluids*, volume 30, issue 10, pp. 2928.
- [45] S. K. Lele, “Compact Finite Difference Schemes with Spectral-like Resolution”, *Journal of Computer Physics*, volume 103, issue 1, pp. 16-42, 1992.
- [46] Josselin G. de, Jong de, “Singularity Distributions for the Analysis of Multiple-fluid Flow through Porous Media”, *Journal of Geophysical Research*, volume 65, issue 11, pp. 3739-3758, November, 1960.
- [47] C. -Y. Chen, Y. -S. Huang, and J. A. Miranda, “Diffuse-Interface Approach to Rotation Hele-Shaw Flows”, *Physics Review E* 84, 046302, April, 2011.
- [48] J. A. Miranda and M. Widom, “Radial Fingering in a Hele-Shaw Cell: a weakly nonlinear analysis”, *Physica D*, volume 120, issue 3-4, pp.315-328, September 1998.
- [49] C. -Y. Chen, Y. -S. Huang, and J. A. Miranda, “Radial Hele-Shaw Flow with Suction: Fully Nonlinear Pattern Formulation”, *Physics Review E* 89, 053006, September, 2014.
- [50] C. -Y. Chen and E. Meiburg, “Miscible Porous Media Displacements in the Quarter Five-Spot Configuration. Part 2. Effect of heterogeneities”, *Journal of Fluid Mechanics*, volume 371, pp. 269-299, September 1998.
- [51] Ll. Carrillo, F. X. Magdaleno, J. Casademunt, and J. Ortín, “Experiments in a rotating Hele-Shaw cell”, *Physical Review E* 54, 6260, December 1996.
- [52] E. Alvarez-Lacalle, J. Ortín, and J. Casademunt, “Low viscosity

contrast fingering in a rotating Hele-Shaw cell “, Physics of Fluids, volume 16,number 4, pp. 908-924, April, 2004.

- [53] E. Alvarez-Lacalle, J. Ortín, and J. Casademunt, “Relevance of Dynamic Wetting in Viscous Fingering Patterns”, Physical Review E 74, 025302, August 2006.
- [54] R. Folch, E. Alvarez-Lacalle, J. Ortín, and J. Casademunt, “Pattern Formation and Interface Pinch-off in Rotating Hele-Shaw Flows: A Phase-Field Approach”, Physical Review E 80, 056305, November 2009.
- [55] J. A. Miranda and E. Alvarez-Lacalle, “Viscosity contrast effects on fingering formation in rotating Hele-Shaw flows”, Physical Review E, 72, 026306, August, 2005.



Resume

中文姓名：王立杰

English Name:

出生年月：1972 年 12 月

籍貫：台北市

E-mail:bigsuperbird@yahoo.com.tw

一、 學歷(Education)

國立交通大學機械工程系博士班

中正理工學院兵器系統工程研究所

中正理工學院航空工程系

台北市立建國高級中學

二、 經歷(Work experience)

空軍第三修護補給大隊場站中隊

空軍測試評估暨戰術研發中心

國家中山科學研究院航空研究所

三、 研究著作(Publication)

(一)期刊論文(Journal Papers)

1. C. -Y. Chen, C. -W. Huang, L. -C. Wang, and Miranda, “Controlling radial fingering patterns in miscible confined flows”, Physical Review E, 82, 056308, November 2010. (SCI)
2. C. -Y. Chen, J. -F. Liu, and L. -C. Wang, “Instability Patterns of Ferrofluids Immersed in A Fluid Layer”, Magnetohydrodynamics, 46, number 3, pp235-244, 2010. (SCI)

(二)研討會論文(Conference Papers)

1. 王立杰, 「戰機增油設計研析」, 中華民國航空太空學會會刊, 第 42 卷第 1-4 期, Jan 2013.
2. L. -C. Wang, C. -W. Huang, and C. -Y. Chen, “Numerical Simulations on Miscible Radial Hele-Shaw Flows with a Non-Monotonic Viscosity Profile”, The 8th International Conference on Flow Dynamics, November 9-11; Sendai, Japan, 2011.
3. 王立杰, 陳振華, 陳慶耀, 「非一致型粘滯度分佈之可互溶徑向 Hele-Shaw 流場數值模擬」, 第 18 屆全國計算流體力學學術研討會, 宜蘭, Jul 2011.
4. 王立杰, 夏筱明, 「具後燃作用混流式渦扇引擎設計點操作性能之研究」, 中華民國燃燒學會第 13 屆學術研討會, 高雄, Mar 2003.
5. 王立杰, 夏筱明, 「模糊邏輯於典型渦輪風扇發動機修護決策率定之應用」, 2002「民航學會/航太學會/燃燒學會」學術聯合會議, 台北.

(三)月刊(monthly publication)

1. 「飛行載具紅外線特徵研究」, 空軍學術雙月刊第 615 期, Apr 2010
2. 「吸氣式推進系統於極超音速飛行載具之運用」, 空軍學術雙月刊第 610 期, Jun 2009
3. 「前翼構型戰機氣動力特性初探」, 空軍學術雙月刊 605 期, Aug 2008
4. 「航空發動機低污染燃燒技術研析」, 空軍學術雙月刊 599 期, Aug 2007
5. 「發動機監控與診斷系統發展」, 空軍學術雙月刊 596 期, Feb 2007
6. 「邊界層控制於未來戰機設計之初探」, 空軍學術月刊 585 期,

Aug 2005

7. 「流場控制對未來推進系統設計之影響」，空軍學術月刊 579 期，Feb 2005
8. 「垂直起降戰機操作特性初探」，空軍學術月刊 572 期，Jul 2004
9. 「飛行安全的最後防線—淺談彈設逃生」，空軍學術月刊 569 期，Apr 2004
10. 「整合飛控系統對戰機飛行性能之影響」，空軍學術月刊 560 期，Jul 2003
11. 「向量噴口對戰機設計的影響」，空軍學術月刊 551 期，Oct 2002
12. 「動件與控制邏輯對發動機整體性能之影響」，空軍學術月刊 545 期，Apr 2002
13. 「俄製戰機超級機動性之探討」，空軍學術月刊 526 期，Sep 2000
14. 「高攻角飛行的探討與 Su-27 戰機高攻角飛行性能剖析」，空軍學術月刊 517 期，Dec 1999